EFFECTS OF SURFACE MODIFICATION ON CHARGE-CARRIER DYNAMICS AT SEMICONDUCTOR INTERFACES

Thesis by

Agnes Juang

In Partial Fulfillment of the Requirements

for the Degree of Doctor of Philosophy

California Institute of Technology

Pasadena, California

2003

(Defended July 16, 2002)

© 2003

Agnes Juang

All Rights Reserved

Acknowledgments

The past five years have been the most incredible time of my life. Graduate school has changed the way I learn, the way I think, and the way I see things. I have gained so much more than what I had anticipated throughout the course of my study at Caltech, and I am glad that I chose to come here and stayed even when things got tough. Along the way, many people have landed their helping hands and gave me the strength to hang on. Without them, this thesis would not have been born.

I am grateful to have had a chance to learn electrochemistry first hand from Prof. Nathan Lewis. He is not only an exceptional scientist, but also one of the best in the field. I have learned a lot from Nate over the years including his high standard for research and persistent scientific honesty; his scientific intuition has not ceased to amaze me. I truly appreciate his forbearance and trust for allowing me to become an independent researcher.

I am thankful to have started my graduate work with a bunch of talented group members. Among all, Dr. Arnel Fajardo was the one whom I followed around the most, and the one who showed me how to hook up my electrochemical cell to the potentiostat. I am lucky to have Dr. Rob Rossi around for most of my time here at Caltech. He had provided me with lots of help and encouragement in and out of the lab. He was also the one who dragged me to the top of the snow-covered Bear Mountain and introduced me to the wonderful world of skiing, which had become my passion and had kept me sane during the winter time. To many others like Florian Gstrein, Dr. Nicholas Prokopuk, and Dr. William Royea, from whom I have learned a trick or two that made my work easier, my thanks go to them. As for the late comers, many have impressed me with their hunger for knowledge and their ambitions to make difficult projects work. Some of them have also let me use their instrument time during the last few months, which allowed me

to finish up on time, and I have to thank them for that. I am also very thankful to have a great collaborator Oren Scherman for the work included in Chapter 4. He saved me from having to do many organic synthesis, and I could always count on him for the best home-made chemicals.

Although Caltech is a wonderful place to be for researchers, it can sometimes make individuals feel trapped or isolated. Without my two closest friends at Caltech, Heather Cox and Dr. Anne Fu, and the almost-weekly lunch meetings we had, I would not have had many chances to talk about something other than science and politics when I am on campus. I also thank all of Nate's administrative assistants, especially Nannette Pettis, who had offered me help and an open door for small chats and complaints. Many people in Chemistry Department and Caltech administrative offices had also made my life easier when I was the head TA for Chem 1, and for that I gratefully thank them.

Best of all, I have met someone who understands not only my research, but also my heart. I thank Nick for his caring, patience, and love. He has shown me the true meaning of partnership through his constant support and understanding. He has also brought endless joy and laughter into my life; with him, life is always fun, fun, fun!

I would like to dedicate this thesis to my parents, Stephen and Sophia, who had bought me my first volume of science book and introduced me to the science at an early age. They had made me believe that I can do anything I want, and never stop having faith in me. Because of their hard work and sacrifices, I never had to worry about anything. Their unconditional love and support throughout my life is immeasurable, and I am forever indebted to that.

Abstract

Understanding the basic concepts of semiconductor junctions is an important step towards the development of efficient solar energy conversion devices. The work described in this dissertation includes both the investigation of semiconductor/liquid junctions and the modification of semiconductor surfaces for achieving chemical control over physical properties.

The interfacial charge-carrier dynamics of *n*-GaAs/CH_3CN junctions has been investigated. Differential capacitance barrier height measurements and steady-state current density–potential (*J*–*E*) measurements were used to evaluate the degree of partial Fermi-level pinning. The presence of irreversible chemical and/or electrochemical changes on *n*-GaAs electrodes immersed in CH_3CN-$CoCp_2^{+/0}$ solutions was examined using x-ray photoelectron spectroscopy (XPS) and cyclic voltammetric studies that were designed to probe surface reactions.

Chemical modifications of semiconductor surfaces can provide a reliable mean to control physical properties of semiconductor interfaces. The growth of robust polymer films that are covalently attached to Si surfaces via a Si-C linkage was demonstrated. Uniform polymer overlayers of different thicknessess were formed using a general method combining chlorination/Grignard reaction with ring-opening metathesis polymerization (ROMP). The surfaces of these modified Si were characterized by x-ray photoelectron spectroscopy (XPS), scanning electron microscopy (SEM), ellipsometry, and/or profilometry. The charge-carrier dynamics at these modified Si/air interfaces was investigated using transient photoconductivity decay method. Time-dependent photoconductivity measurements further confirmed the ability for polymer-terminated Si to maintain low surface recombination velocities once exposed to the air.

Table of Contents

Acknowledgments ... iii
Abstract ... v
Table of Contents ... vi
List of Figures ... ix
List of Tables ... xii

Chapter 1 Introduction ... 1

1. Overview ... 2
2. Charge-Transfer Equilibration at Semiconductor Heterojunctions ... 5
3. Current–Voltage Properties of a Semiconductor Diode ... 12
4. Charge-Carrier Recombination Mechanisms ... 14
   4.1. Interfacial Electron Transfer/Thermionic Emission ... 17
   4.2. Electron Tunneling ... 18
   4.3. Surface-State Recombination ... 19
   4.4. Depletion-Region Recombination ... 23
   4.5. Bulk-Region Recombination ... 24
5. Surface States ... 26
6. References ... 28

Chapter 2 Photoelectrochemical Behavior of *n*-GaAs in Acetonitrile Solutions ... 29

1. Introduction ... 30
2. Background ... 32
   2.1. Determination of the Electron-Transfer Rate Constant at the Semiconductor/Liquid Interface ... 32
   2.2. Fermi-Level Pinning ... 34
3. Experimental ... 37
   3.1. Electrode Material and Etching ... 37
   3.2. Solvents and Reagents ... 38
   3.3. Electrochemical Measurements ... 39
      3.3.1. Impedance Measurements ... 39
      3.3.2. Steady-State Current Density vs. Potential Characteristics ... 41
   3.4. Surface Analysis of *n*-GaAs in Contact with CH_3CN-$CoCp_2^{+/0}$ Solution ... 44
      3.4.1. X-ray Photoelectron Spectroscopy ... 44
      3.4.2. Cyclic Voltammetry ... 45

4. Results ... 46
4.1. Differential Capacitance vs. Potential Results and the Barrier Height of *n*-GaAs/CH_3CN-$CoCp_2^{+/0}$ Contacts ... 46
4.2. Steady-State *J–E* Behavior of *n*-GaAs/CH_3CN-$CoCp_2^{+/0}$ Contacts ... 55
4.2.1. *J–E* Data for *n*-GaAs electrodes in CH_3CN-$CoCp_2^{+/0}$ solutions ... 55
4.2.2. Photoresponses of *n*-GaAs electrodes in CH_3CN-$CoCp_2^{+/0}$ and CH_3CN-$Fc_2^{+/0}$ solutions ... 55
4.2.3. Effects of Exposure to CH_3CN-$CoCp2^{+/0}$ Solutions on the Behavior of *n*-GaAs/CH_3CN-$Fc^{+/0}$ Contacts ... 56
4.3. X-Ray Photoelectron Spectroscopy and Cyclic Voltammetry Data of *n*-GaAs Surfaces in Contact with the CH_3CN-$CoCp_2^{+/0}$ Electrolyte ... 62
5. Discussions ... 66
5.1. Electrochemical Properties of *n*-GaAs/CH_3CN Contacts ... 66
5.2. Interfacial Rate Constant Determinations Using *n*-GaAs/CH_3CN Contacts ... 67
6. Summary ... 70
7. Acknowledgments ... 70
8. References and Notes ... 71

Chapter 3 Fabrication and Characterization of *n*-Si(111) Based Metal-Insulator-Semiconductor Diodes ... 74

1. Introduction ... 75
2. Experimental ... 80
2.1. Solvents and Reagents ... 80
2.2. Semiconductor Material and Etching ... 81
2.3. Surface Modification ... 82
2.4. Metal Deposition and Device Fabrications ... 85
2.4.1. The First-Generation MIS Device ... 85
2.4.2. The Second-Generation MIS Device ... 86
2.4.3. The Third-Generation MIS Device ... 86
2.4.4. The Fourth-Generation MIS Device ... 87
2.5. Surface Characterization ... 93
2.6. Electrical Measurements ... 94
3. Results ... 97
3.1. Surface Modification ... 97
3.2. The *J–E* Behaviors of MIS Diodes ... 100
4. Discussions ... 107
5. Summary ... 110
6. References ... 110

Chapter 4 Transient Photoconductivity Decay Measurements of Polymer-Terminated Silicon Surfaces 113

1. Introduction 114
2. Experimental 119
   2.1. Chemicals 119
   2.2. Preparation of Substrates 120
   2.3. Surface Modification 121
      2.3.1. Chlorination 121
      2.3.2. Terminal-Olefin Addition via Grignard Reaction 122
      2.3.3. Catalyst Addition 123
      2.3.4. Polymerization 123
   2.4. Surface Characterizations 124
      2.4.1. X-ray Photoelectron Spectroscopy 124
      2.4.2. Overlayer Thickness Measurements: Ellipsometry and Profilometry 125
      2.4.3. Scanning Electron Microscopy 126
   2.5. Photoconductivity Decay Measurements 130
3. Results 138
   3.1. Surface Modifications 138
      3.1.1. Polynorbornene-Terminated Si 139
      3.1.2. PolyDCPD-Terminated Si 139
      3.1.3. ROMP of COD and COT 140
      3.1.4. Control Experiments 140
   3.2. Surface Characterizations 148
      3.2.1. Polymer Thickness Measurements 148
      3.2.2. Scanning Electron Microscopy 148
   3.3. Photoconductivity Decay Measurements 156
      3.3.1. C3 Olefin-Terminated and C3 Olefin-Polymer-Terminated Si Surfaces 156
      3.3.2. Effects of Olefin Linker Chain Length 158
      3.3.3. C5 Olefin-Terminated and C5 Olefin-Polymer-Terminated Si Surfaces 158
   3.4. Time-Dependent XPS Studies: Oxidation of Modified Si surfaces in Air 172
4. Discussions 180
   4.1. Surface Modifications and Characterizations 180
   4.2. Surface Recombination Velocity and Oxidation 184
5. Summary 188
6. Acknowledgments 188
7. References 189

List of Figures

Chapter 1

Figure 1.1 A band bending diagram for an ideal *n*-type semiconductor/liquid junction. 8

Figure 1.2 A band bending diagram for an ideal *n*-type semiconductor/metal junction. 10

Figure 1.3 Various types of recombination pathways for an *n*-type semiconductor/liquid junction. 16

Figure 1.4 A schematic depicting the microscopic balance between electron and hole capture and emission processes at recombination centers in the semiconductor. 22

Chapter 2

Figure 2.1 Open-circuit photovoltage vs. equilibrium cell potential for the *n*-GaAs/CH_3CN-$LiClO_4$ system at J_{ph} = 1.0 mA cm^{-2}. 36

Figure 2.2 Circuit diagrams for a semiconductor/liquid junction. 43

Figure 2.3 (a) A representative Bode plot for the *n*-GaAs/CH_3CN-$CoCp_2^{+/0}$ junction. 49

(b) A plot of phase angle vs. log *f* for the *n*-GaAs/CH_3CN-$CoCp_2^{+/0}$ junction. 50

(c) A representative Nyquist plot for the *n*-GaAs/CH_3CN-$CoCp_2^{+/0}$ junction. 51

Figure 2.4 (a) Mott-Schottky plot of the *n*-GaAs/CH_3CN-$CoCp_2^{+/0}$ junction. 53

(b) Linear extrapolations of the Mott-Schottky data shown in (a). 54

Figure 2.5 Representative *J–E* behaviors of *n*-GaAs electrodes in contact with CH_3CN-$CoCp_2^{+/0}$ solution. 57

Figure 2.6 Representative *J–E* behaviors of *n*-GaAs electrodes in contact with slightly wet CH_3CN-$CoCp_2^{+/0}$ solution. 58

Figure 2.7 (a) The *J–E* behavior of *n*-GaAs electrode in contact with CH_3CN-$Fc^{+/0}$ solution. 60

(b) The *J–E* behavior of *n*-GaAs electrode in contact with CH_3CN-$Fc^{+/0}$ solution after performing *J–E* scans in CH_3CN-$CoCp_2^{+/0}$ solution. 61

Figure 2.8 XP survey spectra of *n*-GaAs before and after 10 minutes of *J–E* scans in a CH_3CN-$CoCp_2^{+/0}$ solution. 64

Figure 2.9 Cyclic voltammogram of *n*-GaAs in CH_3CN-0.7 M $LiClO_4$ in the absence of a redox species. 65

Chapter 3

Figure 3.1 A band bending diagram of a metal/insulator-semiconductor (MIS) junction 79
Figure 3.2 An illustration of the first-generation MIS device. 89
Figure 3.3 An illustration of the second-generation MIS device. 90
Figure 3.4 An illustration of the third-generation MIS device 91
Figure 3.5 An illustration of the fourth-generation MIS device 92
Figure 3.6 XP survey spectra of H-terminated, Cl-terminated, C3-terminated, C6-terminated, and C10-terminated Si 98
Figure 3.7 (a) *J–E* behavior of H-terminated Si in contact with 450 Å of Ni 102
(b) *J–E* behavior of C3-terminated Si in contact with 450 Å of Ni 102
Figure 3.8 *J–E* behaviors of a series of C_nH_{2n+1}-terminated Si/Ni (n = 2, 4, 6, and 8) and an H-terminated Si/Ni junctions in the dark 104
Figure 3.9 Photoresponses of a series of C_nH_{2n+1}-terminated Si/Ni (n = 2, 4, 6, and 8) and an H-terminated Si/Ni junctions in the dark 105
Figure 3.10 Time-dependent *J–E* behaviors of a C_8H_{17}-terminated Si/Ni junction in the dark 106

Chapter 4

Figure 4.1 Polymer-terminated Si surfaces reported in literature 117
Figure 4.2 Experimental approach to produce a variety of covalently attached polymer overlayers on Si surfaces 127
Figure 4.3 A schematic of the radio frequency (rf) apparatus used to perform photoconductivity decay measurements 133
Figure 4.4 (a) A schematic of the controlled-environment chamber for sample storage 136
(b) A photograph of the controlled-environment setup 137
(c) A detailed photograph of the chamber interior 137
Figure 4.5 XP survey spectra of each step of the surface modification 142
Figure 4.6 XP survey spectra of polyDCPD-terminated Si. 144
Figure 4.7 XP survey spectra of control experiments 146
Figure 4.8 (a) A partial profilometric surface profile of a polynorbornene-terminated Si surface 151
(b) A SEM image of the same surface at 30× magnification 151
Figure 4.9 SEM top-view images of polynorbornene-terminated Si surfaces. 153
Figure 4.10 A cross-sectional SEM image of a polynorbornene-covered Si surface 155
Figure 4.11 Time-resolved photoconductivity decay curves of C3 olefin-terminated, C3 olefin-polynorbornene-terminated, and C3 olefin-polyDCPD-terminated Si surfaces in an N_2(g) ambient 161

Figure 4.12 Time dependence of the mean carrier lifetimes for C3 olefin-terminated, C3 olefin-polynorbornene-terminated, and C3 olefin-polyDCPD-terminated Si in air 162

Figure 4.13 Time dependence of the mean carrier lifetimes for mixed methyl/C3 olefin-terminated, C3 olefin-terminated, C5 olefin-terminated, and C6 olefin-terminated Si surfaces in air........ 163

Figure 4.14 Time-resolved photoconductivity decay curves of C5 olefin-terminated, C5 olefin-polynorbornene-terminated, and C5 olefin-polyDCPD-terminated Si surfaces in an N_2(g) ambient........ 164

Figure 4.15 (a) Time dependence of the mean carrier lifetimes for C5 olefin-terminated Si surfaces exposed to high temperature/humidity and low temperature/humidity conditions 166

(b)Time dependence of the mean carrier lifetimes for C5 olefin-polynorbornene-terminated Si surfaces exposed to high temperature/humidity and low temperature/humidity conditions........ 167

(c) Time dependence of the mean carrier lifetimes for C5 olefin-polyDCPD-terminated Si surfaces exposed to high temperature/humidity and low temperature/humidity conditions........ 168

Figure 4.16 Time dependence of the mean carrier lifetimes for C5 olefin-terminated, C5 olefin-polynorbornene-terminated, and C5 olefin-polyDCPD-terminated Si surfaces exposed to a low temperature/humidity condition........ 169

Figure 4.17 Time dependence of the mean carrier lifetimes for C5 olefin-terminated, C5 olefin-polynorbornene-terminated, and C5 olefin-polyDCPD-terminated Si surfaces exposed to a high temperature/humidity condition........ 170

Figure 4.18 Time-dependent high-resolution XP spectra of C5 olefin-terminated Si under low temperature/humidity condition........ 174

Figure 4.19 Time-dependent high-resolution XP spectra of C5 olefin-terminated Si under high temperature/humidity condition........ 175

Figure 4.20 Time-dependent high-resolution XP spectra of C5 olefin-polyDCPD-terminated Si under low temperature/humidity condition........ 176

Figure 4.21 Time-dependent High-resolution XP spectra of C5 olefin-polyDCPD-terminated Si under high temperature/humidity condition........ 177

Figure 4.22 Time-dependent high-resolution XP spectra of H-terminated Si under low temperature/humidity condition 178

Figure 4.23 A space-filling model of a Ru catalyst and a Si surface........ 183

Figure 4.24 The aged Si 2p high-resolution XP spectra of H-TERMINATED, C5 olefin-terminated, and C5 olefin-polyDCPD-terminated surfaces........ 187

List of Tables

Chapter 3

Table 3.1 A summary of reaction time, overlayer thickness, and air stability of alkyl-terminated Si 84

Chapter 4

Table 4.1 List of reagents and reaction conditions for Si surface modification 129

Table 4.2 Dependence of the polymer overlayer thickness on the concentration of norbornene in the solution 150

Table 4.3 Time-dependent measured carrier recombination lifetimes and surface recombination velocities for various modified Si surfaces 171

Table 4.4 Time dependence of the silicon oxide growth for polymer-terminated Si 179

Chapter 1

Introduction

1. Overview

From supporting our everyday lives to promoting cutting-edge technological advancements, fossil fuels have played a very important role for our civilization. As the finite amount of fossil reserves are being depleted at a rate that will not sustain the continuing growing human population, the need for affordable alternative energy sources has become more prominent. Renewable energy sources, like wind, hydro, and solar powers, are abundant and can be harnessed and utilized without further polluting our green planet. However, the well-established infrastructure for the extraction and distribution of fossil fuel-derived power has allowed the cost to remain relatively low, making more expensive solar energy less attractive. As people start to recognize our unsustainable practice of energy consumption, many may soon start to incorporate solar energy as part of their primary power source. For the prevalent utilization of solar energy to become a reality in a near future, scientists have to develop more efficient solar energy conversion devices while lowering the costs at the same time. Understanding the basic concepts of semiconductor junctions is the first step towards this goal.

The plants have evolved to make extensive use of solar energy in photosynthesis to convert sun light directly into stored fuels. Typical photosynthetic process, however, convert only 3–5% of the total incident solar power into fuel storage,[1] yet is sufficient to sustain life on Earth. On the other hand, the conversion of photon energy into electrical energy has been realized in photovoltaic devices consisting of two different solids connected at an abrupt junction which has the ability to direct electrical current flow in one direction through the external circuit.[2] These solid-state devices are currently being used for some applications; however, the required use of single crystals and the formation of abrupt junction make the cost of energy so produced too high to compete with that generated by burning fossil fuels. Although modern devices are quite efficient and

durable,[3] with such small economic value, the wide implementation of photovoltaic devices is proved to be difficult. A less-expansive solar energy conversion can be achieved by photoelectrochemical cells, which involve the use of semiconductor to adsorb incident light and the electrochemical process at semiconductor/liquid junction to allow energy conversion. The photoelectrochemical cells can be constructed to produce electricity or to store chemical fuels, and the efficiencies are generally between those of photovoltaics and photosynthesis.[1]

The basic challenge in developing practical photoelectrochemical solar energy conversion devices is the trade-off between the semiconductor stability and conversion efficiency.[1] Semiconductors with relatively high bandgap energies, such as titanium dioxide (TiO_2), absorb high-energy photons but only a small portion of the solar spectrum. TiO_2 is stable in aqueous solutions, but suffers a poor solar-conversion efficiency of about 1%. Materials made of germanium have very small bandgaps that can absorb a large fraction of the solar spectrum; unfortunately, a significant amount of absorbed energy is wasted as heat when the highly excited electrons readily relax to the energy of the conduction band edge. Semiconductors with moderate bandgaps, such as silicon (Si), gallium arsenide (GaAs), and indium phosphide (InP), are unstable in aqueous solutions, but prove to be the most efficient due to a well-overlapped bandgap energies with terrestrial solar spectrum.

The contacts between moderate bandgap semiconductors and aqueous electrolytes frequently result in photocorrosion or photopassivation of the electrode surfaces, which significantly limits the device lifetimes. One solution to this problem is the addition of a redox reagent that can compete kinetically with undesirable surface reactions. The difficulty involved is the extraordinary requirement of an extremely efficient redox species with very fast kinetics; otherwise the photocorrosion or photopassivation processes cannot be completely prevented. Another approach would be replacing the aqueous solution phase with a non-aqueous electrolyte system. Although the

combination is often toxic and not yet suitable for the commercial use, the semiconductor/non-aqueous liquid contacts are ideal for scientific investigation due to the constructional simplicity. Understanding of photoelectrochemical processes at these junctions is viable for future improvements of solar energy conversion devices.

This thesis includes investigations of charge-carrier dynamics at semiconductor junctions through the effects of surface modifications. A brief introduction to the fundamental theory of semiconductor heterojunctions and charge-carrier recombination process is included in this chapter. Chapter 2 presents both electrochemical and surface investigations of *n*-GaAs/CH_3CN interfaces. It also addresses the very importance of understanding the charge-carrier recombination mechanism in correctly assessing the electron-transfer processes across a semiconductor/liquid junctions. Chapter 3 describes an attempt to fabricate metal-insulator-semiconductor (MIS) diodes for improved electrical properties of a metal-semiconductor junction by surface modification of Si. Although problems exist that complicated the junction formation, some preliminary results offered valuable insights and hopes. Chapter 4 turns the focus back into the semiconductor surface chemistry and describes a surface modification procedure capable of producing stable Si surfaces that prevented the increase of surface defect density when exposed to air. The work included can be of importance for several technologies, and possible applications may not be limited to photovoltaics or photoelectrochemical cells.

2. Charge-Transfer Equilibration at Semiconductor Heterojunctions[1,4]

When a semiconductor comes into contact with a liquid or a metal phase, the difference in the electrochemical potential of the semiconductor and the contacting phase results in charge equilibration at the heterojunction. Since works present in this thesis involve *n*-GaAs and *n*-Si, the ideal junction between an *n*-type semiconductor and a contacting phase with a more positive electrochemical potential is described. The electrochemical potential of a freestanding semiconductor is set by the position of its Fermi level ($\mathbf{E}_{F}$), which is the energy level where the probability of finding an electron is one-half. When a solution containing a redox couple A/A^{-} (A is an electroactive acceptor and A^{-} is a donor) is the contacting phase, the electrochemical potential of the contacting phase ($\mathbf{E}_{F,c}$) is $\mathbf{E}(A/A^{-})$ and is given by the Nernst equation:

$$\mathbf{E}(A/A^{-}) = \mathbf{E}^{\circ\prime}(A/A^{-}) + (kT)\ln([A]/[A^{-}]) \qquad (1.1)$$

where $\mathbf{E}^{\circ\prime}(A/A^{-})$ is the electrochemical potential of the redox couple A/A^{-} under standard-state conditions, k is the Boltzmann's constant, and T is the absolute temperature. When the contacting phase is a metal the $\mathbf{E}_{F,c}$ is $\mathbf{E}_{F,m}$. Since it is difficult to experimentally determine the value of $\mathbf{E}_{F,m}$, work function of the metal (φ_{m}) is often used instead of $\mathbf{E}_{F,m}$.

When two phases are brought into contact, electrons flow from the phase with more negative initial electrochemical potential to the other, in this case from the semiconductor to the contacting phase, until the electrochemical potentials of both phases are in equilibrium. As the result of this charge-transfer process, both the semiconductor and the contacting phase lose their original charge neutrality. Excess positive charges are produced in the semiconductor while an excess of negative charges appears in the contacting phase. Since the number of available states per unit energy in the solution,

even with dilute concentration of redox species, or the metal far exceeds the number in a semiconductor, the accepted negative charges do not change the position of the $\mathbf{E}_{F,c}$. On the other hand, the Fermi level of the semiconductor becomes more positive, and the equilibrium position of the Fermi level for both phases is essentially equal to the initial value of the $\mathbf{E}_{F,c}$.

During the equilibration process, electrons that are the most easily ionized are removed first. This means that the charges are removed from dopant atoms before Si atoms are ionized. Since a certain number of electrons are needed from the semiconductor in order to reach the charge-transfer equilibrium, usually more than an atomic layer of dopant atoms are ionized. The distance into the semiconductor from the interface that is required for removal of charges from all the dopant atoms within this region is called the depletion width (W), and the region is called depletion region. A more positive initial $\mathbf{E}_{F,c}$ or a more negative initial $\mathbf{E}_{F}$ requires more layers of dopant atoms to be ionized, hence a larger W. The charge-transfer equilibration causes electric fields and electric potential gradients to rise in both phases, and the presence of this electric field at the interface is essential for the effective charge separation at semiconductor/liquid junction to separate charge effectively. A band bending diagram is used to depict the potential energy vs. distance relationship for a semiconductor/liquid junction (Figure 1.1) and for a semiconductor/metal junction (Figure 1.2). The electric potential energy levels of both conduction band ($\mathbf{E}_{cb}$) and valence band ($\mathbf{E}_{vb}$) drop within the depletion width as moving away from the interface and into the bulk of semiconductor. A barrier height (ϕ_b) is thus formed at the interface, and the barrier height energy ($q\phi_b$) is defined as the differences between the equilibrium Fermi level and the energy of the conduction band edge. In the case of semiconductor/metal junction, the ϕ_b can be calculated using thermodynamic model:[5,6]

$$\phi_b = (\varphi_m - \chi_s) / q \qquad (1.2)$$

where φ_m is the work function of the metal (in eV) and χ_x is the electron affinity of the semiconductor.

Figure 1.1

A band bending diagram for an ideal *n*-type semiconductor/liquid junction before equilibrium (a) and at equilibrium (b). (a) Before charge-transfer equilibration occurs, the energy levels of the conduction and the valence bands of the semiconductor are the same everywhere from the surface to the bulk. When a semiconductor with a more negative Fermi level ($\mathbf{E}_F$) is brought into contact with a solution with a redox potential $\mathbf{E}(A/A^-)$, electrons flow from the semiconductor to the solution phase. (b) After charge-transfer equilibration has occurred, a depletion layer of a width W formed in the semiconductor, and the contact potential drops primarily across this region. The Fermi level is the same across the junction at all points. The parameter qV_n is defined as the difference between $\mathbf{E}_F$ and $\mathbf{E}_{cb}$ in the bulk, V_{bi} is the built-in voltage of the junction, and the barrier height (ϕ_b) is defined as $\phi_b = V_{bi} + V_n$, and $q\phi_b$ is the difference between $\mathbf{E}_{cb}$ at the interface and $\mathbf{E}(A/A^-)$ of the solution.

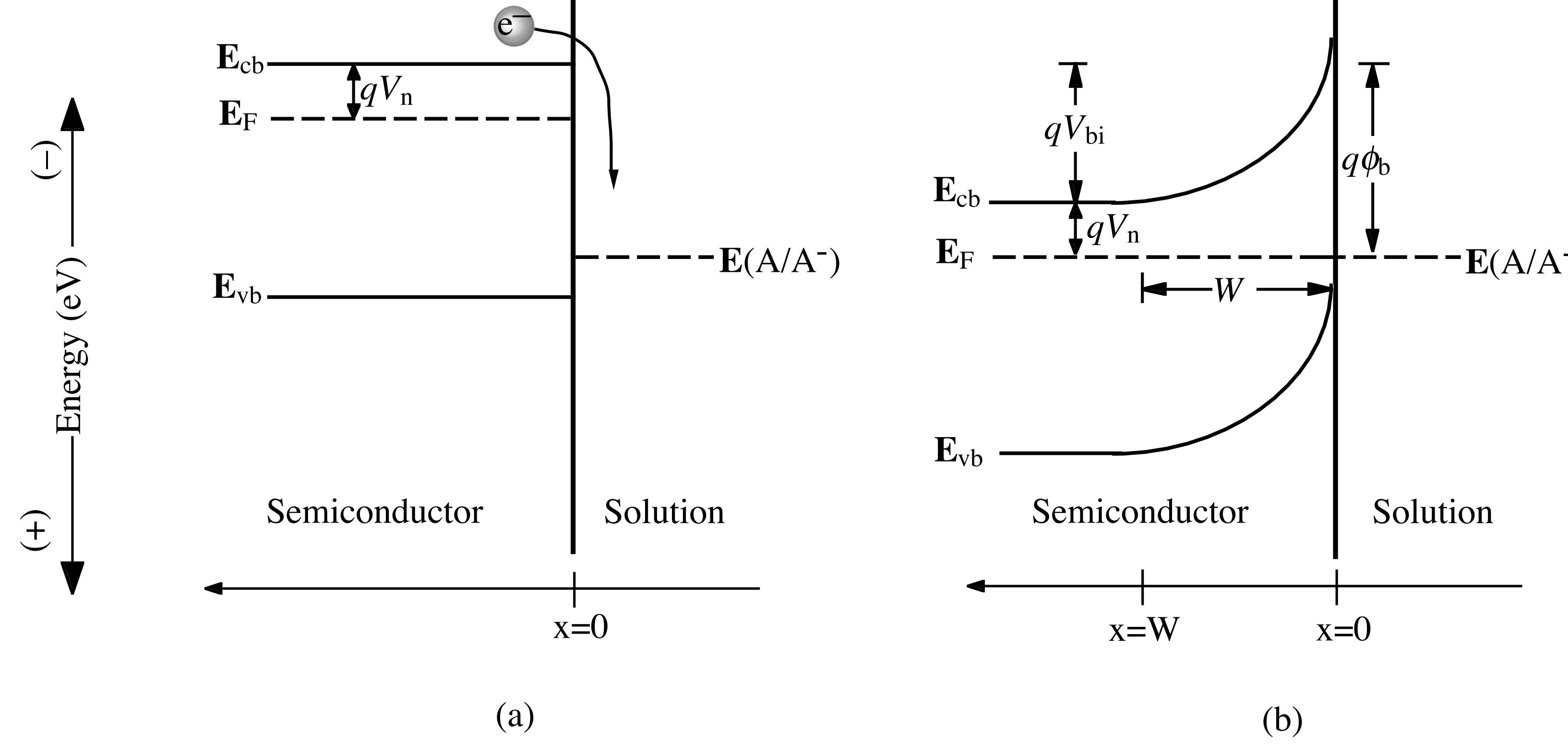

Energy (eV)
(−)
(+)
E_{cb}
E_F
E_{vb}
qV_n
e⁻
E(A/A⁻)
Semiconductor
Solution
x=0
(a)
qV_{bi}
$q\phi_b$
W
x=W
(b)

Figure 1.2

A band bending diagram for an ideal *n*-type semiconductor/metal junction before equilibrium (a) and at equilibrium (b). (a) Before charge-transfer equilibration occurs, the energy levels of the conduction a valence bands of the semiconductor are the same everywhere from the surface to the bulk. When a semiconductor with a more negative Fermi level ($\mathbf{E}_F$) is brought into contact with a metal with a Fermi level ($\mathbf{E}_{F,m}$), electrons flow from the semiconductor to the metal phase. (b) After charge-transfer equilibration has occurred, a depletion layer of a width W formed in the semiconductor and the contact potential drops primarily across this region. The Fermi level is the same across the junction at all points. The parameter qV_n is defined as the difference between $\mathbf{E}_F$ and $\mathbf{E}_{cb}$ in the bulk, V_{bi} is the built-in voltage of the junction, and the barrier height (ϕ_b) is defined as $\phi_b = V_{bi} + V_n$, and is the difference between the metal work function φ_m and the electron affinity χ_s of the semiconductor.

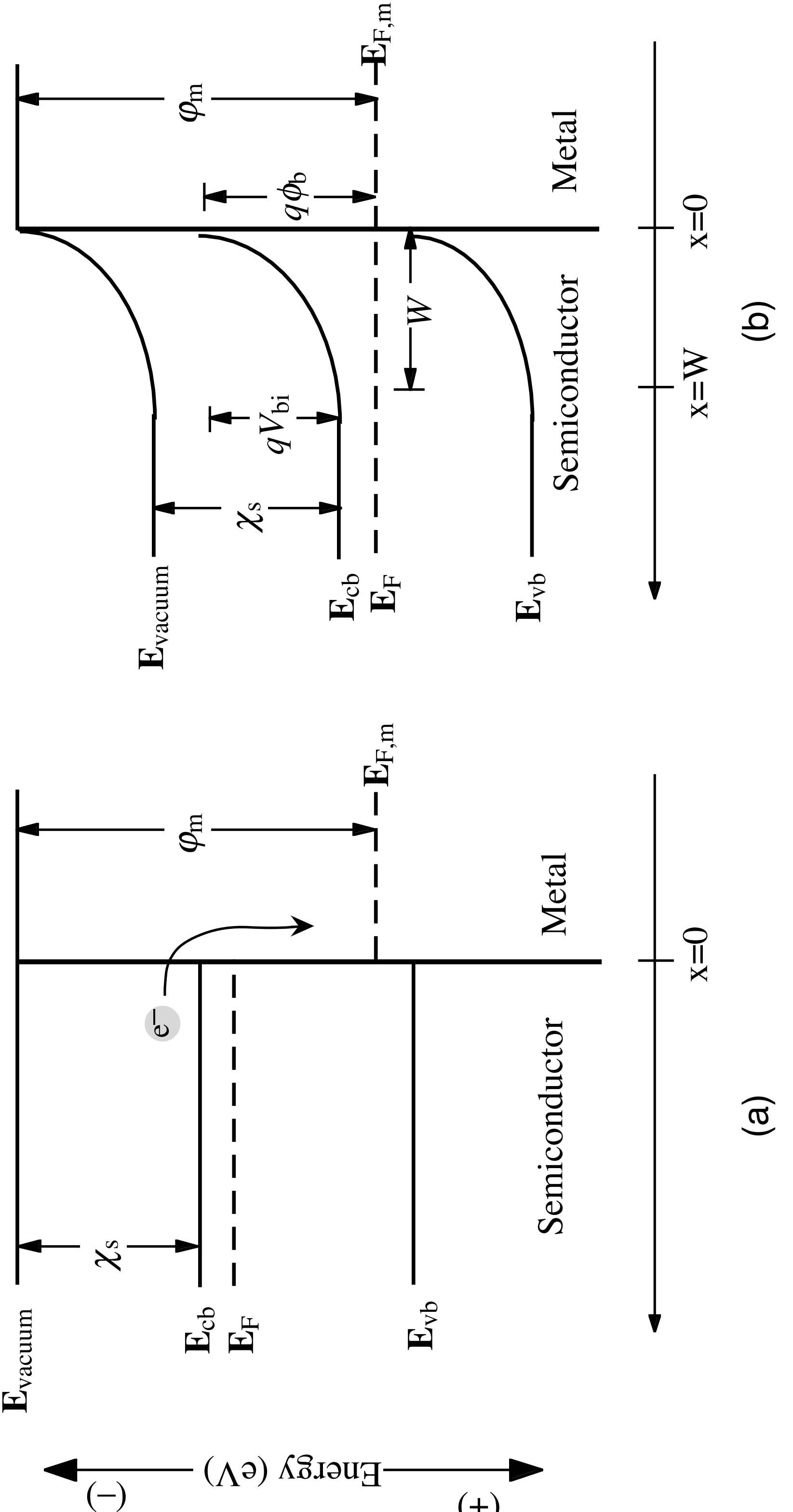
Energy (eV)
(−)
(+)
Evacuum
Ecb
EF
Evb
EF,m
χs
φm
e−
Metal
Semiconductor
x=0
(a)
qφb
qVbi
W
x=W
(b)

3. Current–Voltage Properties of a Semiconductor Diode

When a semiconducting material is illuminated with photons of sufficient energy (≥ bandgap energy, E_g), electrons are excited from valence band orbitals to the conduction band and leave behind positively charged sites (commonly referred to as "holes"). In the absence of an electric field, these photoexcited electrons quickly relax to their ground states and recombine with the holes. With the presence of an electric field formed at the semiconductor heterojunction, photogenerated carriers can be separated since electrons have a tendency to move away from the more negative interface while holes move towards it. The photogenerated electrons can then be collected at the ohmic back contact and directed through the external circuit to do useful work. The separation of charge carriers at semiconductor/liquid and semiconductor/metal junctions is the basis of solar energy conversion by photoelectrochemical cells and photovoltaics.

The flow of electrons through the external circuit due to photoexcitation is measured as the photocurrent (J_{ph}). The current can also flow in the opposite direction of the J_{ph} due to recombination of electron-hole pairs, and this unfavorable current is called reserve saturation current or recombination current (J_0). The discussion of charge-carrier recombination mechanisms is also in order. The total current (J) flowing across an *n*-type semiconductor heterojunction is described by the diode equation:[3,7]

$$J = J_{ph} - J_0\left[\exp\left(\frac{-qV}{\gamma kT}\right) - 1\right] \qquad (1.3)$$

where V is the applied voltage and γ is the diode quality factor. The anodic current is assigned positive values and the diode forward bias is negative on the electrochemical scale. The voltage developed by the photoelectrochemical cell under illumination, the open-circuit voltage (V_{oc}), is the voltage measured at $J = 0$, and is a measure of the

maximum Gibbs free energy available from the cell. For $J_{ph} >> J_0$, equation 1.3 can be rearranged to yield

$$V_{oc} = \frac{\gamma kT}{q} \ln\left(\frac{J_{ph}}{J_0}\right) \tag{1.4}$$

Measurements of V_{oc} and J_{ph} at several illumination intensities, combined with the use of equation 1.4, can allow the extraction of J_0. Since this measurement is performed at no net current flow, it can eliminate the problems that can distort the *J–V* properties of many semiconductor/liquid junctions. These potential problems include the presence of a large series resistance at high current flow and a nonlinear voltage drop due to mass transport limit of the redox species.[7-9]

4. Charge-Carrier Recombination Mechanisms[10]

Once the electron-hole pairs are generated in the semiconductor by photoexcitation, electrons and holes can find ways to recombine before being harnessed to do useful work. Generally there are five types of recombination mechanisms that can contribute to the recombination current (J_0). Depending on the location of recombination relative to the junction, the recombination pathways are grouped into either majority carrier processes or minority carrier processes. Figure 1.3 depicts several pathways that the recombination processes can occur at the semiconductor/liquid junction. All possible recombination mechanisms usually occur simultaneously for a given sample, and the total recombination current is the sum of the individual recombination currents:

$$J_0 = J_{\mathrm{et}} + J_{\mathrm{tun}} + J_{\mathrm{ss}} + J_{\mathrm{dr}} + J_{\mathrm{br}} \qquad (1.5)$$

where subscript "et" is the recombination due to interfacial electron transfer when the contacting phase is a liquid and is replaced by "th", the thermionic emission, when the contacting phase is a metal, subscript "tun" is the recombination due to electron tunneling, subscript "ss" is the surface-state recombination, subscript "dr" is the depletion-region recombination, and subscript "br" is the bulk-region recombination. Depending on the semiconductor dopant density (N_{d}), barrier height, the density of surface traps located within the bandgap, and the applied bias (V), one pathway usually dominates the recombination event and therefore J_0. These recombination processes will be discussed briefly in the next two sections.

When electrons are injected into the contacting phase and recombine with holes outside of the semiconductor, it is categorized as a majority carrier recombination. Two pathways involving this process are interfacial electron transfer, or thermionic emission, and tunneling through the surface potential barrier. If the surface barrier is large or wide,

electron injection into the contacting phase might be more difficult. In this case, the rate of hole injection into the semiconductor dominates the carrier transport across the interface, and the injected holes travel through the semiconductor and can recombine with electrons via one of the three pathways: surface-state recombination, depletion-region recombination, and bulk-region recombination.

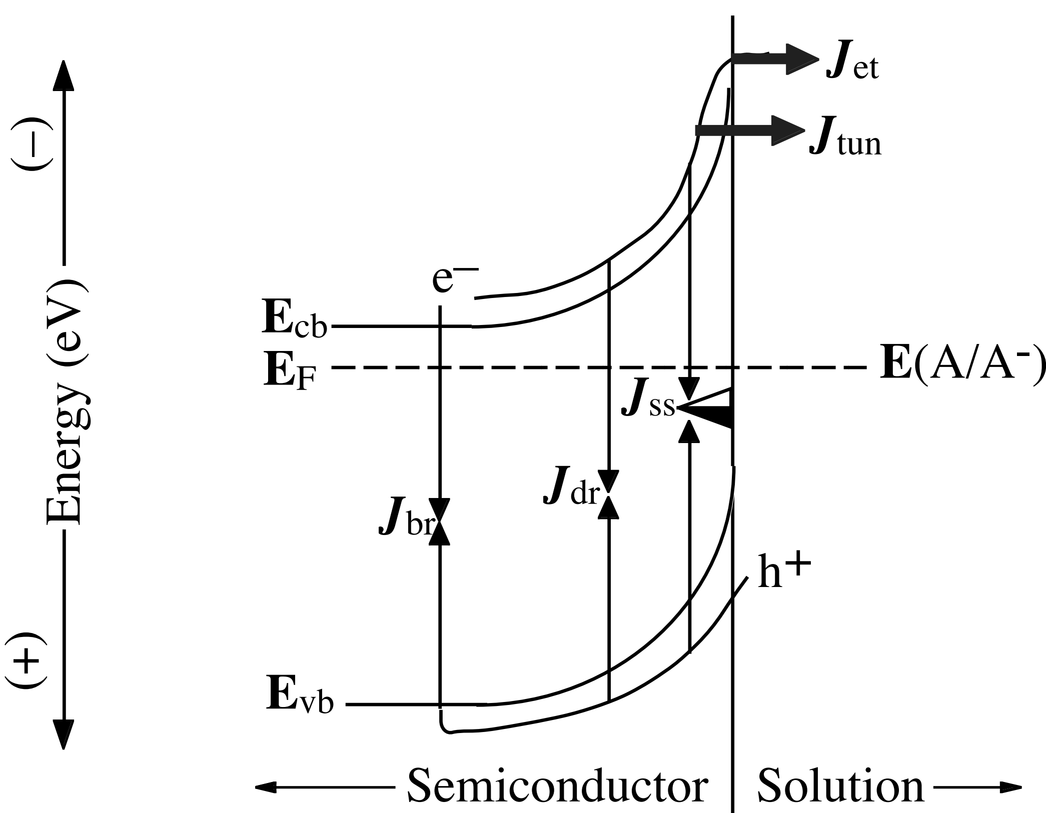

Figure 1.3

Various types of recombination pathways for an *n*-type semiconductor/liquid junction. The J_{et} is the current caused by electron transfer over the potential barrier from the semiconductor to the redox acceptors in the solution. The J_{tun} describes the majority carrier tunneling current through the potential barrier. Recombination due to the surface states near the interface results in J_{ss}, while recombination in the depletion and bulk regions produces J_{dr} and J_{br}, respectively. Both J_{et} and J_{tun} are currents requiring injection of majority carriers from the semiconductor, hence majority carrier recombination currents. On the other hand, J_{ss}, J_{dr}, and J_{br} are currents due to minority carrier recombination process, since holes are injected into the semiconductor for the recombination to occur.

4.1. Interfacial Electron Transfer/Thermionic Emission

At semiconductor/metal junctions (Schottky junctions), the interfacial electron transfer over the top of the surface barrier is called thermionic emission. Since the metal has a very high density of unoccupied levels, every electron that reaches the top of the surface barrier is assumed to be captured by the metal phase.[7,9] The relationship between J_0 and ϕ_b can be described by the thermionic emission theory:[11]

$$J_0 = A^{**}T^2 \exp\left(\frac{-q\phi_b}{kT}\right) \tag{1.6}$$

where A^{**} is the modified Richardson constant, which is the probability of an electron being injected into the metal once it reaches the interface. Since ϕ_b is not a function of N_d, the thermionic emission current is independent of the dopant density of semiconductor. When the thermionic emission is the dominant recombination mechanism, the experimentally determined γ is 1, and the activation energy is $q\phi_b$.

At semiconductor/liquid junctions, the interfacial electron-transfer event is governed by both the concentration of electrons at the semiconductor surface (n_s) and the concentration of acceptor species in solution ([A]). The recombination current can be expressed as:[12,13]

$$J_0 = qk_{et}n_s[A] \tag{1.7}$$

where k_{et} is the rate constant for electron transfer from the semiconductor to the redox acceptor in solution.

4.2. Electron Tunneling

The electron tunneling rate can be calculated with quantum theory by modeling the potential barrier as triangular. The probability of tunneling through the base of the barrier is

$$T_{\text{tun}} = \exp\{-8\pi W[2qm_e^*(|V_{\text{bi}}| + V)]^{1/3} / 3h \tag{1.8}$$

where m_e* is the effective mass of an electron, V_{bi} is the difference between the conduction band edge at the surface and in the bulk, and h is the Planck's constant. The total current can be described as

$$J = qv_{\text{th}}T_{\text{tun}}(\mathbf{E})dn(\mathbf{E}) \tag{1.9}$$

The rate of electron tunneling through the potential barrier usually only dominates the recombination rate when the semiconductor is highly doped. When the dopant density is high, the relatively small W results in a thin barrier, which allows electrons to cross into the contacting phase. The recombination current depends on dopant density and is a complicated function of V, T, and N_d (affects V_{bi}). If the recombination due to electron tunneling is the dominant mechanism, the experimentally determined γ is greater than 1.

4.3. Surface-State Recombination

Nonradiative recombination mediated by energy levels within the bandgap can be described by Shockley-Read-Hall (SRH) statistics.[14,15] The rate of surface-state recombination can be derived by evaluating the microscopic balance between electrons and holes capture and emission processes by recombination centers at the semiconductor surface.

Assuming a given number density of recombination centers at surface ($N_{r,s}$, cm^{-2}) exist at an energy within the bandgap $\mathbf{E}_{r,s}$ (Figure 1.4). The net rate of electron occupying these recombination centers is equal to the capture rate of electrons in conduction band minus the thermal emission rate of electrons back to the conduction band:

$$\frac{d(N_{r,s}f_{r,s})}{dt} = n_s k_{n,s} N_{r,s}(1 - f_{r,s}) - k'_{n,s} N_{r,s} f_{r,s} \tag{1.10}$$

and the net rate of holes in valence band occupying these recombination centers is

$$\frac{d[N_{r,s}(1 - f_{r,s})]}{dt} = p_s k_{p,s} N_{r,s} f_{r,s} - k'_{p,s} N_{r,s}(1 - f_{r,s}) \tag{1.11}$$

where $f_{r,s}$ is the fraction of occupied recombination centers, n_s is the number of electrons in the conduction band, p_s is the number of holes in the valence band, $k_{n,s}$ and $k_{p,s}$ is the capture coefficient of electrons and holes by the recombination centers, and $k'_{n,s}$ and $k'_{p,s}$ is the emission coefficient of electrons and holes from the filled recombination centers. Let $n_{1,s}$ and $p_{1,s}$ be the surface electron and hole concentrations when the Fermi level is located at $\mathbf{E}_{r,s}$, $k_{n,s}$ and $k_{p,s}$ can be related to $k'_{n,s}$ and $k'_{p,s}$, respectively, using the principle of detailed balance at steady state, which tells us that each process is in equilibrium by itself and also with other processes:

$$k'_{\mathrm{n,s}} = k_{\mathrm{n,s}} N_{\mathrm{c}} \exp[(\mathbf{E}_{\mathrm{r,s}} - \mathbf{E}_{\mathrm{c,s}}) / kT] = k_{\mathrm{n,s}} n_{1,\mathrm{s}} \quad (1.12)$$

$$k'_{\mathrm{p,s}} = k_{\mathrm{p,s}} N_{\mathrm{v}} \exp[(\mathbf{E}_{\mathrm{r,s}} - \mathbf{E}_{\mathrm{v,s}}) / kT] = k_{\mathrm{p,s}} p_{1,\mathrm{s}} \quad (1.13)$$

N_{c} and N_{v} are the density of electronic states in the conduction band and valence band, and $\mathbf{E}_{\mathrm{c,s}}$ and $\mathbf{E}_{\mathrm{v,s}}$ are the energy of the conduction and valence band edges at the surface, respectively.

Under the steady-state conditions, the occupancy density of the states is constant, and the recombination rate (U_{s}) is equal to $d(N_{\mathrm{r,s}} f_{\mathrm{r,s}})/\mathrm{dt} = d[N_{\mathrm{r,s}}(1\text{-}f_{\mathrm{r,s}})]/\mathrm{dt}$. The $f_{\mathrm{r,s}}$ can be solved by setting equations 1.10 and 1.11 equal to each other. Substituting the expression for $f_{\mathrm{r,s}}$ back into either equation and realizing $n_{1,\mathrm{s}} p_{1,\mathrm{s}} = n_{\mathrm{i}}^2$ (n_{i} is the intrinsic carrier concentration) yields

$$U_{\mathrm{s}} = N_{\mathrm{r,s}} \frac{k_{\mathrm{n,s}} k_{\mathrm{p,s}} (n_{\mathrm{s}} p_{\mathrm{s}} - n_{\mathrm{i}}^2)}{k_{\mathrm{n,s}} (n_{\mathrm{s}} + n_{1,\mathrm{s}}) + k_{\mathrm{p,s}} (p_{\mathrm{s}} + p_{1,\mathrm{s}})} \quad (1.14)$$

Equation 1.14 represent sthe net rate of surface-state recombination for recombination centers located at a single energy level $\mathbf{E}_{\mathrm{r,s}}$, and the total surface-state recombination current can be obtained by integrating U_{s} over all possible recombination center energies. Surface recombination velocity (S) represents the pseudo-first-order rate constant for surface-state recombination of minority carrier and is commonly used to characterize the surface property of semiconductors. During photoexcitation, the surface carrier concentrations can be described as the sum of equilibrium and injected carrier concentrations ($n_{\mathrm{s}} = n_{0,\mathrm{s}} + \Delta n_{\mathrm{s}}$ and $p_{\mathrm{s}} = p_{0,\mathrm{s}} + \Delta p_{\mathrm{s}}$). Substituting these terms and $U_{\mathrm{s}} \equiv S \Delta p_{\mathrm{s}}$ into equation 1.14 results in the following expression, taking into account that $n_{0,\mathrm{s}} p_{0,\mathrm{s}} = n_{\mathrm{i}}^2$:

$$S = N_{\mathrm{r,s}} \frac{k_{\mathrm{n,s}} k_{\mathrm{p,s}} [n_{0,\mathrm{s}} + (p_{0,\mathrm{s}} \Delta n_{\mathrm{s}} / \Delta p_{\mathrm{s}}) + \Delta n_{\mathrm{s}}]}{k_{\mathrm{n,s}} (n_{0,\mathrm{s}} + \Delta n_{\mathrm{s}} + n_{1,\mathrm{s}}) + k_{\mathrm{p,s}} (p_{0,\mathrm{s}} + \Delta p_{\mathrm{s}} + p_{1,\mathrm{s}})} \quad (1.15)$$

Since S (has units of velocity, cm s^{-1}) is a function of electron and hole concentrations, the parameter depends on variables such as illumination level, applied potential, and temperature. At high level injection, concentrations of photogenerated carriers Δn_s and Δp_s are much greater than $n_{0,s}$ and $p_{0,s}$, respectively, and $\Delta n_s = \Delta p_s$. Equation 1.13 can be rewritten as:

$$S = N_{r,s} \frac{k_{n,s} k_{p,s}}{k_{n,s} + k_{p,s}} \quad (1.16)$$

At low level injection, $\Delta n_s = \Delta p_s$, $\Delta p_s >> p_{0,s}$, and $\Delta n_s << n_{0,s}$; equation 1.13 can then be simplified:

$$S = N_{r,s} k_{p,s} = 1 / \tau_{p,s} \quad (1.17)$$

where $\tau_{p,s}$ is defined as minority carrier lifetime at the surface. When S is measured under either of these conditions, S is independent of carrier concentrations and allows for the extraction of surface recombination trap density without the effect of perturbation. At high level injection the slowest of either electron or hole capture dominates the S, while it is controlled only by the hole capture at low level injection. The surface-state recombination current can be expressed in a way similar to a diode equation by factoring out the injected carrier concentration Δp_s:

$$J = qU = qSp_{0,s}[\exp(-qV / kT) - 1] \quad (1.18)$$

From equation 1.18, γ is predicted to be 1 for surface-state recombination, although it can be higher than 1 under the low level injection condition.

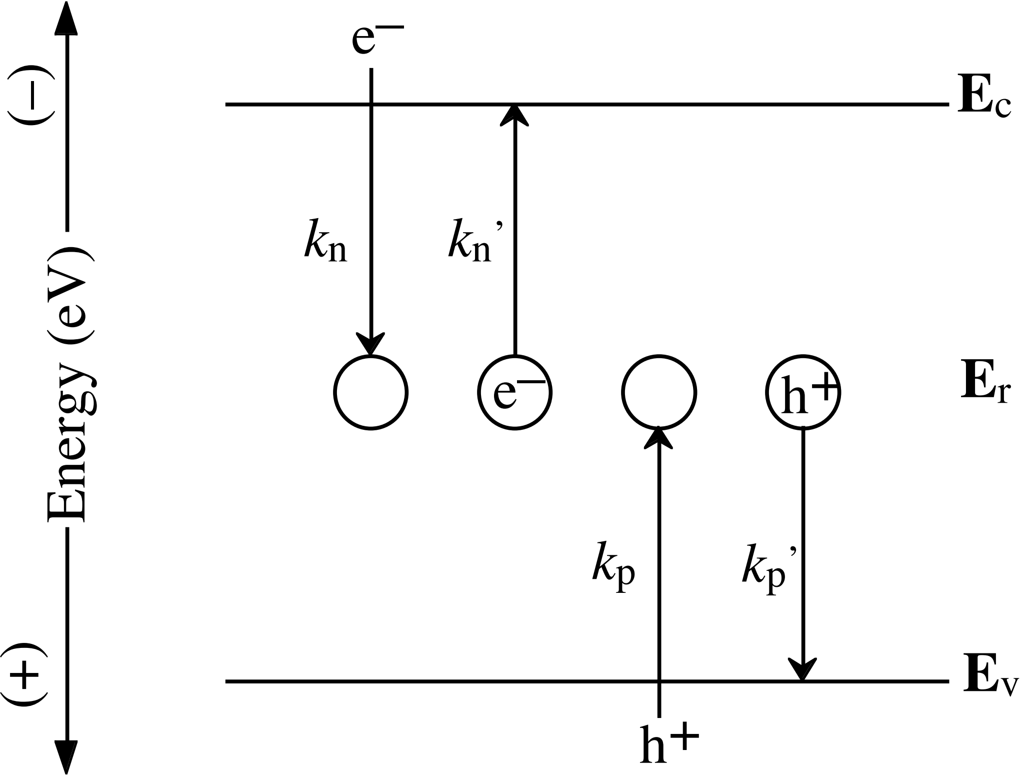

Figure 1.4

A schematic depicting the microscopic balance between electron and hole capture and emission processes at recombination centers in the semiconductor. The k_n and k_p are the capture coefficients of electrons and holes by the recombination centers at an energy level of $\mathbf{E}_r$, respectively. The k_n' and k_p' are the thermal emission coefficients of electrons and holes from the recombination centers back to the conduction and valence bands, respectively. The $\mathbf{E}_c$ and $\mathbf{E}_v$ are energies of conduction and valence band edges.

4.4. Depletion-Region Recombination

Depletion-region recombination can also be calculated using SRH statistics. We use the Equation 1.14 derived in the previous section, and drop the subscript "s" in all parameters to yield the following expression, with N_r (having a unit of cm^{-3}) now accounts for the density of recombination centers within the semiconductor:

$$U = N_r \frac{k_n k_p (np - n_i^2)}{k_n(n + n_1) + k_p(p + p_1)} \tag{1.19}$$

Since only those recombination centers with energy levels at the mid-gap are the most effective traps, we can assume $k_n = k_p$. To obtain the depletion-region recombination current, U has to be integrated over the limits of depletion region. The value of U has a large dependence on both n and p, and the maximum value of U exist when $n = p$.

$$U_{max} = \frac{n_i}{2\tau_p} \exp(-qV / 2kT) \tag{1.20}$$

The integral $\int U(x)dx$ can then be replaced by the U_{max} multiplied by a width over which this maximum rate occurs. The effective width for the integration is $kTW/q(V_{bi}+V)$, and the depletion-region recombination current can be obtained:

$$J = \int_0^{kTW/q(V_{bi}+V)} qUdx = \frac{kTWn_i}{2\tau_p(V_{bi}+V)} \exp(-qV / 2kT) \tag{1.21}$$

From equation 1.21, a γ of 2 is often an indication that the recombination current is dominated by the depletion-region recombination. Assuming J_{dr} dominates the recombination current, substituting $n_i = (N_c N_v)^{1/2} \exp(\mathbf{E}_g/2kT)$ into equation 1.19 yields an expression for the J_0:

$$J_0 = \frac{kTW(N_c N_v)^{1/2}}{2\tau_p(V_{bi} + V)} \exp(-\mathbf{E}_g / 2kT) \exp(-qV / 2kT) \tag{1.22}$$

4.5. Bulk-Region Recombination

The current for the bulk recombination process is a function of hole diffusion rate into the bulk region of the semiconductor. Assuming that depletion-region recombination does not occur, and at any point x, the recombination rate in the bulk is the same as the diffusion rate:

$$[p(x) - p_0(x)] / \tau_p + D_p \frac{\delta^2 p(x)}{\delta x^2} = 0 \tag{1.23}$$

where $p(x)$ and $p_0(x)$ are the hole concentration and the equilibrium hole concentration at a point x in the bulk, and D_p is the hole diffusion coefficient. Since the total current at steady state is the same everywhere in the bulk, the total bulk recombination current can be determined by solving the hole concentration at the deletion layer edge. Two boundary conditions will be applied. First is the assumption of the absence of depletion-region recombination at the depletion layer edge $x = W$:

$$n(W)p(W) = n_i^2 \exp(-qV / kT) \tag{1.24}$$

Because the injected minority carrier concentration is much lower than the dopant density, $n(W) \approx n(W)$, and equation 1.24 becomes

$$p(W) = p_0 \exp(-qV / kT) \tag{1.25}$$

Adding in the second boundary condition that all the holes recombine in the bulk before reaching the ohmic contact, $p(\infty) = p_0$, $p(x)$ can be solved:

$$p(x) = p_0 + p_0[\exp(-qV / kT) - 1]\exp[-(x - W) / L_\mathrm{p}) \qquad (1.26)$$

where L_p is the hole diffusion length. Substituting this expression into $J_\mathrm{p} = qD[dp(x)/dx]$, and then the current at $x = W$ can be evaluated:

$$J_\mathrm{p}(W) = \frac{qD_\mathrm{p}p_0}{L_\mathrm{p}}[\exp(-qV / kT) - 1] \qquad (1.27)$$

If the bulk-region recombination is the dominant mechanism, the γ is expected to be 1, and the activation energy $\mathbf{E}_\mathrm{g}$. If $J_\mathrm{p}(W)$ is equal to the total bulk recombination current:

$$J_0 = \frac{qD_\mathrm{p}p_0}{L_\mathrm{p}} = \frac{qD_\mathrm{p}n_\mathrm{i}^2}{L_\mathrm{p}N_\mathrm{d}} \qquad (1.28)$$

5. Surface States[10]

In order to improve the efficiency and the stability of photoelectrochemical or photovoltaic devices, the unfavorable current due to recombination has to be suppressed. While many strategies to improve the solar energy conversion devices have been researched by others, the central theme of this thesis is to approach the challenge by investigating the surface states at the semiconductor/liquid junction and proposing a solution to improve the stability by surface modification. As the size of semiconductor devices continues to decrease, the effects of surface defects also become considerably more significant. Understanding of semiconductor surface properties and developments of methods that can improve the electrical properties of semiconductors can certainly provide unimaginable benefits for technologies of the future.

The different orbital structure of a semiconductor surface compared to its bulk usually results in one or more energy levels located inside of the bandgap region. These localized surface states can be either intrinsic or extrinsic in nature. The intrinsic surface states can arise because the surface atoms of a semiconductor do not have the periodic bonding structure that exists in the crystal lattice, or due to the reconstruction of the surface. The extrinsic surface states are the result of interface formation. Surface defects can emerge if a reaction or bonding occurs between the two phases in contact, and the adsorption or attachment of chemical impurities can also contribute to the surface states.

Although not all surface bonds produce deleterious surface states, those reside in the bandgap can unquestionably affect the electrical properties of a semiconductor. The presence of these surface states can provide recombination centers and reduce the carrier lifetime. They can also serve as sinks or sources for electrical charges, which can have negative effects on the junction potential. As Chapter 2 demonstrates the existence of surface states at *n*-GaAs/CH_3CN interfaces and how it modifies the junction behavior, the

works presented in Chapters 3 and 4 involve surface modification of Si and the effects on the solid-state junction behaviors. Surface modification can be one of the easiest methods to create stable surface bonds that do not cause the rise of surface states, while also provide a barrier against corrosion or destructive oxidation.

6. References

(1) Tan, M. X.; Laibinis, P. E.; Nguyen, S. T.; Kesselman, J. M.; Stanton, C. E.; Lewis, N. S. *Prog. Inorg. Chem.* **1994**, *41*, 21.

(2) Chapin, D. M.; Fuller, C. S.; Pearson, G. L. *J. Appl. Phys.* **1954**, *25*, 676.

(3) Fahrenbruch, A. L.; Bube, R. H. *Fundamentals of Solar Cells: Photovoltaic Solar Energy Conversion*; Academic: New York, 1983.

(4) Kumar, A.; Wilisch, W. C. A.; Lewis, N. S. *CRC Critical Rev.* **1993**, *18*, 327.

(5) Rhoderick, E. H.; Williams, R. H. *Metal-Semiconductor Contacts*; 2nd ed.; Oxford University Press: New York, 1988.

(6) Sharma, B. L., Ed. *Metal-Semiconductor Schottky Barrier Junctions and Their Applications*; Plenum: New York, 1984.

(7) Sze, S. M. *The Physics of Semiconductor Devices*; 2nd ed.; Wiley: New York, 1981.

(8) Weast, R. C.; Astle, M. J.; Bayer, W. H. *Handbook of Chemistry and Physics*; 71st ed.; CRC Press: Boca Baton, FL., 1991.

(9) Fonash, S. J. *Solar Cell Device Physics*; Academic: New York, 1981.

(10) Lewis, N. S.; Rosenbluth, M. In *Photocatalysis: Fundamentals and Applications*; Serpone, N., Pelizzetti, E., Eds.; John Wiley & Sons: New York, 1989, pp 45.

(11) Crowell, C. R.; Sze, S. M. *Solid State Elec.* **1966**, *9*, 1035.

(12) Memming, R. In *Electroanalytical Chemistry*; Bard, A. J., Ed.; Marcel Dekker, Inc.: New York, 1979; Vol. 11, p 1.

(13) Gerischer, H. In *Physical Chemistry: An Advanced Treatise*; Eyring, H., Henderson, D., Yost, W., Eds.; Academic: New York, 1970; Vol. 9A, pp 463.

(14) Shockley, W.; Read, W. T. *Phys. Rev.* **1952**, *87*, 835.

(15) Hall, R. N. *Phys. Rev.* **1952**, *87*, 387.

Chapter 2

Photoelectrochemical Behavior of *n*-GaAs in Acetonitrile Solutions

1. Introduction

The photoelectrochemical behavior of GaAs/liquid contacts has attracted much attention in attempts to compare theoretical predictions with the experimental behavior of semiconductor electrodes.[1-16] There has been significant controversy regarding the electron-transfer rate constant, k_{et}, at semiconductor/liquid interfaces. While many experimental results and theoretical studies have indicated that the upper bounds on k_{et} is on the order of 10^{-17} to 10^{-16} $cm^4 s^{-1}$,[4,9-11,15-17] other reports have suggested that k_{et} can be as large as 10^{-12} to 10^{-10} $cm^4 s^{-1}$.[7,18-20] Steady-state current density (J) vs. potential (E) data obtained on n-GaAs/CH_3CN-cobaltocenium-cobaltocene $(CoCp_2)^{+/0}$ contacts in the limit where the observed rate does not exhibit the expected second-order rate law (first order in the surface electron concentration and first order in the redox acceptor concentration) have been interpreted to indicate that k_{et} values at semiconductor/liquid contacts can be as high as 10^{-10} cm^4 s^{-1}.[7] Subsequent reports on n-GaAs/CH_3CN contacts have relied upon solvent-suspended quartz crystal microbalance measurements to indicate that both cobaltocene and cobaltocenium adsorb onto the GaAs surface.[8] Assumptions about the effective electron-transfer distance to the adsorbed species, the distance-dependence of the orbital coupling overlap, and the surface coverage of adsorbed electroactive species in this system have then yielded a 10,000-fold reduction in the inferred k_{et} value to $k_{et} \approx 10^{-14}$ cm^4 s^{-1}.[7,8]

It is therefore of great interest and importance to examine in detail the J–E properties of the n-GaAs/CH_3CN interface. The behavior of n-GaAs in contact with CH_3CN has been studied previously by a number of workers. Wrighton and Bard used cyclic voltammetry techniques to conclude that Fermi-level pinning was present at n-GaAs/CH_3CN contacts over a wide range of redox potentials.[21] Nagasubramanian, Wheeler and Bard subsequently reached identical conclusions based on impedance

measurements of *n*-GaAs/CH_3CN contacts.[22] Other studies indicating non-ideal junction behavior of *n*-GaAs electrodes in propylene carbonate, tetrahydrofuran, dimethylformamide, and aluminum chloride-butylpyridinium chloride molten salt electrolyte systems have been reported.[23-31] Reduction of the influence of surface states has, in certain cases, resulted in efficient GaAs-based photoelectrochemical cells, specifically for *n*-GaAs/CH_3CN-ferricenium-ferrocene ($Fc^{+/0}$) contacts.[32,33]

While *J–E* behaviors of *n*-GaAs/CH_3CN contacts with a series of metallocenes have been studied previously in our laboratory, the focus of this chapter involves the investigation of the photoelectrochemical properties of *n*-GaAs/CH_3CN-colbaltocenium-cobaltocene ($CoCp_2^{+/0}$) contacts. The presence of Fermi-level pinning is confirmed by correlating the barrier height obtained for this junction with prior results. This chapter also presents a series of experiments designed to probe the presence of irreversible chemical and/or electrochemical changes on GaAs electrodes during electrochemical process in CH_3CN-$CoCp_2^{+/0}$ solution. These results display the non-ideal behavior of *n*-GaAs/CH_3CN-$CoCp_2^{+/0}$ junction and consequently the invalidity of k_{et} extraction using the *J–E* data from this system.

2. Background

2.1. Determination of the Electron-Transfer Rate Constant at the Semiconductor/Liquid Interface

Current density vs. potential (*J–E*) measurements, in conjunction with kinetic information obtained from impedance measurements, can be useful tools for assessing the electron-transfer rate constants, k_{et} at semiconductor/liquid interfaces. In order to extract robust k_{et} values from the steady-state *J–E* data, the following three conditions must be satisfied.

(1) The electron transfer from the conduction band of a semiconductor to an outer sphere redox acceptor in solution must follow a second-order rate law given by

$$-\frac{d[\mathrm{A}]}{dt} = k_{\mathrm{et}} n_{\mathrm{s}} [\mathrm{A}] \qquad (2.1)$$

where n_s is the concentration of surface electrons in the conduction band, and [A] is the concentration of redox acceptors located near the surface of the semiconductor. The interfacial flux must be shown to be first order in the n_s at the semiconductor surface and first order in the [A] in the solution.[4,34] In this case, interfacial electron transfer dominates the recombination current, and $J_0 = qk_{et}n_s[\mathrm{A}]$. By varying the concentration of redox acceptors, V_{oc} should change accordingly.

A prior study of *n*-GaAs/CH_3CN-$Fc^{+/0}$ contacts in our laboratory had shown that a change of two orders of magnitude of [A] and [A^-], while the solution potential remained constant, produced no change in V_{oc} value at a constant light intensity. There was also no change in V_{oc} at a constant photocurrent density as [A] was increased from 0.5 mM to 33.4 mM while [A^-] remained constant.[35] This result clearly demonstrated that the

variation in [A] did not affect the interfacial flux, and therefore interfacial electron transfer current does not dominate the recombination current.

(2) The semiconductor band edges do not move with changes in the concentration of the redox acceptor species. Otherwise, the validation of the rate law is hindered when both variables of the rate law, n_s and [A], are simultaneously changed.

If the band edges stay at the same positions when the redox potential is varied, then the barrier height of the junction, which is the difference between the semiconductor conduction band edge and the solution redox potential, should change linearly with the changes in the redox potential of the contacting solution. When this relationship is not observed, the junction is Fermi-level pinned, and the band edges could shift with changes in the cell potential. A prior investigation on Fermi-level pinning at *n*-GaAs/CH_3CN junctions was conducted by measuring the V_{oc} values at different cell potentials,[35] and is presented in section 2.2 of this chapter. Although the relationship between the V_{oc} and the cell potential can provide an indication for the degree of Fermi-level pinning, the observed changes in V_{oc} could also be caused by reasons other than the band edge movement. For example, the interfacial electron transfer current could increase with changes in the equilibrium barrier height at the interface, or the surface-state recombination current could have increased due to the changes in equilibrium occupation fraction of the surface states. Since these conditions are capable of affecting the measured V_{oc} values as well, the barrier height measurement would be essential for confirming the presence of Fermi-level pinning.

(3) The capture of the electrons by surface states does not compete kinetically with the direct electron transfer from the semiconductor to the redox acceptor species.[4,34,36-39] The surface states can either be intrinsic or arise from adsorption of the redox species. If the semiconductor surface reacts with the contacting solution, it is a good indication that the surface-state process dominates the interfacial kinetics.

The investigation of n-GaAs surface reaction in contact with CH$_3$CN-CoCp$_2^{+/0}$ is one of the main focuses of this chapter. The V_{oc} of this junction was larger than expected at such a negative cell potential, which is fairly close to the GaAs conduction band edge. If the GaAs surface is modified during the electrochemical operation in this solution, the extraction of k_{et} value from the steady-state J–E data of this junction would certainly not be possible.

2.2. Fermi-Level Pinning

In an ideal situation, a change in the redox potential of the solution should result in a defined change in the barrier height (ϕ_b) of the junction; however, this behavior is not always observed experimentally. When a reliable barrier height measurement technique was unavailable, open-circuit photovoltages, V_{oc}, were measured and related to the thermodynamic quantities for the investigation of the Fermi-level pinning. For an n-type semiconductor when the interfacial electron transfer is the dominating recombination process, V_{oc} can be related to the build-in voltage (V_{bi}) according to the equation:

$$V_{oc} = \frac{kT}{q} \ln\left(\frac{J_{ph}}{qN_c k_{et}[A]}\right) + V_{bi} \tag{2.2}$$

However, if the interfacial electron transfer current is much less than the total recombination current, then the inequality in Equation 2.2 must hold. Since $\phi_b = V_{bi} + (kT/q)\ln(N_c/N_d)$, V_{oc} can be related to ϕ_b as follows:

$$V_{oc} < \frac{kT}{q} \ln\left(\frac{J_{ph}}{qN_c k_{et}[A]}\right) + \phi_b \tag{2.3}$$

The electrochemical behavior of a series of n-GaAs/CH$_3$CN contacts has been investigated over a significant range of Nernstian solution potentials, $E(A/A^-)$, in order to

ascertain whether "ideal" behavior of the V_{oc} vs. $E(A/A^{-})$ is observed for these contacts, or whether Fermi-level pinning, which would lead to apparent band edge shifts as $E(A/A^{-})$ is changed,[21] is present in these systems. The former condition is required for a straightforward extraction of k_{et} values from J–E data, while, in contrast, the latter behavior has been observed in prior cyclic voltammetry and impedance measurements of n-GaAs/CH_3CN contacts.[22,40-42]

Several different metallocene-based redox couples, spanning a wide range of formal potentials, $E^{o\prime}(A/A^{-})$, were used to produce a variation in the Nernstian potentials of the electrolyte solutions from –1.2 V to +0.2 V vs. SCE. Figure 2.1 displays the V_{oc} of each system recorded at a light intensity sufficient to provide a photocurrent density of 1 mA cm^{-2} at each n-GaAs/CH_3CN contact. Despite a change of over 1.2 V in $E(A/A^{-})$ between the n-GaAs/CH_3CN-$Co(C_5H_4CH_3)_2^{+/0}$ and the n-GaAs/CH_3CN-$Fc^{+/0}$ contacts, the V_{oc} only changed by ~0.3 V.[43] In the ideal model of semiconductor photoelectrochemistry, the V_{oc} should be linearly dependent on $E(A/A^{-})$, with a slope close to unity, for a homologous series of redox species. Instead, a much weaker dependence of V_{oc} was observed as $E(A/A^{-})$ was varied, and the presence of Fermi-level pinning in this system over the range of potentials investigated was indicated. Furthermore, for $E(A/A^{-})$ more negative than –0.80 V vs. SCE, the measured V_{oc} values that are larger than expected from the linear region signals the possibility of a chemical reaction between the n-GaAs and CH_3CN-based electrolyte under the conditions explored.

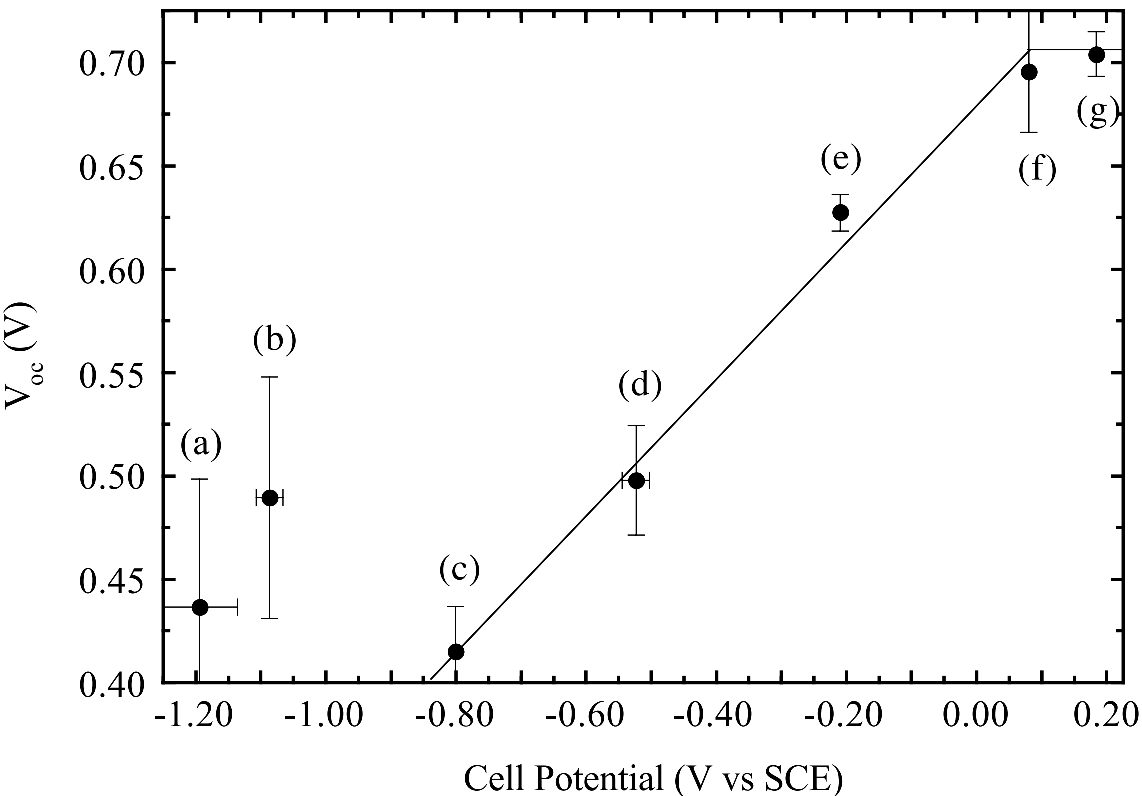

Figure 2.1

Open-circuit photovoltage vs. equilibrium cell potential for the *n*-GaAs/CH_3CN-$LiClO_4$ system at J_{ph} = 1.0 mA cm^{-2}. The redox couples used for this system are (a) $Co(C_5H_4CH_3)_2^{+/0}$, (b) $CoCp_2^{+/0}$, (c) $[CoCp(C_5H_4CO_2CH_3)]^{+/0}$, (d) $Co(C_5H_4CO_2CH_3)_2^{+/0}$, (e) $Fe[C_5(CH_3)_5]_2^{+/0}$, (f) $Fe(C_5H_4CH_3)_2^{+/0}$, (g) $FeCp_2^{+/0}$.[43]

3. Experimental

3.1. Electrode Material and Etching

Single-crystal Si-doped (100)-oriented *n*-GaAs (Laser Diode Co.) with dopant density, N_d, of (0.9–1.9) $\times 10^{17}$ cm^{-3} and wafer thickness of 400–500 μm were used. Ohmic contacts were prepared by thermal evaporation of a 1000 Å layer of 98% Au:2% Ge alloy (Alfa Aesar) or 88% Au:12% Ge alloy (Aesar) on the unpolished side of the wafers, followed by annealing in forming gas at 475 °C for 5 minutes.[33] Electrodes were fabricated by attaching a tinned copper wire (22 AWG, Belden) to the ohmic contact using electrically conductive silver print (GC Electronics). The wire was encased in glass tubing and the backside and edges of the electrode were sealed with insulating white epoxy (Epoxy Patch Kit 1C, Dexter Corp.), leaving only the polished surface of the crystal exposed. Electrode areas were determined by digitizing magnified scanned images of the electrode along with a micro ruler using ImageSXM program. The typical exposed electrode areas were 0.15–0.25 cm^2.

For surface x-ray photoelectron spectroscopy (XPS) studies, either 2 mm $\times$ 4 mm size samples or electrodes with surface areas of 0.10–0.15 cm^2 were used. To investigate the surface property of GaAs following the electrochemical measurements, the length of the electrode glass tubing had to be reduced before it could be brought into the ultrahigh vacuum (UHV) system for XPS analysis. Prior to electrochemical experiments, the glass tubing that encases the tinned copper wire was pre-cut at ~1 inches from the epoxy and reconnected with heat-shrink tubing. The upper part of the glass tubing can then be easily removed after the electrochemical experiment by cutting away the heat-shrink tubing. With the wire folded back, the electrode can be mounted onto a stub and introduced into the UHV chamber. For some electrodes the glass tubing was replaced

with flexible polyethylene tubing, and the wire encased in polyethylene tubing can be folded back so the length of the electrode is less than 1.5 inches. These electrodes could be reused for electrochemical experiments by either unfolding the wire and reconnecting the glass tubing or unfolding the polyethylene tubing.

The *n*-GaAs working electrodes were initially etched in a 4:1:1 H_2SO_4(aq):H_2O_2 (30%):H_2O solution, rinsed with 18.0 MΩ·cm resistivity H_2O (obtained from a Barnstead Inc. Nanopure water purification system) and CH_3CN, and dried under flowing N_2(g) before being taken into the N_2(g)-purged glove box. This oxidizing etch is known to remove ~1 μm of wafer thickness per minute.[43] Between experiments, the electrode surfaces were etched in a solution of 0.05% (v/v) Br_2 (EM Science) in CH_3OH (EM Science) followed by immersion in a 4.0 M solution of NH_3 in CH_3OH, which was prepared by bubbling NH_3(g) through CH_3OH until the desired concentration was achieved. The etching cycle was repeated three times, rinsed again in CH_3OH, and dried with N_2(g).[44,45] This procedure has been shown to give an oxide free stoichiometric surface with a mirror finish.[32,46,47]

3.2. Solvents and Reagents

Methanol (CH_3OH) and acetonitrile (CH_3CN) were obtained from EM Science or Aldrich. The CH_3OH was distilled over magnesium turnings prior to use. The CH_3CN was predried over CaH_2 and then dried over P_2O_5 and stored over activated 3 Å sieves (EM Science). Both solvents were distilled, collected and stored under N_2(g). Ferrocene (Fc, Aldrich) and cobaltocene ($CoCp_2$, Strem or Aldrich) were sublimed *in vacuo*. Ferrocenium tetrafluoroborate ($FcBF_4$) was purchased from Aldrich or prepared as previously described,[48] and was dried *in vacuo* at room temperature before use. Colbaltocenium hexafluorophosphate ($CoCp_2PF_6$) was purchased from Aldrich or prepared via the method of Sheats and Rausch,[49] and was recrystallized from CH_3CN and

dried *in vacuo* at room temperature. Lithium perchlorate ($LiClO_4$, Aldrich or J.T. Baker) was dried by fusing at 280 ˚C under active vacuum in a quartz tube.[50] All solid reagents were stored and weighed out in a N_2(g)-purged drybox until use.

3.3. Electrochemical Measurements

A standard three-electrode potentiostatic setup was used for all electrochemical measurements. The reference electrode was a Pt wire poised at the Nernstian solution potential, and the counter electrode was a Pt gauze of area at least 10 times larger than that of the working electrode. Both Pt reference and counter electrodes were cleaned by immersion in a 3:1 (v/v) solution of concentrated HCl(aq) (EM Science) and concentrated HNO_3(aq) (EM Science) prior to being taken into the N_2(g)-purged glove box. Typical cell solutions for *n*-GaAs/CH_3CN-$CoCp_2^{+/0}$ studies consist of 10mM $CoCp_2$, 10 mM $CoCp_2PF_6$, and 0.7 M $LiClO_4$ in CH_3CN. Typical cell solutions for *n*-GaAs/CH_3CN-$Fc^{+/0}$ studies consist of 90 mM Fc, 0.5 mM $FcBF_4$, and 0.7 M $LiClO_4$ in CH_3CN. The cell solutions were magnetically stirred, and the cell potential was periodically measured relative to a methanoic SCE. All electrochemical experiments were carried out in a N_2(g)-purged glove box that had less than 10 ppm of O_2 as verified by the lack of fuming of $(CH_3CH_2)_2Zn$.

3.3.1. Impedance Measurements

The impedance measurements were performed on a Schlumberger Instruments Model 1260 impedance/gain-phase analyzer equipped with a Solartron 1286 Electrochemical Interface. A 10 mV ac signal with a frequency sweep from 100 Hz to 100 kHz was superimposed upon a reverse dc bias stepped in 50 mV intervals between 0.4 and 1.0 V vs. Nernstian solution potential, $E(A/A^-)$. The impedance analyzer measures the total impedance, Z, and the phase angle, θ, between Z and the input ac

signal. The real and imaginary components of the impedance, Z_{re} and Z_{im}, respectively, can then be calculated using the relationships $Z_{re} = Z\cos\theta$ and $Z_{im} = Z\sin\theta$.

The impedance data were fit to an equivalent circuit consisting of a resistor, R_s, representing the resistive loss across cell solution and lead, in series with a parallel circuit containing a differential capacitance of the semiconductor space-charge region, C_{sc}, and a space-charge resistance, R_{sc}, representing resistance to Faradaic charge transfer (Figure 2.2). This model assumes that the measured differential capacitance, C_{diff}, equals C_{sc}. The differential capacitance was computed from the impedance data using the equation:[51]

$$2\pi f C_{\text{diff}} = \frac{1 + \sqrt{1 - 4{Z_{\text{im}}}^2 / {R_{\text{sc}}}^2}}{2Z_{\text{im}}} \tag{2.4}$$

where f is the frequency of the ac signal and Z_{im} is the imaginary part of the measured impedance at the dc bias of interest. The R_{sc} value at each dc bias was extracted from the circular fit of the Nyquist plot. A Nyquist plot is a plot of Z_{im} vs. Z_{re} that shows the branching between these two components of the measured impedance as a function of f. At a high frequency, the effective impedance of the capacitor is small relative to R_{sc} and the C_{sc}'s contribution to Z_{im} falls to zero. As most of the current flows through the C_{sc} pathway, the observed impedance is simply R_s. At a low frequency, the effective impedance of the capacitor is high relative to R_{sc}, therefore most of the current flows through the R_{sc} pathway, and the observed impedance is $R_{sc} + R_s$. In the intermediate-frequency range, the changes in frequency translate directly into the changes in the effective impedance of the capacitor, therefore the magnitude of Z is dictated by C_{sc}. The differential capacitance measurements were performed in this capacitive frequency regime where the Faradaic charge transfer pathway is suppressed.

The differential space-charge capacitance was then related to the built-in voltage V_{bi} of the semiconductor/liquid junction by the Mott-Schottky equation:[34]

$$C_{\mathrm{sc}}^{-2} = \frac{2}{qN_{\mathrm{d}}\varepsilon\varepsilon_0 A_{\mathrm{s}}^2}\left(E + V_{\mathrm{bi}} - \frac{kT}{q}\right) \tag{2.5}$$

where ε is the dielectric constant of the semiconductor, ε_0 is the permittivity of free space, N_{d} is the semiconductor dopant density, A_{s} is the electrode surface area, E is the applied dc potential. By plotting C_{diff}^{-2} vs. E (i.e., a Mott-Schottky plot) for each frequency and extrapolating the linear regression of these data points to infinite capacitance, the V_{bi} of the solid/liquid junction was calculated. To assess the validity of the equivalent circuit model used in this experiment, the measured semiconductor dopant density was computed from the slope of the linear fit of C_{diff}^{-2} vs. E and compared to the value specified by the manufacturer. Only electrodes which exhibited linear Mott-Schottky plots (R^2 .≥ 0.999, where R is the correlation coefficient) and had measured dopant densities within the range specified by the manufacturer were included in the analysis. Electrodes that yielded nonlinear or frequency-dependent plots were considered defective.

3.3.2. Steady-State Current Density vs. Potential Characteristics

Current density vs. potential (J–E) measurements were performed using a Solartron Model 1287 potentiostat or an EG&G Princeton Applied Research (PAR) Model 173 potentiostat/galvanostat equipped with an EG&G PAR Model 175 universal programmer. When EG&G PAR Model 173 potentiostat/galvanostat was used, traces were recorded on a Houston Instruments Omnigraphic 2000 recorder at a scan rate of 50 mV s^{-1}. Light intensities were controlled by the use of a 300 W ENH-type tungsten-halogen bulb in conjunction with neutral density filters (Hoya Optics). Open-circuit voltages (V_{oc}) were obtained with the sample held at open-circuit, and photocurrents (I_{ph}) were obtained with the samples held at 0.4 V vs. the cell potential $E(\mathrm{A/A^-})$. Photoresponse measurements were performed for both both n-GaAs/CH_3CN-$CoCp_2^{+/0}$ and n-GaAs/CH_3CN-$Fc^{+/0}$ junctions. The values of V_{oc} and J_{ph} were collected at different

light intensities by reading the appropriate quantities through a Fluke 27 digital multimeter. The diode quality factors (γ) and the reverse saturation current density (J_0) were extracted using the equation:[52]

$$V_{oc} = \frac{\gamma kT}{q} \ln\left(\frac{J_{ph}}{J_0}\right) \quad (2.6)$$

where k is Boltzmann's constant, T is the temperature, and q is the charge on the electron.

The *J–E* characteristics of both *n*-GaAs/CH_3CN-$CoCp_2^{+/0}$ and *n*-GaAs/CH_3CN-$Fc^{+/0}$ systems were collected mainly to confirm the reproducibility of results from prior studies in the Lewis group. Before and after each impedance measurement, the *J–E* data were obtained to verify that the properties of the electrode remained unchanged over the time scale of the impedance study. To investigate the possibility of surface change during the electrochemical experiments of *n*-GaAs in CH_3CN-$CoCp_2^{+/0}$ solution, the *J–E* data of an *n*-GaAs/CH_3CN-$Fc^{+/0}$ contact before and after potential scans in CH_3CN-$CoCp_2^{+/0}$ solution were also collected. This experiment was performed in an attempt to observe any effect on the *J–E* properties of *n*-GaAs after electrochemical measurements in contact with CH_3CN-$CoCp_2^{+/0}$ solution. An etched *n*-GaAs electrode was first immersed in CH_3CN-$Fc^{+/0}$ solution and a series of *J–E* curves were recorded in the dark and at five different light intensities. The electrode was rinsed with CH_3CN before exposing to CH_3CN-$CoCp_2^{+/0}$ solution where three types of potential scans were performed to age the electrode. Following another CH_3CN rinse, the electrode was returned to the CH_3CN-$Fc^{+/0}$ solution and another series of *J–E* curves were obtained.

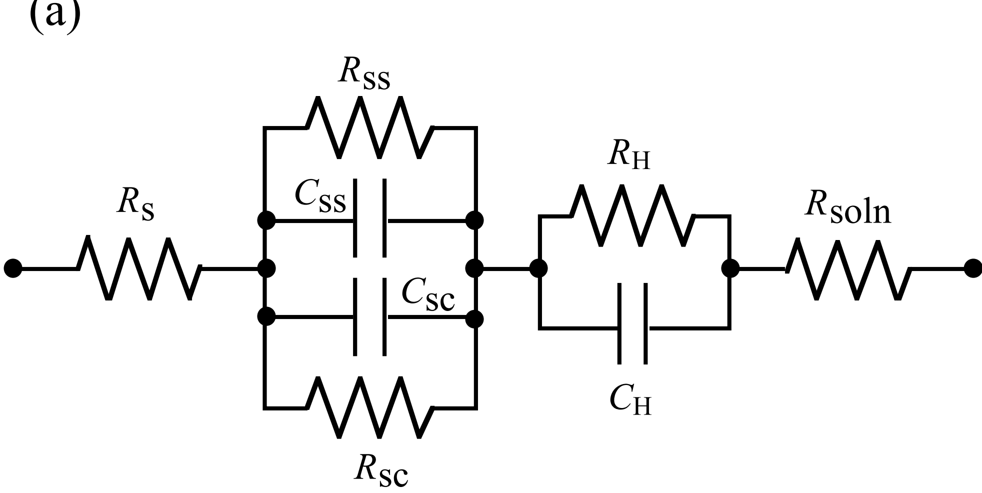

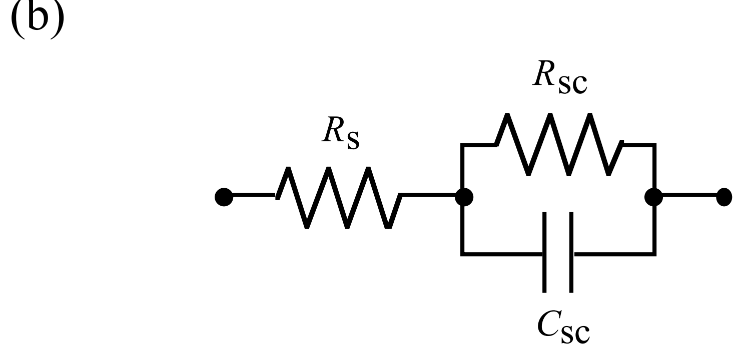

Figure 2.2

(a) A circuit of a semiconductor/liquid junction and (b) a simplified equivalent circuit of a semiconductor/liquid junction at high enough frequencies where surface states cannot react fast enough to the applied ac signal. R_s is the semiconductor bulk resistance, R_{ss} is the surface state resistance, C_{ss} is the surface state capacitance, R_{sc} is the space-charge resistance, C_{sc} is the space-charge capacitance, R_H is the Helmholtz layer resistance, C_H is the Helmholtz layer capacitance, and R_{soln} is the cell solution resistance.

3.4. Surface Analysis of *n*-GaAs in Contact with CH_3CN-$CoCp_2^{+/0}$ Solution

3.4.1. X-ray Photoelectron Spectroscopy

The chemistry of *n*-GaAs after exposure to CH_3CN-$CoCp_2^{+/0}$ solution was investigated with x-ray photoelectron spectroscopy (XPS). Immediately before the experiment all samples were etched in a N_2(g)-purged glove box using the procedure described in section 3.1. Four samples without back ohmic contacts were immersed in the following four CH_3CN solutions for 10 minutes each. Solution 1 contained 0.7 M $LiClO_4$, solution 2 contained 0.7 M $LiClO_4$ and 10 mM $CoCp_2$, solution 3 contained 0.7 M $LiClO_4$ and 10 mM $CoCp_2PF_6$, and solution 4 contained 0.7 M $LiClO_4$ and 10 mM each of both $CoCp_2$ and $CoCp_2PF_6$. In order to analyze the *n*-GaAs surfaces after electrochemical processes, customized electrodes with pre-cut glass tubing or flexible polyethylene tubing which allowed the length of these electrodes to be reduced to less than 1.5 inches were used. The electrode was immersed in an electrochemical cell with solution 4, and a potential sweep at 50 mV s^{-1} between –0.5 and 0.3 V vs. $E(A/A^-)$ was applied for 10 minutes. All samples were rinsed with CH_3CN and sealed in vials under N_2(g).

The vials were transferred into another N_2(g)-purged glove box which is connected directly to the ultrahigh vacuum (UHV) system that houses the XPS via a high-vacuum load lock. The non-ohmic contacted GaAs samples were mounted on a stainless steel or aluminum stub with gold-plated molybdenum clips or screws. A custom-made aluminum stub designed to hold tubing down was used to mount the shortened electrodes. The tinned copper wire of the electrode was fold back to make an electrical contact with the stub. The samples stub was introduced into the load lock through a gate valve inside of the glove box. A Varian V-200 turbo pump backed by a Varian model SD-300 mechanical pump were used to evacuate the load lock to

approximately 10^{-7} Torr prior to transferring the samples into the UHV system. The XPS experiments were conducted in an M-probe surface spectrometer (Surface Science Instrument) pumped by a CTI Cryogenics-8 cryo pump. The XPS chamber was maintained at a base pressure of less than 5×10^{-10} Torr, although the operating pressure was 5×10^{-9} to 2×10^{-8} Torr. Monochromatic Al K_α x-rays (hν = 1486.6 eV) incident at 35° from the sample surface were used to excite electrons from the sample, while the emitted electrons were collected by a hemispherical analyzer at a take-off angle of 35° from the plane of the sample surface. Data collection and analysis were done with the M-probe package software version 3.4. The survey scan was collected in the scanned mode with an elliptical spot of dimensions 800 μm × 1200 μm incident on the sample surface.

3.4.2. Cyclic Voltammetry

The possibility of surface changes when *n*-GaAs underwent electrochemical measurements in CH_3CN-$LiClO_4$ system was further investigated by the cyclic voltammetry. Cyclic voltammograms of *n*-GaAs in a standard electrolyte solution were collected using a Solartron Model 1287 potentiostat. A three-electrode potentiostatic setup was used with a SCE as the reference electrode and a large Pt as the counter electrode. The cell solution was unstirred and consists of 0.7 M $LiClO_4$ in CH_3CN, in the absence of a redox-active species. The data were collected from 2.0 to –2.5 V vs. SCE with a scan rate of 50 mV s^{-1}.

4. Results

4.1. Differential Capacitance vs. Potential Results and the Barrier Height of *n*-GaAs/CH_3CN-$CoCp_2^{+/0}$ Contacts

The barrier height of the *n*-GaAs/CH_3CN-$CoCp_2^{+/0}$ junction was calculated from electrochemical impedance data. The barrier height (ϕ_b) of the junction can be calculated from the V_{bi} from the following equation:[53]

$$\phi_b = V_{bi} + \frac{kT}{q}\ln\left(\frac{N_c}{N_d}\right) \tag{2.8}$$

where N_c is the effective density of states in the conduction band.

Typical representations of one set of impedance data for the *n*-GaAs/CH_3CN-$CoCp_2^{+/0}$ system are shown in Figure 2.3. To determine a relevant frequency range for the Mott-Schottky analysis (i.e., barrier height calculation), a plot of log |Z| vs. log f (Bode plot) and a plot of the phase angle θ vs. log f were used. A linear dependence of the total impedance on frequency (a linear region on the Bode plot) with a slope of 1 indicates the dominance of the space-charge capacitance in the circuit model illustrated in Figure 2.2b. Figure 2.3a displays the measured circuit impedance as a function of frequency in Bode plot form for a representative electrode at applied potentials of 0.40 V and 1.00 V vs. $E(A/A^-)$. For 100 Hz $< f <$ 50 kHz range, the mean slope of the Bode plots between 0.40 V and 1.00 V vs. $E(A/A^-)$ was –0.995 ± 0.001, which means that the differential capacitance was independent of the measured frequency. Another criterion for the space-charge capacitance dominance was a measured phase angle of ≈ 90°. For the work done in this chapter, only the frequencies with phase angles above 80° were used, and this frequency range was found to be between 100 Hz and 50 KHz (Figure

2.3b). During the subsequent analysis, only frequencies that yielded linear fits with $R^2 \geq$ 0.999 were used to calculate the barrier height values. Figure 2.3c displays a typical Nyquist plot of the n-GaAs/CH_3CN-$CoCp_2^{+/0}$ interface. The R_{sc} values were very large in all cases, which again confirmed the relevance of the frequency range selected. Figure 2.4a display a Mott-Schottky plot at six different measured frequencies, and Figure 2.4b shows the extrapolated linear fits to these data. For this particular set of data, the average extrapolated x-intercept for 9 different measured frequencies was –0.740 ± 0.009 V, and using Equation 2.10, the V_{bi} was calculated to be 0.765 ± 0.009 V. From Equation 2.11, the ϕ_b of this electrode was found to be 0.902 ± 0.009 V. The mean observed Mott-Schottky plot slope of $(1.400 \pm 0.014) \times 10^{15}$ F^{-2} V^{-1} yielded a measured dopant density of $(1.41 \pm 0.01) \times 10^{17}$ cm^{-3}, which is in good agreement with that specified by the manufacturer. The mean barrier height calculated from 8 samples with a total of 17 trials was 0.915 ± 0.054 V and the mean calculated dopant density was $(1.16 \pm 0.15) \times 10^{17}$ cm^{-3}, which is also in good agreement with that specified by the manufacturer.

Figure 2.3

(a) A representative Bode plot (impedance |*Z*| vs. frequency *f*), (b) a plot of phase angle vs. log *f* , and (c) a Nyquist plot (Z_{im} vs. Z_{re}) for the *n*-GaAs/CH_3CN-$CoCp_2^{+/0}$ junction at an applied potential of +0.4 V vs. $E(A/A^-)$ (filled circles) and +1.0 V vs. $E(A/A^-)$ (open circles). The redox couple concentrations were [A] = [A^-] = 10 mM, and $E(A/A^-)$ was –0.887 V vs. SCE.

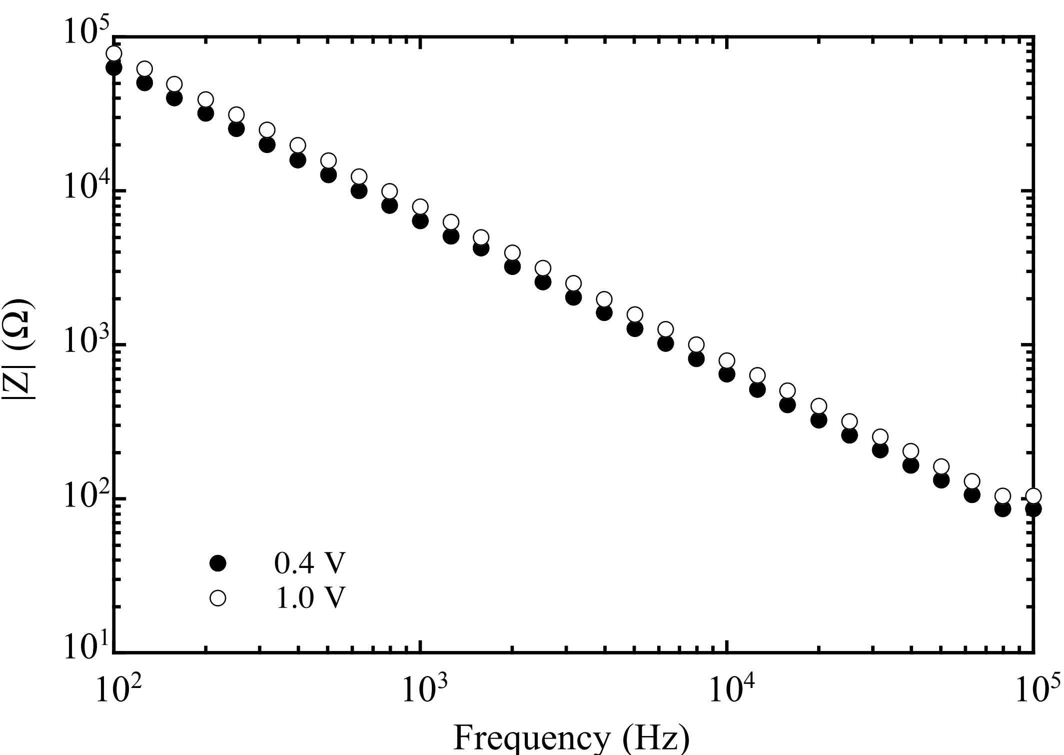

Figure 2.3a

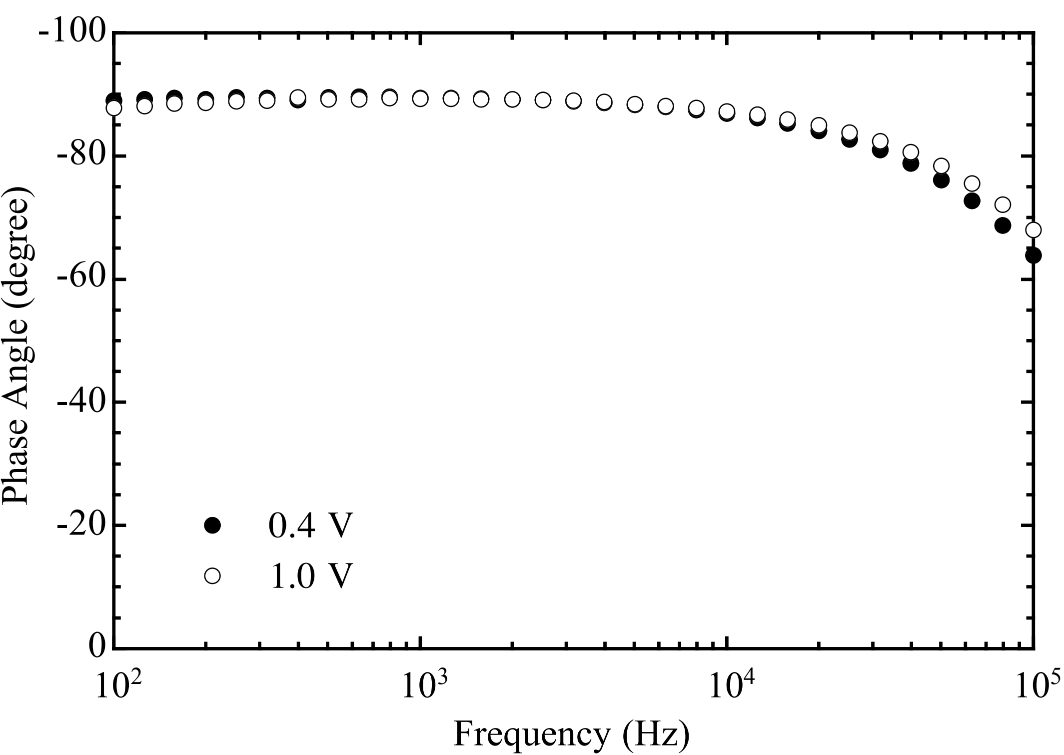

Figure 2.3b

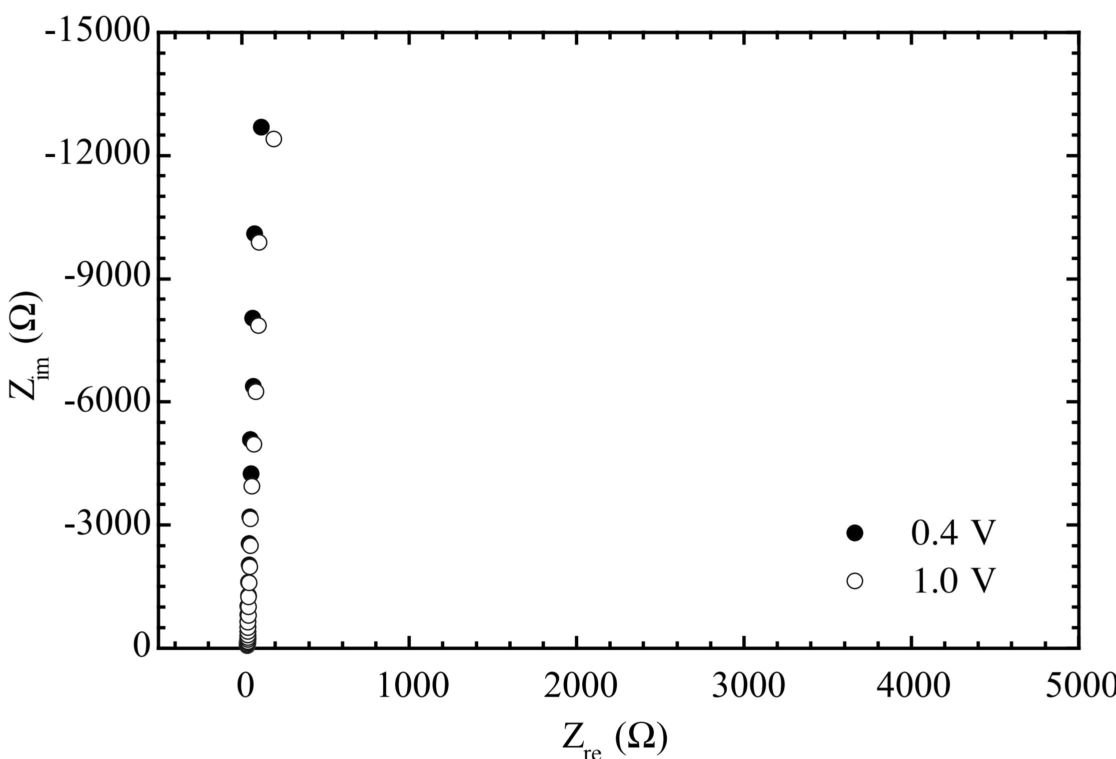

Figure 2.3c

Figure 2.4

(a) Mott-Schottky plot of the *n*-GaAs/CH_3CN-$CoCp_2^{+/0}$ junction. (b) The linear extrapolations of data shown in (a), and all linear fits yielded correlation coefficients of 0.999 or greater. The measuring frequency range shown is 100 Hz to 10 kHz. For this electrode, the ϕ_b was calculated to be 0.902 ± 0.009 V and the measured dopant density was $(1.41 \pm 0.01) \times 10^{17}$ cm^{-3}. The total cell resistance was ~37 Ω.

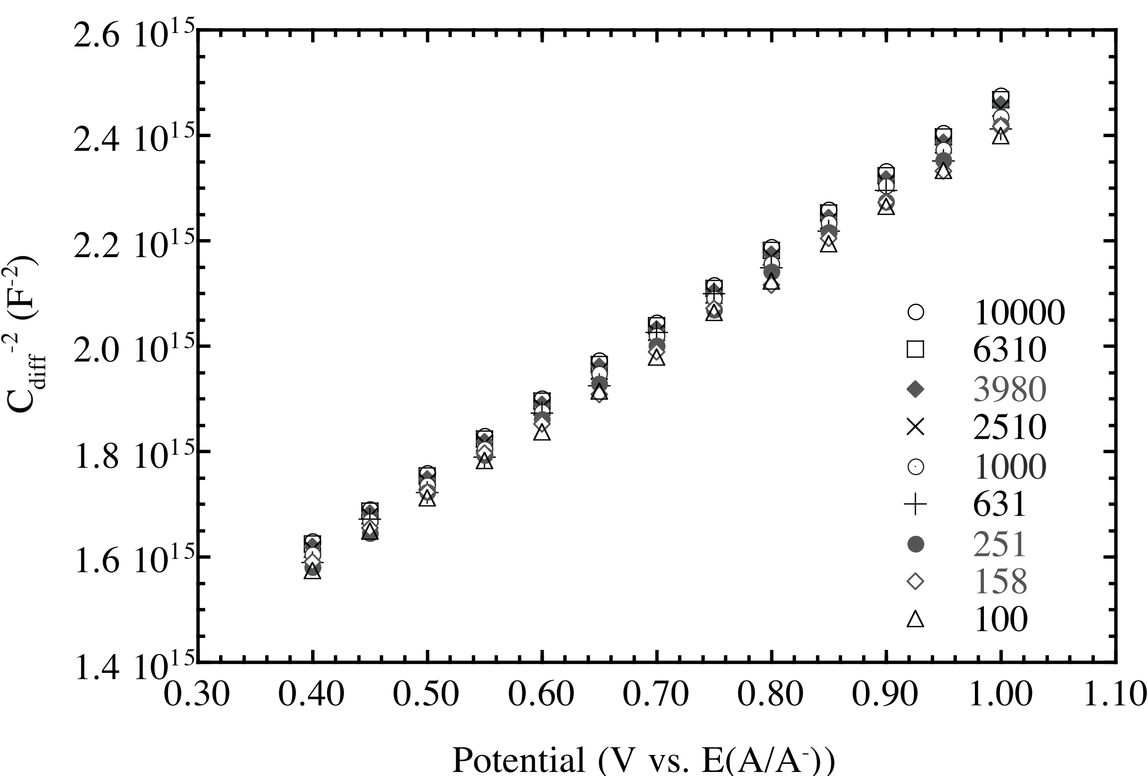

Figure 2.4a

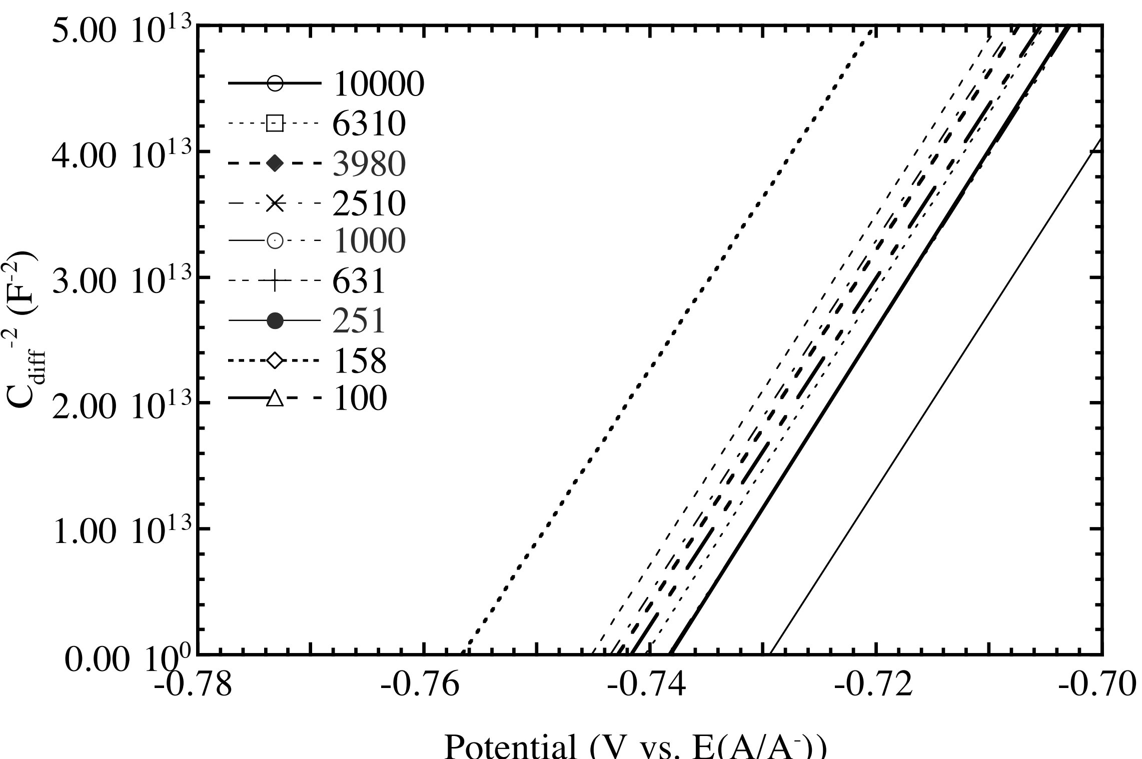

Figure 2.4b

4.2. Steady-State *J–E* Behavior of *n*-GaAs/CH_3CN-$CoCp_2^{+/0}$ Contacts

4.2.1. *J–E* Data for *n*-GaAs electrodes in CH_3CN-$CoCp_2^{+/0}$ solutions

Figure 2.5 displays a typical current density vs. potential (*J–E*) data for *n*-GaAs in contact with CH_3CN-10 mM $CoCp_2$-10 mM $CoCp_2PF_6$ solution in the dark and at several different light intensities. At higher illumination intensities, typically at J_{ph} above 0.7 mA cm^{-2}, the *J–E* curves exhibited hysteresis behavior indicating possible surface reaction. The sensitivity of the *n*-GaAs material on the solution quality could be observed in Figure 2.6. The *J–E* data was collected in the same solution except that CH_3CN was distilled only once over CaH_2, and in this case the hysteresis occurred even at lower J_{ph} values. The electrode surfaces were sometimes damaged to a point that the standard chemical etch could not repair the electrode. For this reason, an extra step was taken to distill CH_3CN over P_2O_5 after CaH_2, and the light intensity was carefully controlled not to overexpose the electrode surfaces.

4.2.2. Photoresponses of *n*-GaAs electrodes in CH_3CN-$CoCp_2^{+/0}$ and CH_3CN-$Fc_2^{+/0}$ solutions

For *n*-GaAs/CH_3CN-$CoCp_2^{+/0}$ junctions, the average calculated diode quality factor was 1.48 ± 0.08, and the mean calculated V_{oc} value was 320 ± 14 mV at J_{ph} = 1 mA/cm^2. For *n*-GaAs/CH_3CN-$Fc^{+/0}$ junctions, the average calculated diode quality factor was 1.51 ± 0.05, and the mean calculated V_{oc} value was 718 ± 24 mV at J_{ph} = 20 mA/cm^2. The diode quality factors for both contacts are in good agreement with obtained values from prior work. The V_{oc} values observed are, however, lower than the previously observed value of 490 ± 60 mV in CH_3CN-$CoCp_2^{+/0}$ and 822 ± 4 mV in CH_3CN-$Fc^{+/0}$ at the same J_{ph}. The electrode material used for prior study was of high quality epitaxial *n*-GaAs samples, and this difference in semiconductor quality was perceived to cause this

discrepancy in V_{oc} values. A white-silvery film was observed on the electrode surface after each experiment in CH_3CN-$CoCp_2^{+/0}$ solution, in addition, some white-silvery powders were also observed in the cell solution after electrochemical measurements were made using several electrodes.

4.2.3. Effects of Exposure to CH_3CN-$CoCp2^{+/0}$ Solutions on the Behavior of *n*-GaAs/CH_3CN-$Fc^{+/0}$ Contacts

Since *J–E* behavior of *n*-GaAs in contact with CH_3CN-$Fc^{+/0}$ solution was stable and reproducible. Comparing the *J–E* curves of this junction before and after the electrode was exposed to CH_3CN-$CoCp2^{+/0}$ solutions could help identify if surface modification took place in $CoCp_2^{+/0}$ solution. Figure 2.7a displays *J–E* behaviors of *n*-GaAs/CH_3CN-$Fc^{+/0}$ contact immediately following the etching process. After the electrodes were subjected to potential scans in CH_3CN-$CoCp2^{+/0}$ solutions, the *J–E* data of *n*-GaAs/CH_3CN-$Fc^{+/0}$ contact, as displayed in Figure 2.7b, exhibited decreased forward bias current density that was roughly half of the magnitude of the original value. Slightly lowered J_{ph} values at identical illumination intensities was also observed, although the values of V_{oc} did not change by much. The decreased cathodic current suggested that the interface between the *n*-GaAs and CH_3CN-$Fc^{+/0}$ solution was altered when the electrode was exposed to the CH_3CN-$CoCp2^{+/0}$ solution. The results here also indicate the possibility of surface reaction between the electrode surface and the CH_3CN-$CoCp2^{+/0}$ solution.

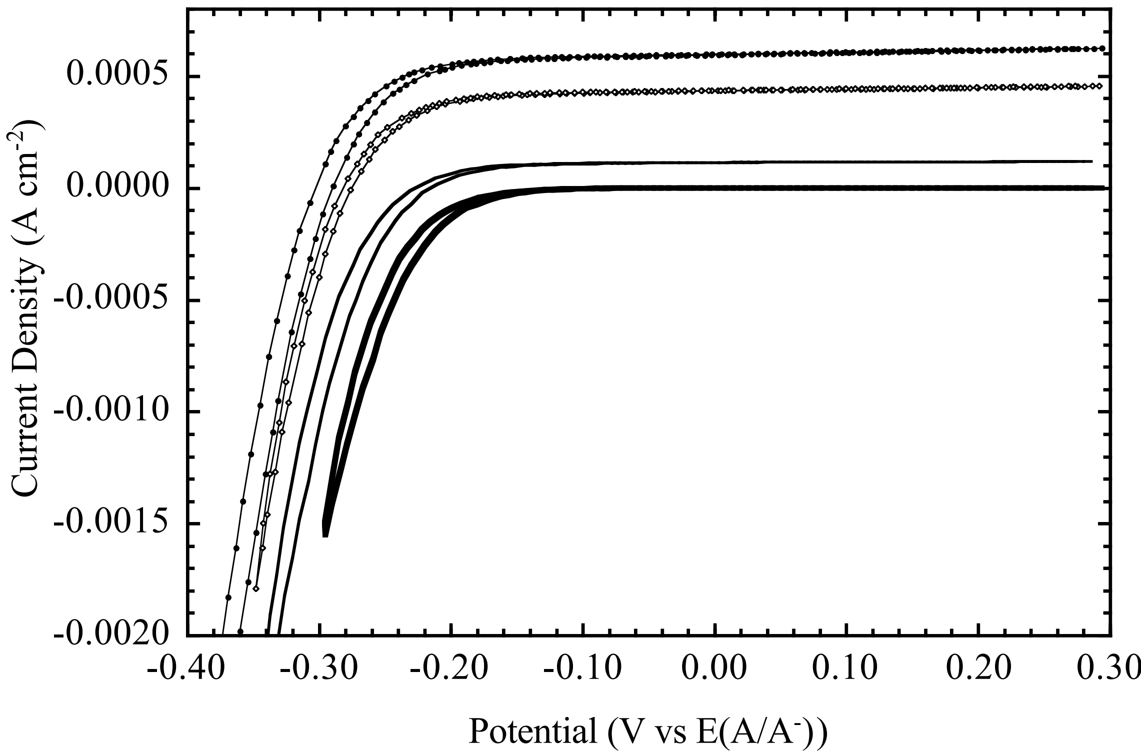

Figure 2.5

Representative *J–E* behaviors of *n*-GaAs electrodes in contact with CH_3CN-$CoCp_2^{+/0}$ solution in the dark and at three light intensities. The electrode area was 0.2661 cm^2. The cell solution consists of $CoCp_2$ (10 mM), $CoCp_2PF_6$ (10 mM), and $LiClO_4$ (0.7 M) in CH_3CN. The scan rate was 50 mV s^{-1}.

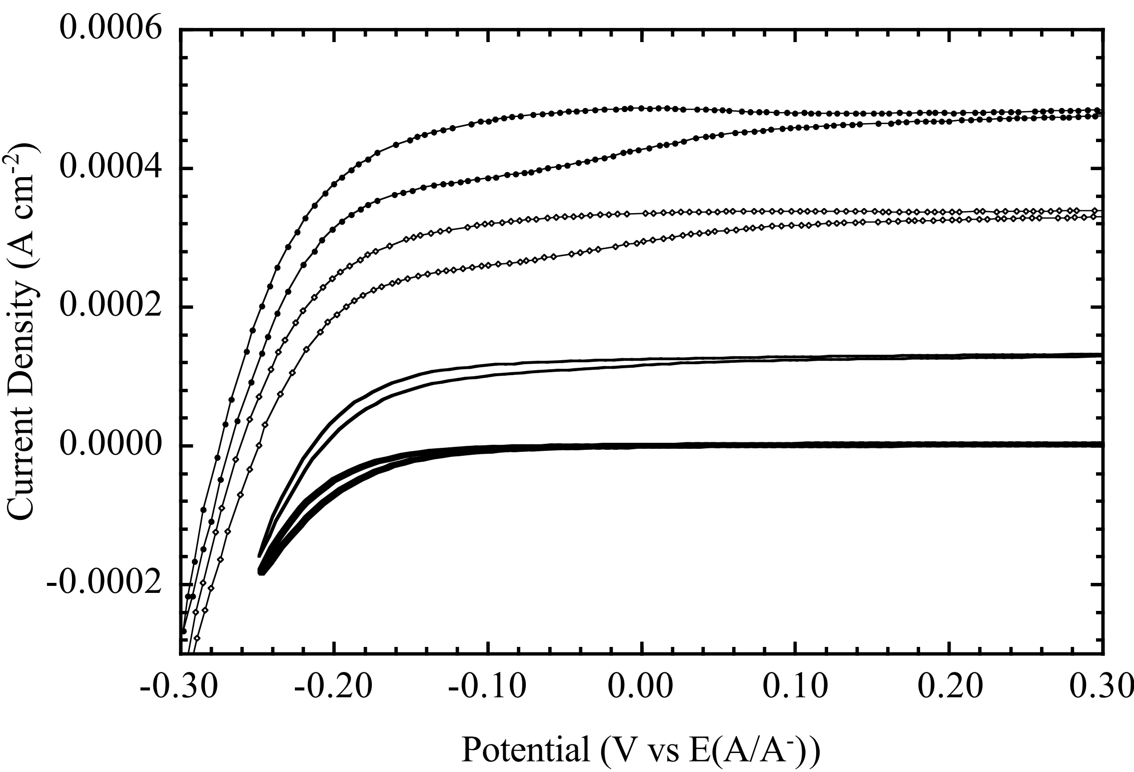

Figure 2.6

Representative *J–E* behaviors of *n*-GaAs electrodes in contact with slightly wet CH_3CN-$CoCp_2^{+/0}$ solution in the dark and at three light intensities. The electrode area was 0.2090 cm^2. The cell solution consists of $CoCp_2$ (10 mM), $CoCp_2PF_6$ (10 mM), and $LiClO_4$ (0.7 M) in CH_3CN. The scan rate was 50 mV s^{-1}.

Figure 2.7

The *J–E* behavior of *n*-GaAs electrode in contact with CH_3CN-$Fc^{+/0}$ solution (a) before the electrode was used for electrochemical measurements in CH_3CN-$CoCp_2^{+/0}$ solution and (b) after performing *J–E* scans in CH_3CN-$CoCp_2^{+/0}$ solution in the dark and at five different light intensities from +0.2 V vs. $E(A/A^-)$ to –0.05V vs. V_{oc}. The CH_3CN-$Fc^{+/0}$ solution consists of Fc (90 mM), $FcBF_4$ (0.5 mM), and $LiClO_4$ (0.7 M) in CH_3CN, and $E(A/A^-)$ was +0.209 V vs. SCE. The CH_3CN-$CoCp_2^{+/0}$ solution consists of $CoCp_2$ (10 mM), $CoCp_2PF_6$ (10 mM), and $LiClO_4$ (0.7 M) in CH_3CN, and $E(A/A^-)$ was –0.888 V vs. SCE. The scan rate for both was 50 mV s^{-1}.

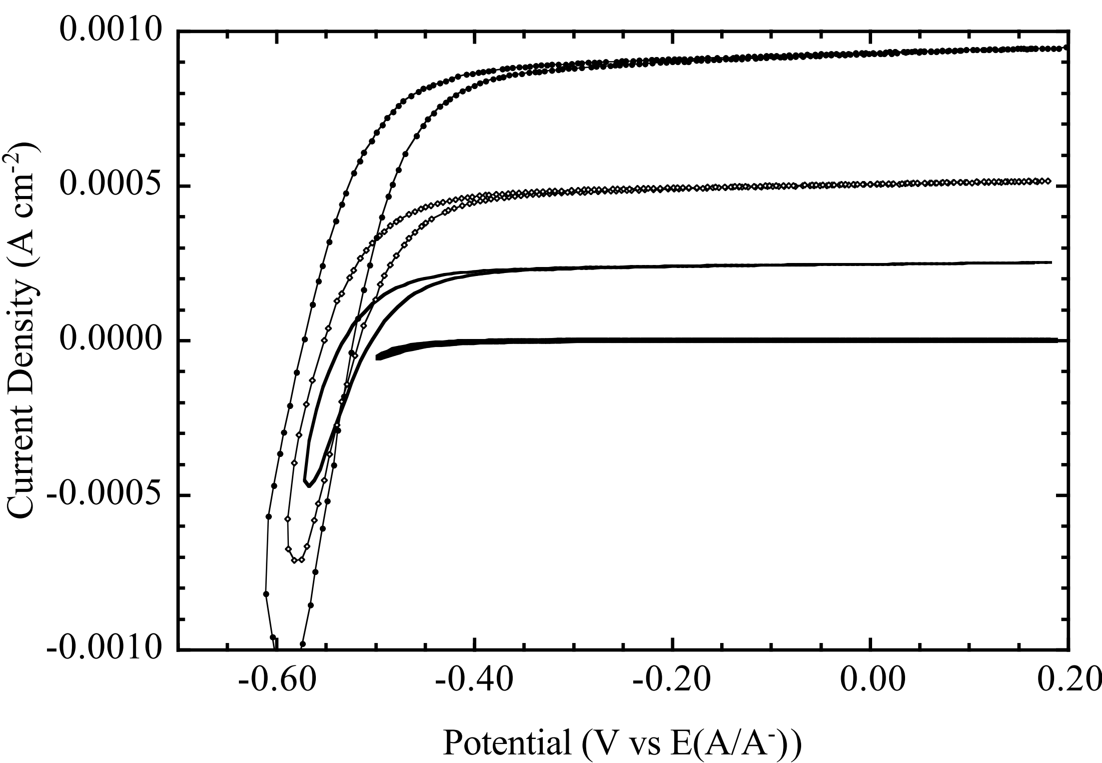

Figure 2.7a

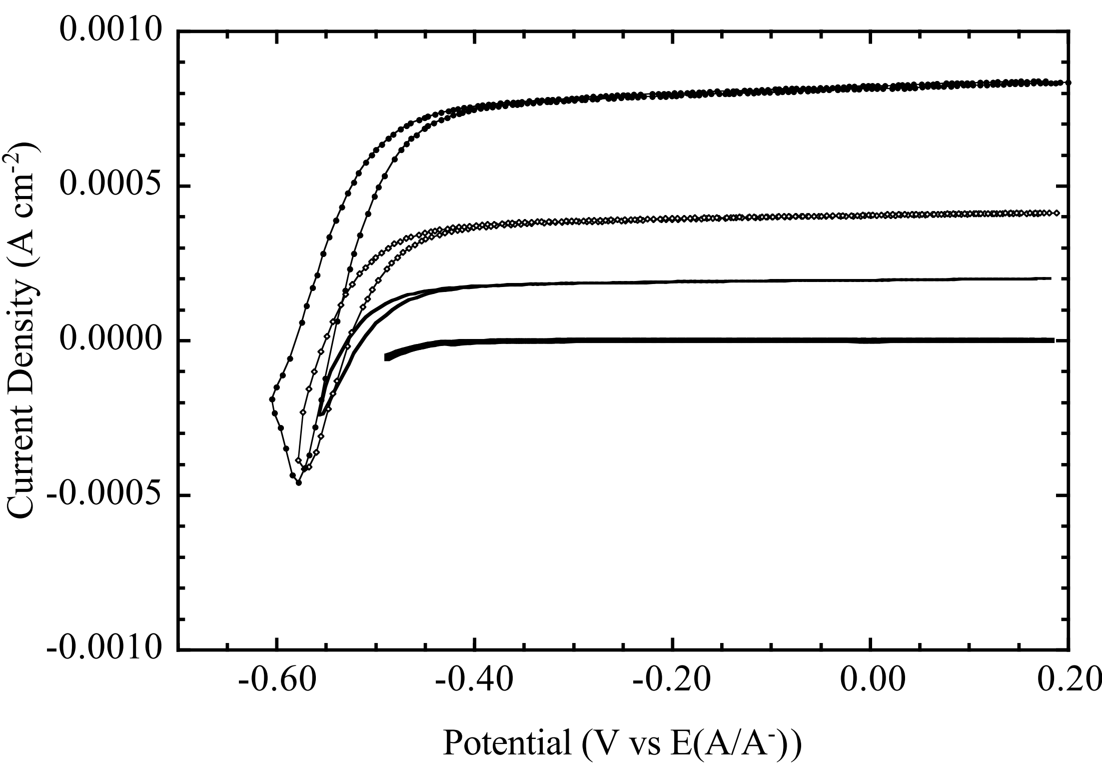

Figure 2.7b

4.3. X-Ray Photoelectron Spectroscopy and Cyclic Voltammetry Data of *n*-GaAs Surfaces in Contact with the CH_3CN-$CoCp_2^{+/0}$ Electrolyte

The anomalous open-circuit photovoltages observed when *n*-GaAs was immersed in CH_3CN-$CoCp_2^{+/0}$ solution signals the presence of a chemical reaction between the *n*-GaAs and the contacting solution under the conditions explored in this work. This hypothesis was confirmed by XPS studies of the surface of *n*-GaAs electrodes before and after being exposed to the CH_3CN-$CoCp_2^{+/0}$ electrolyte.

Figure 2.8 depicts the XPS survey spectrum for an *n*-GaAs surface before exposure to a CH_3CN-$CoCp_2^{+/0}$ solution (top spectrum). Inspection of the As 3p and Ga 3d regions in high resolution mode indicated that the As peak displayed negligible contribution from excess elemental As, as has been observed previously for *n*-GaAs surfaces exposed to the KOH and Br_2-CH_3OH sequential etching process.[44,54,55] The XP spectrum has been shown to remain unchanged after immersion or electrochemical operation of *n*-GaAs electrodes in the CH_3CN-$Fc^{+/0}$ electrolyte.[44,54,55] In contrast, the XPS data of an *n*-GaAs electrode recorded after 10 minutes of *J–E* scans in a CH_3CN-$CoCp_2^{+/0}$ solution (bottom spectrum in Figure 2.8) looks very different from that of a clean GaAs surface. Peaks for C and O were seen but Ga and most of As peaks disappeared, no peaks for Co were observed. However, it was found that simple immersion of the *n*-GaAs in all four electrolyte solutions without undergoing electrochemical measurement (as described in section 3.4.1) did not cause observable surface modification in the XPS study. Upon removal of the electrode after 10 minutes of immersion without potential scan, no film was observed on the surfaces.

The presence of changes in the GaAs surface chemistry at negative potentials in CH_3CN was also confirmed by investigating the cyclic voltammetry of *n*-GaAs in CH_3CN-0.7 M $LiClO_4$ solution, in the absence of redox-active species. As displayed in Figure 2.9, a reduction wave was observed at –1.5 V vs. SCE. Because the operating

limit of the solvent/electrolyte window is < –2.5 V vs. SCE, this reduction wave must be associated with chemical changes in the surface of the GaAs electrode. This observation is in excellent agreement with prior work by Kohl and Bard, who observed similar behavior for *n*-GaAs electrodes in contact with CH_3CN-0.1 M tetra-n-butylammonium perchlorate (TBAP) solution.[41]

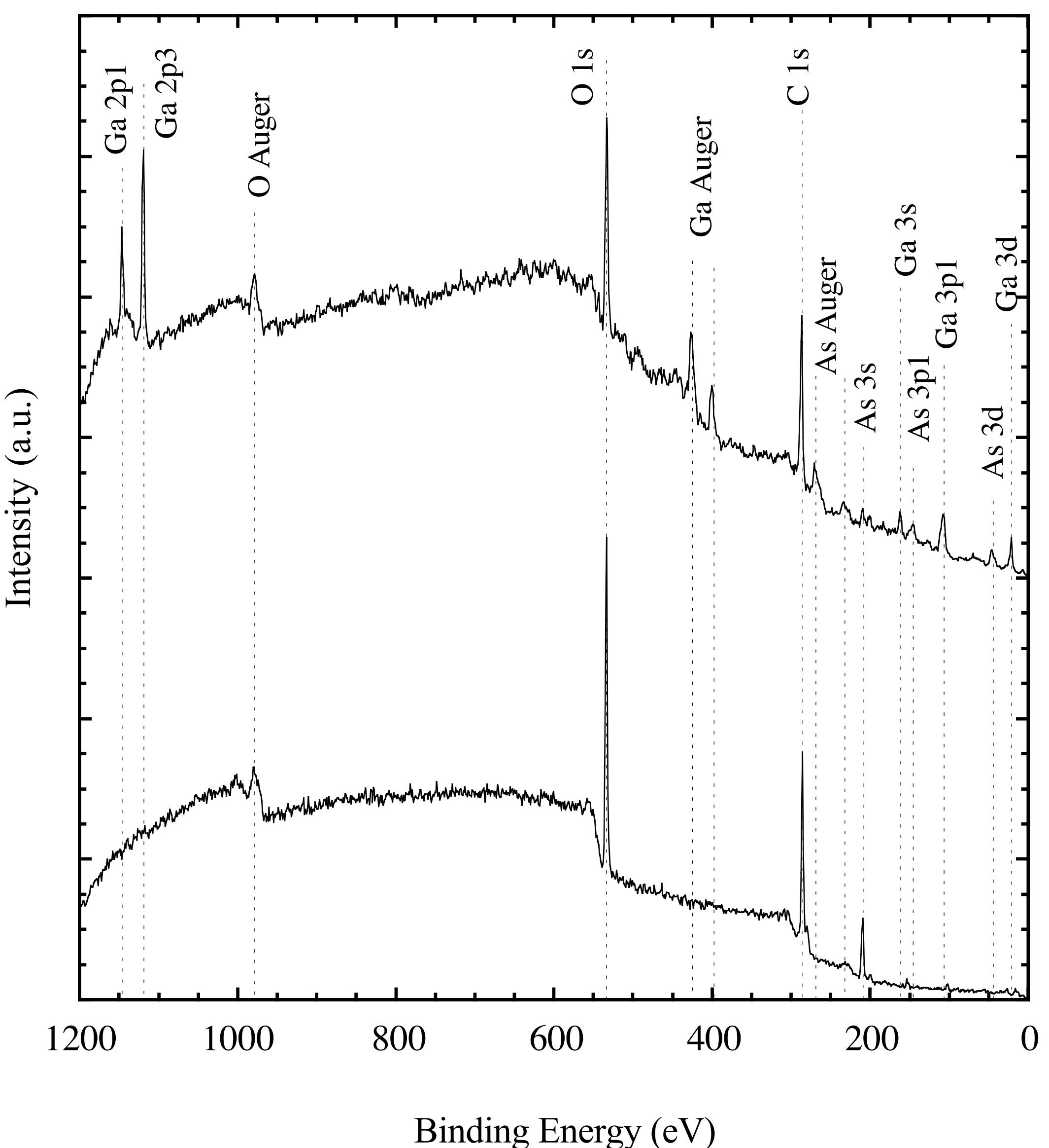

Figure 2.8

XP survey spectra of an *n*-GaAs electrode (a) immediately following etching process and (b) after 10 minutes of *J–E* scans in a CH_3CN solution containing $LiClO_4$ (0.7 M), $CoCp_2PF_6$ (10 mM), and $CoCp_2$ (10 mM).

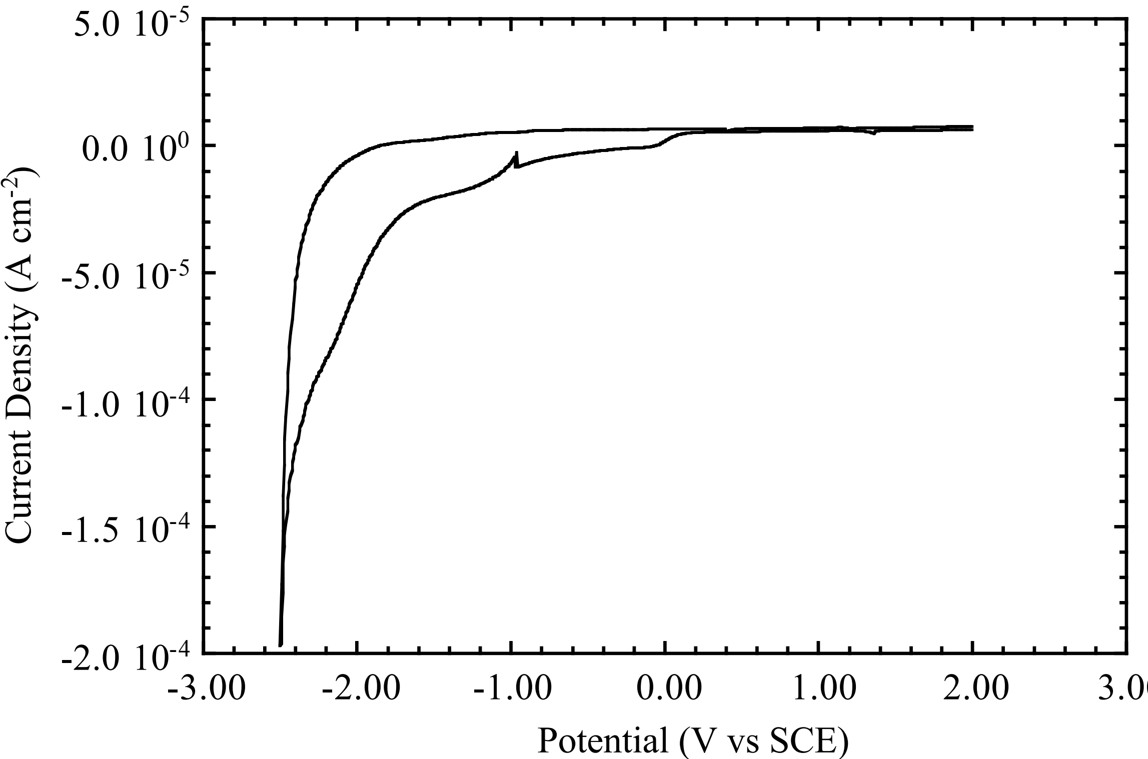

Figure 2.9

Cyclic voltammogram of *n*-GaAs in CH_3CN-0.7 M $LiClO_4$ in the absence of a redox species. A reduction wave at –1.5 V vs. SCE confirmed the presence of irreversible surface changes at negative potentials in CH_3CN. The scan rate was 50 mV s^{-1}.

5. Discussions

5.1. Electrochemical Properties of n-GaAs/CH_3CN Contacts

It is clear that *n*-GaAs electrodes exhibit partial Fermi-level pinning in contact with CH_3CN over a wide range of redox potentials. In prior work, the Fermi-level pinning behavior had been probed through the use of steady-state *J–E* and V_{oc} vs. T data.[33] The band edge shifts documented were often difficult to resolve when a small potential range is explored, but such behavior was clearly seen with a large variation in $E(A/A^-)$.

These conclusions are also consistent with differential capacitance measurements of the band edge positions of *n*-GaAs/CH_3CN contacts. Prior studies of the *n*-GaAs/CH_3CN-$Fc^{+/0}$ contact have yielded a barrier height of 1.1 V for this system,[9] in which the Nernstian solution potential, $E(A/A^-)$, was +0.32 V vs. SCE. For comparison, Mott-Schottky measurements of the *n*-GaAs/CH_3CN-$CoCp_2^{+/0}$ contact indicate a barrier height of 0.92 V, even though the redox potential of these solutions is –0.9 V vs. SCE. The fact that the barrier height changed by less than 300 mV for a change of more than 1.2 V in the redox potential of the solution clearly indicates the presence of Fermi-level pinning for these *n*-GaAs/CH_3CN contacts.

Similar conclusions regarding Fermi-level pinning of GaAs electrodes in contact with non-aqueous solvents have been reached previously from cyclic voltammetric and/or impedance studies of GaAs/CH_3CN contacts.[22,25,26,31,41,56] The cyclic voltammetric study described in this chapter has explored an even wider potential range than was investigated in the previous *J–E* experiments. Kohl and Bard reported the photoelectrochemical behavior of *n*-GaAs in CH_3CN solutions with a range of redox couples, including photovoltages for some redox couples having formal potentials negative of the GaAs flat-band potential.[41] The ability to generate a photovoltage at the

most negative cell potentials was attributed to the pinning of the Fermi level by surface states. The current-voltage properties of the *n*-GaAs/tetrahydrofuran system were characterized using cyclic voltammetry by DiQuarto and Bard.[56] Saturation of the photovoltage at cell potentials negative of the valence band for *n*-GaAs and positive of the conduction band for *p*-GaAs was interpreted as indicating Fermi-level pinning due to either a high density of surface states or carrier inversion at the interface. Yeh and Hackerman[31] investigated the behavior of the *n*-GaAs/N,N-dimethylformamide interface. Using cyclic voltammetry in solutions of various redox couples, they observed negative shifts in the oxidation/reduction wave of benzoquinone at n-GaAs under illumination as compared to the values of these peaks in the dark, and ascribed this behavior to non-ideality in the GaAs/liquid junction.

The Fermi-level pinning behavior observed herein is also consistent with a variety of prior studies of GaAs surface chemistry in other ambient. For example, non-ideal energetic behavior has been observed for *n*-GaAs surfaces exposed to a variety of impurities in UHV, with formation of As defects or excess elemental As thought to be the source of the persistent Fermi-level pinning of *n*-GaAs surfaces.[57-59] In addition, formation of metal contacts on *n*-GaAs is well documented to result in Fermi-level pinning.[53,60,61] In fact, we are not aware of any series of *n*-GaAs contacts reported to date in which Fermi-level pinning has not been observed when the electrochemical potential of the contacting phase has been varied over a significant range.

5.2. Interfacial Rate Constant Determinations Using n-GaAs/CH_3CN Contacts

The XPS analysis of the GaAs system shows the formation of a carbonaceous overlayer on the GaAs surface subsequent to electrochemical measurements in the CH_3CN-$CoCp_2^{+/0}$ solution. The evidence for this irreversible surface changes implies that a significant portion of the interfacial current in the *n*-GaAs/CH_3CN-$CoCp_2^{+/0}$ contact

flows through pathways that do not involve the direct transfer of electrons from the conduction band of the semiconductor into dissolved, nonadsorbed redox acceptor species. The XPS data clearly indicate that a chemical reaction, which produces a carbonaceous surface film, dominates the interfacial chemistry of the *n*-GaAs/CH_3CN-$CoCp_2^{+/0}$ contact at potentials sufficiently negative to produce cathodic current flow through the interfaces. This film might introduce surface states and thereby raise the overall flux, act as an insulator and block the interfacial current from flowing, or both. The presence of such a film also implies that the concentration of adsorbed electroactive $CoCp_2^{+/0}$-based sites can not be directly deduced under these experimental conditions from mass-change measurements of the electrode.

The *n*-GaAs electrodes investigated in this chapter and prior work exhibited higher open-circuit voltages, and therefore must have lower values of k_{et} than have been reported for *n*-GaAs electrodes exposed to less optimal etching procedures.[7] Since the rate constant k_{et} describes the direct transfer of electrons from the conduction band of the semiconductor to nonadsorbing electron acceptor ions in the solution phase, k_{et} can not depend on the surface condition or etching procedure. The photovoltage value observed at J_{ph} = 1 mA cm^{-2} can therefore be used to set an upper bound on k_{et} for the *n*-GaAs/CH_3CN-$CoCp_2^{+/0}$ system, because the rate of the direct electron-transfer process is equal to, or less than, the observed interfacial charge transfer flux. This produces an upper bound on k_{et} for the *n*-GaAs/CH_3CN-$CoCp_2^{+/0}$ contact of less than 10^{-14} cm^4 s^{-1}, which is consistent with theoretical expectations for such process.[4,6,11] It is, of course, always possible to produce less rectifying contacts through introduction of etch-induced surface defects or surface nonstoichiometries. However, regardless of the surface condition, etch-related increases in current density at a given electrode potential are a clear indication that the direct electron-transfer process is not being measured from the interfacial current densities observed at such contacts.

Additional evidence supporting the presence of surface-states at the *n*-GaAs/CH_3CN-$CoCp_2^{+/0}$ contact can be obtained by comparison of the *J–E* properties of the *n*-GaAs/CH_3CN-$CoCp_2^{+/0}$ contact with those of the *n*-GaAs/CH_3CN-$Fc^{+/0}$ contact. The results had shown that the surface-state recombination is the dominant recombination mechanism for the *n*-GaAs/CH_3CN-$Fc^{+/0}$ semiconductor/liquid contact, and thermionic emission is greatly suppressed in this system.[33] Thus the value of k_{et} must be smaller than 10^{-14} cm^4 s^{-1} for the *n*-GaAs/CH_3CN-$Fc^{+/0}$ contact in order to have the observed flux dominate the recombination current of the contact.[9] Because the barrier heights are so similar between the *n*-GaAs/CH_3CN-$CoCp_2^{+/0}$ and *n*-GaAs/CH_3CN-$Fc^{+/0}$ contacts, and the Marcus nuclear reorganization energy term is only weakly dependent on the driving force for the expected reorganization energy of between 0.5 and 1.0 eV for these metallocenes at semiconductor electrodes having this value of the barrier height,[4,11,62,63] the charge-transfer rate constants should certainly not differ by more than a factor of 10^2. This comparison therefore also supports the notion that surface states, and not direct interfacial electron transfer, dominate the interfacial kinetics of the *n*-GaAs/CH_3CN-$CoCp_2^{+/0}$ contact. The discovery of chemical methods to remove this Fermi-level pinning condition, and subsequent demonstration of an ideal energetic barrier height vs. $E(A/A^-)$ dependence as well as the expected second-order kinetic rate law, are therefore required before robust k_{et} values can be extracted from the steady-state *J–E* behavior of n-GaAs/CH_3CN contacts.

6. Summary

The barrier height of *n*-GaAs/CH_3CN-$CoCp_2^{+/0}$ interface has been measured, and combined with prior barrier height result for *n*-GaAs/CH_3CN-$Fc^{+/0}$ interface,[9] the presence of partial Fermi-level pinning was confirmed. The presence of irreversible chemical and/or electrochemical changes on *n*-GaAs electrodes immersed in CH_3CN-$CoCp_2^{+/0}$ solutions was investigated using x-ray photoelectron spectroscopy (XPS), steady-state current density–potential (*J*–*E*) measurements, and cyclic voltammetric studies that were designed to probe surface reactions. Since the dominant recombination mechanism of *n*-GaAs/CH_3CN interfaces is surface-state recombination and not direct electron transfer, the k_{et} value could not be evaluated from the steady-state *J*–*E* data of *n*-GaAs/CH_3CN-$CoCp_2^{+/0}$ junction. The similarity in barrier heights of *n*-GaAs/CH_3CN-$CoCp_2^{+/0}$ and *n*-GaAs/CH_3CN-$Fc^{+/0}$ junctions indicated that the charge-transfer rate constants should not differ by more than a factor of 10^2. Only when an ideal energetic barrier height vs. $E(A/A^-)$ dependence and the second-order rate law can be established, a robust k_{et} values can then be extracted from this system.

7. Acknowledgments

This work was supported by the U.S. Department of Energy (Office of Basic Energy Sciences) and the Eastman Kodak Company.

8. References and Notes

(1) Diol, S. J.; Poles, E.; Rosenwaks, Y.; Miller, R. J. D. *J. Phys. Chem. B* **1998**, *102*, 6193.

(2) Fan, F. R.; Bard, A. J. *J. Phys. Chem.* **1991**, *95*, 1969.

(3) Kesselman, J.; Hoffman, M. R.; Shreve, G. A.; Lewis, N. S. *J. Phys. Chem.* **1995**, *98*, 13385.

(4) Lewis, N. S. *Ann. Rev. Phys. Chem.* **1991**, *42*, 543.

(5) Lewis, N. S. *Sol. Energy Mater. Sol. Cells* **1995**, *38*, 323.

(6) Lewis, N. S. *J. Phys. Chem. B* **1998**, *102*, 4843.

(7) Meier, A.; Kocha, S. S.; Hanna, M. C.; Nozik, A. J.; Siemoneit, K.; Reineke-Koch, R.; Memming, R. *J. Phys. Chem. B* **1997**, *101*, 7038.

(8) Meier, A.; Selmarten, D. C.; Siemoneit, K.; Smith, B. B.; Nozik, A. J. *J. Phys. Chem. B* **1999**, *103*, 2122.

(9) Pomykal, K. E.; Fajardo, A. M.; Lewis, N. S. *J. Phys. Chem.* **1996**, *100*, 3652.

(10) Pomykal, K. E.; Lewis, N. S. *J. Phys. Chem. B* **1997**, *101*, 2476.

(11) Royea, W. J.; Fajardo, A. M.; Lewis, N. S. *J. Phys. Chem. B* **1998**, *102*, 3653.

(12) Sinn, C.; Meisser, D.; Memming, R. *J. Electrochem. Soc.* **1990**, *137*, 168.

(13) Wang, D.; Buontempo, J.; Li, Z. W.; Miller, R. J. D. *Chem. Phys. Lett.* **1995**, *232*, 7.

(14) Fajardo, A. M.; Lewis, N. S. *Spectrum* **1997**, *10*, 1.

(15) Fajardo, A. M.; Lewis, N. S. *Science* **1996**, *274*, 969.

(16) Fajardo, A. M.; Lewis, N. S. *J. Phys. Chem. B* **1997**, *101*, 11136.

(17) Horrocks, B. R.; Mirkin, M. V.; Bard, A. J. *J. Phys. Chem.* **1994**, *98*, 9106.

(18) Rosenwaks, Y.; Thacker, B. R.; Ahrenkiel, R. K.; Nozik, A. J. *J. Phys. Chem.* **1992**, *96*, 10096.

(19) Rosenwaks, Y.; Thacker, B. R.; Nozik, A. J.; Ellingson, R. J.; Burr, K. C.; Tang, C. L. *J. Phys. Chem.* **1994**, *98*, 2739.

(20) Smith, B. B.; Halley, J. W.; Nozik, A. J. *Chem. Phys.* **1996**, *205*, 245.

(21) Bard, A. J.; Bocarsly, A. B.; Fan, F. R. F.; Walton, E. G.; Wrighton, M. S. *J. Am. Chem. Soc.* **1980**, *102*, 3671.

(22) Nagasubramanian, G.; Wheeler, B. L.; Bard, A. J. *J. Electrochem. Soc.* **1983**, *130*, 1680.

(23) Singh, P.; Rajeshwar, K. *J. Electrochem. Soc.* **1981**, *128*, 1724.

(24) Singh, P.; Rajeshwar, K.; DuBow, J.; Job, R. *J. Am. Chem. Soc.* **1980**, *102*, 4676.

(25) Ba, B.; Fotouhi, B.; Gabouze, N.; Gorochov, O.; Cachet, H. *J. Electroanal. Chem.* **1992**, *334*, 263.

(26) Gabouze, N.; Fotouhi, B.; Gorochov, O.; Cachet, H.; Yao, N. A. *J. Electroanal. Chem.* **1987**, *237*, 289.

(27) Salvador, P.; Diez, Y. G.; Soto, L. G. *Surf. Sci.* **1991**, *245*, 324.

(28) Uosaki, K.; Shigematsu, Y.; Kaneko, S.; Kita, H. *J. Phys. Chem.* **1989**, *93*, 6521.

(29) DiQuarto, F.; Bard, A. J. *J. Electroanal. Chem.* **1981**, *127*, 43.

(30) Langmuir, M. E.; Hoenig, P.; Rauh, R. D. *J. Electrochem. Soc.* **1981**, *128*, 2357.

(31) Yeh, L.-S. R.; Hackerman, N. *J. Phys. Chem.* **1978**, *82*, 2719.

(32) Tufts, B. J.; Casagrande, L. G.; Lewis, N. S.; Grunthaner, F. J. *Appl. Phys. Lett.* **1990**, *57*, 2262.

(33) Casagrande, L. G.; Lewis, N. S. *J. Am. Chem. Soc.* **1985**, *107*, 5793.

(34) Morrison, S. R. *Electrochemistry at Semiconductor and Oxidized Metal Electrodes*; Plenum: New York, 1980.

(35) Casagrande, L. G. Ph.D., Stanford University, 1988.

(36) Howard, J. N.; Koval, C. A. *Anal. Chem.* **1994**, *66*, 4525.

(37) Gerischer, H. *J. Phys. Chem.* **1991**, *95*, 1356.

(38) Evenor, M.; Huppert, D.; Gottesfeld, S. *J. Electrochem. Soc.* **1986**, *133*, 296.

(39) Chazalviel, J.-N. *J. Electrochem. Soc.* **1982**, *129*, 963.

(40) Kohl, P. A.; Bard, A. J. *J. Electrochem. Soc.* **1979**, *126*, 603.

(41) Kohl, P. A.; Bard, A. J. *J. Electrochem. Soc.* **1979**, *126*, 59.

(42) Lin, M. S.; Hung, N.; Wrighton, M. S. *J. Electroanal. Chem.* **1983**, *149*, 27.

(43) Casagrande, L. G. Ph.D. Thesis, Stanford University, 1988.

(44) Bansal, A.; Tan, M. X.; Tufts, B. J.; Lewis, N. S. *J. Phys. Chem.* **1993**, *97*, 7309.

(45) Casagrande, L. G.; Tufts, B. J.; Lewis, N. S. *J. Phys. Chem.* **1991**, *95*, 1373.

(46) Stocker, H. J.; Aspnes, D. E. *Appl. Phys. Lett.* **1983**, *42*, 85.

(47) Vasquez, R. P.; Lewis, B. F.; Frunthaner, F. J. *J. Vac. Sci. Technol.* **1983**, *B1*, 791.

(48) Hendrickson, D. H.; Sohn, Y. S.; Gray, H. B. *Inorg. Chem.* **1971**, *10*, 1559.

(49) Sheats, J. E.; Rausch, M. D. *J. Org. Chem.* **1970**, *35*, 3245.

(50) CAUTION: Lithium perchlorate reacts explosively with organics at these temperatures. Great care must be taken to ensure that no organic material is exposed to the molten salt. Lithium perchlorate also decomposes at temperatures above 400 ˚C, therefore the molten salt temperature must be kept below this value.

(51) Bard, A. J.; Faulkner, L. R. *Electrochemical Methods: Fundamentals and Applications*; John Wiley & Sons: New York, 1980.

(52) Tan, M. X.; Laibinis, P. E.; Nguyen, S. T.; Kesselman, J. M.; Stanton, C. E.; Lewis, N. S. *Prog. Inorg. Chem.* **1994**, *41*, 21.

(53) Sze, S. M. *The Physics of Semiconductor Devices*; 2nd ed.; Wiley: New York, 1981.

(54) Lunt, S. R.; Casagrande, L. G.; Tufts, B. J.; Lewis, N. S. *J. Phys. Chem.* **1988**, *92*, 5766.

(55) Tufts, B. J.; Abrahams, I. L.; Caley, C. E.; Lunt, S. R.; Miskelly, G. M.; Sailor, M. J.; Santangelo, P. G.; Lewis, N. S.; Roe, A. L.; Hodgson, K. O. *J. Am. Chem. Soc.* **1990**, *112*, 5123.

(56) DiQuarto, F.; Bard, A. J. *J. Electroanal. Chem.* **1981**, *127*, 43.

(57) Spindt, C. J.; Liu, D.; Miyano, K.; Meissner, P. L.; Chiang, T. T.; Kendelewicz, T.; Lindau, I.; Spicer, W. E. *Appl. Phys. Lett.* **1989**, *55*, 861.

(58) Spicer, W. E.; Chye, P. W.; Skeath, P. R.; Su, C. Y.; Lindau, I. *J. Vac. Sci. Technol.* **1979**, *16*, 1422.

(59) Spicer, W. E.; Lindau, I.; Skeath, P.; Su, C. Y. *J. Vac. Sci. Technol.* **1980**, *17*, 1019.

(60) Mead, C. A.; Spitzer, W. G. *Phys. Rev.* **1964**, *134*, A713.

(61) McGill, T. C. *J. Vac. Sci. Technol.* **1974**, *11*, 935.

(62) Uhlendorf, I.; Reineke-Koch, R.; Memming, R. *J. Phys. Chem.* **1996**, *100*, 4930.

(63) Fonash, S. J. *Solar Cell Device Physics*; Academic: New York, 1981.

Chapter 3

Fabrication and Characterization of *n*-Si(111) Based Metal-Insulator-Semiconductor Diodes

1. Introduction

Our knowledge of metal-semiconductor diodes goes back more than a century ago when Braun,[1] in 1874, discovered the rectifying nature of metallic contacts on semiconductors such as copper, iron, and lead sulfide crystals.[2] It was not until 1931, when Schottky[3] proposed the existence of some sort of potential barrier at the metal-semiconductor contact, that the scientists began to understand the rectifying nature of this junction. In 1938, Schottky[4] and Mott[5] pointed out, independently, that the potential barrier formation was the result of a difference between the work functions of the metal and semiconductor, and the metal-semiconductor barrier height (ϕ_b) could be calculated according to this equation:

$$\phi_b = (\varphi_m - \chi_s)/q \tag{3.1}$$

where φ_m is the metal work function and χ_s is the electron affinity of the semiconductor. This behavior has come to be known as the "Schottky limit."

Practical metal-semiconductor contacts do not always appear to obey the Schottky limit. Linear dependence of the barrier height on metal work function is predominantly observed in ionic semiconductors only. In the case of covalent semiconductors, some have barrier heights that are only weakly dependent on φ_m, and some exhibit almost no relationship between ϕ_b and φ_m.[6] Bardeen[7] was the first to point out the importance of localized surface states, which exist in many covalent semiconductors, in determining the barrier height. These surface states arise from the dangling bonds at the semiconductor surface where no neighboring atoms are available for making covalent bond on the vacuum side, and their energies are usually continuously distributed across the bandgap. When brought into contact with a metal, equilibration between Fermi levels of these two phases occurs first by exchanging charges between the metal and the surface states,

which then reduces or eliminates the effect on the semiconductor depletion region.[2] As a result the barrier height is primarily determined by the surface states and is largely independent of the metal in contact. A system that obeys this "Bardeen limit" is described as "Fermi-level pinned."

Heine[8] argued that when a metal is deposited on a semiconductor surface, it is possible for the wave function of electrons in the metal with energies corresponding to the forbidden gap in the semiconductor to extend into the semiconductor and thereby induce states within the bandgap. These metal induced gap states (MIGS) replace the intrinsic electron states that may be present on the semiconductor surface, and can affect the true barrier height measurements.

In some cases, when a metal is deposited on a semiconductor surface, an interfacial reaction between the metal and the semiconductor occurs to form deleterious silicide. This interfacial reaction causes the interface to move into the semiconductor bulk, and as a result the barrier height is independent of the surface properties and the metal work function.[9-11,12,13] It was found that the barrier heights of this type of MS contacts are linearly dependent on the heat of formation of the silicide.[14] In these cases the properties of the silicides controls barrier formation, which prevents the true barrier height of the MS contacts to be determined.

A thin-film insulator, namely thermally grown oxide, has been used to make metal-insulator-semiconductor (MIS) contacts since the mid-60's. A native thin oxide layer on the semiconductor surface is thin enough that a significant number of electrons can tunnel through it, and it also satisfies the dangling bonds and thus reduces the intrinsic surface state density. However, thermally grown oxides on silicon typically contain fixed positive charges, which increase the barrier height of *p*-type Si junctions, but have an opposite effect on *n*-type Si junctions.[15] Some metals can also penetrate through a thin layer of oxide, and react with the semiconductor to form silicide. Although it's now possible to control oxide layer thicknesses on the order of angstroms,

oxide layers tend to grow thicker over time and consequently lower the current that was allowed to tunnel through.

An alkyl monolayer can serve as a useful alternative to the oxide layer in MIS devices, because its thickness is easily controlled down at an atomic level. Since such layers can be covalently attached to the Si surface, they also satisfy the dangling bonds and reduce the density of surface states. Since the interactions between the independent alkyl chains and the Si atoms are covalent, they can align themselves in registry with the Si atoms better than the lattice-constrained oxygen atoms in SiO_2. Many alkyl groups have been covalently attached to Si(111) surfaces via a two-step chlorination/alkylation procedure.[16-18] This modification technique could be utilized to develop a MIS system enabling barrier height measurements of intimate metal-semiconductor contacts not currently possible. For an improved MIS system with an alkyl insulating layer, the observed ϕ_b value should be closer to the Schottky limit. Another advantage of using an alkyl insulator is that the thickness is easily controlled by using different chain lengths, and thus reproducible thicknesses can be achieved for systematic investigation of its effects on the junction electrical properties. Barrier height measurements and *J–E* characterization of the MIS with different insulator thickness could identify an optimal alkyl chain that can effectively inhibit silicide formation while introducing the minimal series resistance.

Introduction of a thin insulating layer between a metal and a semiconductor could affect the *J–E* characteristics of an MS contact in many ways. An insulating layer could reduce the number of majority carriers crossing the interface from the semiconductor into the metal, decrease the reverse saturation current density (J_0) , and therefore increase the open-circuit voltage (V_{oc}). It could also act as a chemical barrier and prevent unfavorable interfacial reactions between the metal and the semiconductor. As depicted in Figure 3.1, voltage drop typically occurs at a MIS interface due to the resistance of the insulator. However, when the insulating layer is very thin (i.e., < 20 Å), the potential drop across it

should be negligibly small compared to that in the semiconductor depletion region,[2] and electrons should be able to tunnel through this layer relatively easily. Straight alkyl chains tend to line up on a surface and form an organized overlayer, which will also encourage electron tunneling. In this case, the barrier height and the contact potential difference should be unaffected by the presence of the thin interfacial layer, and the true MS barrier height can be extracted for silicide-forming metal/Si interfaces.

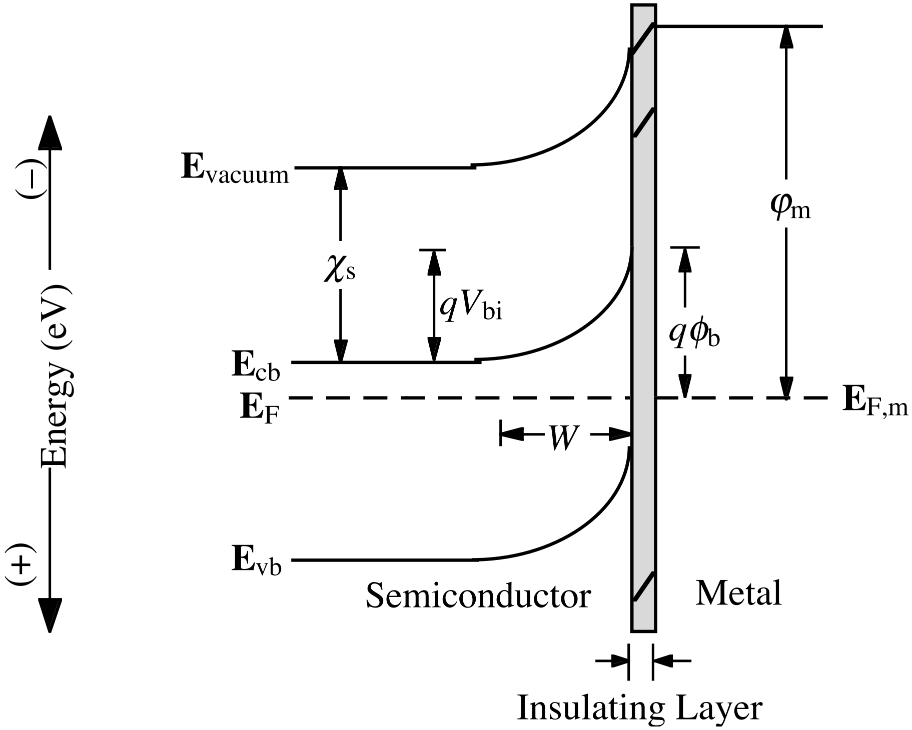

Figure 3.1

A band bending diagram of a metal-insulator-semiconductor (MIS) junction. The barrier height (ϕ_b) of this junction is less than the difference between the metal work function (φ_m) and the electron affinity of the semiconductor (χ_s), and it is caused by a voltage drop across the insulating layer. If the insulating layer is thin enough, the voltage drop can become negligible, and can mimic the electrical properties of the equivalent metal/semiconductor junction.

2. Experimental

2.1. Solvents and Reagents

All solvents used for surface modification, including anhydrous methanol, anhydrous chlorobenzene, anhydrous acetonitrile, and anhydrous tetrahydrofuran (THF) were obtained from Aldrich and were used as received. These solvents were packaged under N_2(g) in Sure/Seal bottles and were stored over activated 3 Å molecular sieves (EM Science) in a N_2(g)-purged glove box. Solvents used for wafer degreasing, acetone, dichloromethane, methanol, and 1,1,1-trichloroethane, were either reagent grade (GR) or Omnisolve grade obtained from EM Science and used as received. The 30% H_2O_2 was purchased from EM Science, and the H_2SO_4(aq) was obtained from J. T. Baker. Hydrofluoric acid buffered with ammonium fluoride (NH_4F/HF, buffered HF) and 40% ammonium fluoride (NH_4F) solutions were purchased from Transene Co. The 18 MΩ·cm resistivity H_2O was collected from a Barnstead E-pure filtration system. The following chemicals used for surface modification were purchased from Aldrich and were used without further purification: Phosphorus pentachloride (PCl_5), benzoyl peroxide, methylmagnesium bromide (CH_3MgBr, 3.0 M in diethyl ether), methylmagnesium chloride (CH_3MgCl, 3.0 M in THF), ethylmagnesium bromide (C_2H_5MgBr, 3.0 M in diethyl ether), propylmagnesium chloride (C_3H_7MgCl, 2.0 M in diethyl ether), butylmagnesium chloride (C_4H_9MgCl, 2.0 M in THF), hexylmagnesium bromide ($C_6H_{13}MgBr$, 2.0 M in diethyl ether), octylmagnesium chloride ($C_8H_{17}MgCl$, 2.0 M in THF), and decylmagnesium bromide ($C_{10}H_{21}MgBr$, 1.0 M in diethyl ether).

2.2. Semiconductor Material and Etching

Single-crystal, (111)-oriented *n*-type silicon wafers with a polished front side were obtained from Crysteco. The wafers were phosphorous-doped with a resistivity of 2–8.5 Ω·cm and a thickness of 475–550 μm as specified by the manufacturer. The silicon wafers were first oxidized in a "Pirhana" solution which consisted of 3:1 (v/v) concentrated H_2SO_4(aq):H_2O_2 (30%) heated to approximately 100 °C for one hour.[18] **Caution:** *The acidic "Pirhana" solution is extremely dangerous, particularly in contact with organic materials and should be handled carefully*. The wafers were then rinsed with copious amount of 18.0 MΩ·cm resistivity water (obtained from a Barnstead Inc. Nanopure water purification system), dried under pressurized N_2(g), and stored for future use. Ohmic contact was made by rubbing an Ga-wetted In ball on the non-polished side of both derivatized and H-terminated samples. This was done by first rubbing an In (99.999%, Alfa Aesar) ball into a small amount of melted Ga (99.99+%, Aldrich) to create a eutectic mixture. An In ball, held by a tweezer, was then dipped into and wetted by the eutectic mixture, and was used to rub on the back side of the Si samples.

Before surface modifications, the wafer was cut into smaller size samples. Each piece was briefly sonicated in 18.0 MΩ·cm resistivity water, degreased by rinsing sequentially with methanol, acetone, 1,1,1-trichloroethane, dichloromethane, 1,1,1-trichloroethane, acetone, and methanol, and followed by another brief sonication in water. After blow drying with N_2(g), the samples were etched in NH_4F/HF (buffered HF) for 30–45 seconds, and then without rinsing immersed in 40% NH_4F for 10–15 min.[19] Tiny bubbles were observe to appear on the (111) surface of the samples when immersed in 40% NH_4F. Following the etching process, the samples were rinsed with 18.0 MΩ·cm resistivity water (obtained from Barnstead E-pure filtration system), and dried under a stream of N_2(g). The samples were quickly mounted onto the XPS stubs and introduced

into ultrahigh vacuum (UHV) system that houses the x-ray photoelectron spectroscopy (XPS) via an atmospheric load lock for immediate surface characterization.

2.3. Surface Modification

All surface modification procedures were carried out in a N_2(g)-purged glove box which is connected to the UHV system housing the XPS spectrometer via a gate valve. After verifying the surfaces were H-terminated, the samples were transferred into glove box without exposing to the air. The stock chlorinating solution was prepared by dissolving excess PCl_5 in chlorobenzene to form a saturated solution (typically 0.6–0.7 M). The solution was warmed to about 60 °C for at least 1 hour to ensure that enough PCl_5 had dissolved. Immediately before use, a small portion of the stock chlorinating solution was poured into a small beaker, and a few grains of benzoyl peroxide were added (approximately 30–40 mg of benzoyl peroxide in 10 ml of PCl_5-chlorobenzene solution) as a radical initiator.[20,21] With the samples completely immersed in this solution and the beaker covered by a watch glass, the reaction was heated to 90–100 °C for 45–50 min. The samples were then taken out of the chlorinating solution, rinsed with anhydrous THF followed by anhydrous methanol, and dried in a stream of N_2(g). The chlorinated samples were mounted on the stub and transferred into UHV for characterization.

Following the XPS characterization, the chlorinated samples were transferred back into the glove box and further derivatized by alkylation. The samples were immersed in alkyl Grignard (RMgX: R = CH_3, C_2H_5, C_3H_7, C_4H_9, C_6H_{13}, C_8H_{17}, or $C_{10}H_{21}$; X = Br or Cl) solutions and heated to 65–80 °C. The duration of this step was varied with the alkyl chain length, and is summarized in Table 3.1.[22] The alkylated samples were rinsed thoroughly with anhydrous THF followed by anhydrous methanol, individually immersed in anhydrous methanol in screw-capped vials, and taken out of the glove box for sonication. The derivatized samples were sonicated in anhydrous methanol

and anhydrous acetonitrile for 5 min each, dried in a stream of N_2(g) before being mounted on the XPS stub, and introduced into UHV through atmospheric load lock for surface characterization.

Table 3.1

A summary of reaction time, overlayer thickness, and air stability of alkyl-terminated Si.

Alkyl Group	Reaction Time (hr)	Observed Ellipsometric Thickness[a] (Å)	Air Stability[a,b] (hr)
CH_3	2.5 – 8	--	--
C_2H_5	2.5 – 10	7 ± 2	20
C_3H_7	10 – 18	--	--
C_4H_9	12 – 24	9 ± 1	> 87
C_6H_{13}	16 – 46	11 ± 1	> 87
C_8H_{17}	20 – 46	--	--
$C_{10}H_{21}$	20 – 72	12 ± 2	30

[a] The data were taken from prior studies performed in our laboratory.

[b] The numbers represent the amount of time for alkyl-terminated surfaces to oxidize in air to an extent that a half monolayer of oxide could be detected by the XPS.

2.4. Metal Deposition and Device Fabrications

2.4.1. The First-Generation MIS Device

Electrodes were fabricated by attaching a tinned copper wire (22 AWG, Belden) to the ohmic contact of unmodified Si using electrically conductive silver print (GC Electronics). As illustrated in Figure 3.2, the wire was encased in glass tubing and the backside and edges of the electrode were sealed with insulating white epoxy (Epoxy Patch Kit 1C, Dexter Corp.), leaving only the polished surface of the crystal exposed. Another thin tinned copper wire was wrapped around the epoxy seal in a close proximity to the Si and the outside of the glass tubing before the epoxy was completely hardened. The electrodes were stored in a covered tray for at least 24 hours for the epoxy to cure. A layer of Ni was then deposited on the front side of electrode, covering the Si and the epoxy surrounding it, along with the thin tinned copper wire that was situated near the Si. The front contact was provided by the deposited metal film that electrically connects the Si surface and the tinned copper wire. A small amount of silver print was painted around the wire and epoxy to ensure a good electrical connection. Electrode areas were determined by digitally scanning the electrodes along with a micro ruler, and the exposed electrode areas were traced and measured using the digitizing software ImageSXM. The typical exposed electrode areas were 0.05–0.15 cm^2.

All electrodes made of modified Si were transferred to a high-vacuum evaporation chamber (Vacuum Coating Unit LCI-14B, Consolidated Vacuum Corp.) and evacuated to a pressure of $\leq 5 \times 10^{-6}$ Torr. The Ni (99.994%, Alfa AESAR) was deposited onto the electrodes at a rate of 2–5 Å/s to a thickness of ~450 Å by filament evaporation. Evaporation rates and film thicknesses were determined by a R. D. Mathis TM-100 thickness monitor.

2.4.2. The Second-generation MIS Device

The Si wafers were cut into 5 mm × 5 mm pieces and were modified and characterized as described. Immediately following the surface derivatization process, the modified samples were introduced into the evaporator for metal deposition. The thickness of the deposited metal film was usually 450 Å. Figure 3.3 depicts the cell assembly of this sandwiched MIS device. Each device could hold two samples at the same time. Two small Cu plates embedded on the bottom portion of the device provided the back contacts. The ohmic contacted backside of a sample was bonded to the Cu plate using silver print. Two thick Cu wires were inserted into the top portion of the device made of delrin at an angle so that the ends appeared on the surface of the underside near the two circular openings. The wire ends were cut and polished to the level of the delrin top plate surface and referred to as Cu dots. When the cell was assembled, the Cu dots should touch the samples and make electrical contacts with the deposited metal film. The other ends of these two wires were connected to instruments via alligator clips as front contacts. The device had two openings for illumination, and a cell holder was used to position the device so the incident light could hit the surfaces of samples without creating any shadow. Two screws were necessary to hold together the cell device.

2.4.3. The Third-generation MIS Device

The front contact of the second-generation device was replaced with an indium tin oxide (ITO)-coated glass obtained from Delta Technology. To avoid short-circuiting, the ITO-coating was pre-patterned so that the area and the shape of conductive coating match that of the deposited metal on the Si surface. The design for patterning mask was created in ClarisDraw version 1.0.4 and was printed out and photographed onto a Kodak mask plate. At least 30 min prior to the patterning, ITO-coated slides were cleaned in acetone and 18 MΩ·cm H_2O, dried in a stream of $N_2(g)$, and baked in a 100˚C oven for 30 min.

This step served to degrease the slide surface and to eliminate moisture, both could affect the adhesion of photoresist.

Shipley 1818 photoresist was spin-coated (~30 s) onto the ITO-coated side (cut into 2.5 mm × 2.5 mm pieces), pre-baked in a 90˚C oven for 20 min, and then exposed to UV radiation under the patterning mask for 60 s. After immersing the slides in Shipley CD-30 developer, the UV-exposed part of photoresist was washed off in deionized water. The slides were blow-dried with N_2(g) and post-baked at 90˚C for 15 min. Once the photoresist pattern was baked onto the ITO coating, the uncovered portion was etched away in an aqueous solution of 20% HCl (EM Science) and 5% HNO_3 (EM Science) at 55˚C for 5–7 min. The ITO-coated slides were rinsed with 18 MΩ·cm H_2O, and then immersed in a basic solution or 10% Na_2CO_3 to neutralize the acid etch. The slides were again rinsed with 18 MΩ·cm H_2O and dried under N_2(g). The remaining photoresist was washed off with acetone, followed by another 18 MΩ·cm H_2O rinse and N_2(g) dried. The ITO pattern could be seen clearly.

The Si samples were cut into 5 mm × 8 mm pieces and were modified and characterized as described. Immediately following the surface derivatization process, the modified samples were introduced into the evaporator for metal deposition. The Ni (99.994%, Alfa AESAR) was deposited onto the electrodes at a rate of 2–5 Å s^{-1} to a thickness of ~115 Å or ~500 Å by filament evaporation. The samples used for measurements in the dark only had thicker metal films to prevent short-circuiting. A mask was used to limit the area of deposited Ni to a circular shape with an area of 0.1257 cm^2, the same size and shape as the patterned ITO front contact. Each cell could hold two samples at the same time (Figure 3.4).

2.4.4. The Fourth-generation MIS Device

The Si samples were modified as described, and 300–500 Å of Ni was deposited on the modified samples by filament evaporation immediately after the derivatization. A

mask was used during the metal deposition to allow a circular shaped metal film of an area of 0.1257 cm^2. The MIS samples were ohmic contacted on the back surface. As illustrated in Figure 3.5, cell device consisted of a Cu plate that was secured on a plastic base and a thin Rhodium (Rh) wire held steady by an insulated block was used for electrical measurements. The backside of a sample was placed on the Cu plate that served as a back contact with the aid of silver print. The tip of the Rh wire was bent and gently lowered to the front surface of the MIS sample until an electrical contact was made. The Rh wire was very thin and relatively flexible, so that it would not penetrate the metal layer on contact.

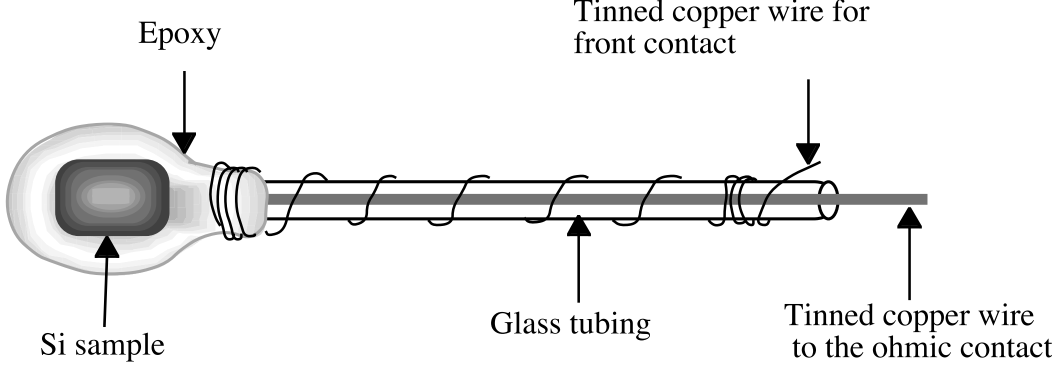

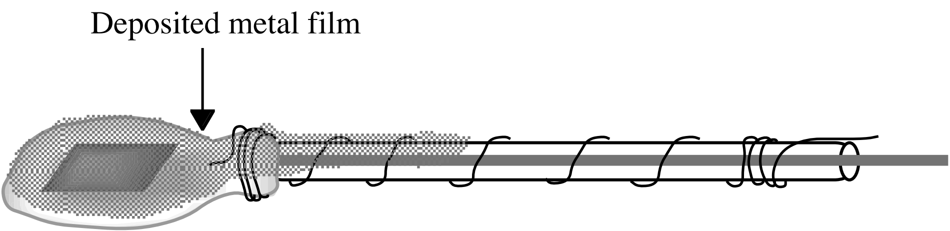

Figure 3.2

An illustration of the first-generation MIS device. The Si sample was first modified with a desired insulating layer, ohmic contacted on the backside, and made into an electrode. A Cu wire bonded to the ohmic contact was used as a back contact, and was covered by insulated epoxy. A thin Cu wire wrapped around the glass tubing was covered with the deposited metal to serve as a front contact. The metal was deposited after the epoxy was allowed to cure for at least 24 hours.

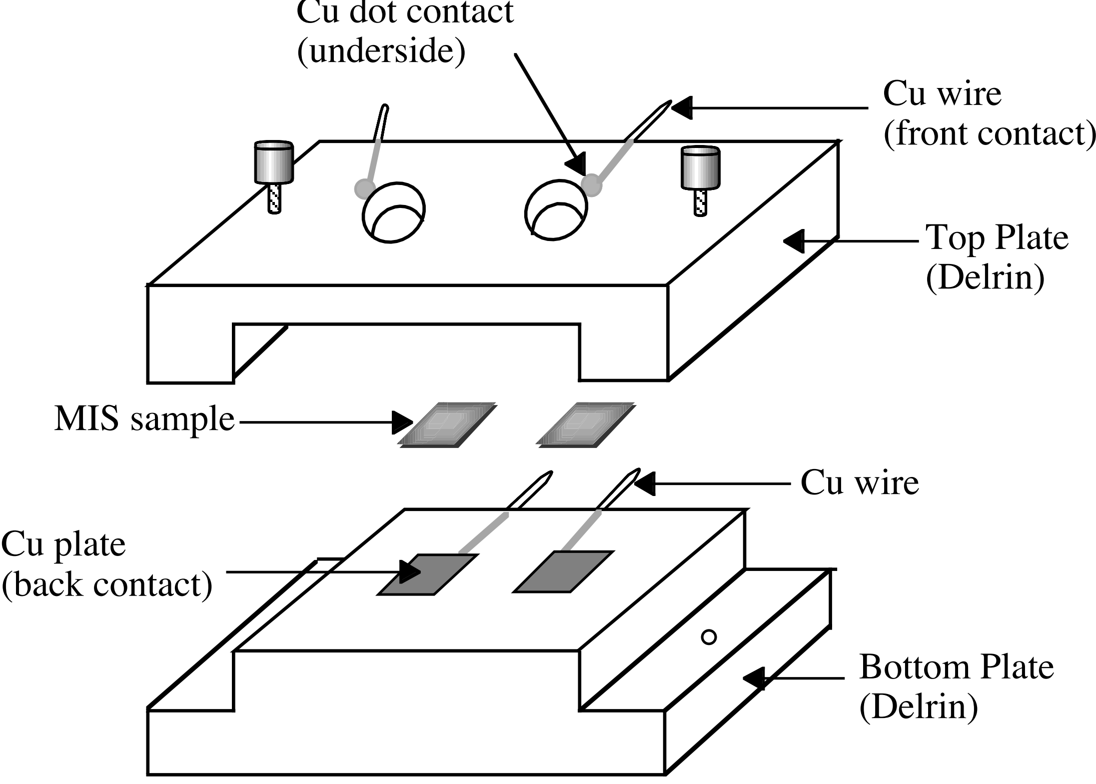

Figure 3.3

An illustration of the second-generation MIS device. The Si surfaces were modified followed by immediate metal deposition to form a MIS sample. The ohmic contacts were made on the backside of samples, silver print was painted on between the ohmic contacts and the Cu plates embedded on the bottom part of the cell. The front contacts were provided by Cu dots embedded in the underside of the cell top plate, which then came in contact with the deposited metal film on these samples. Two samples were sandwiched in a cell held together with two screws.

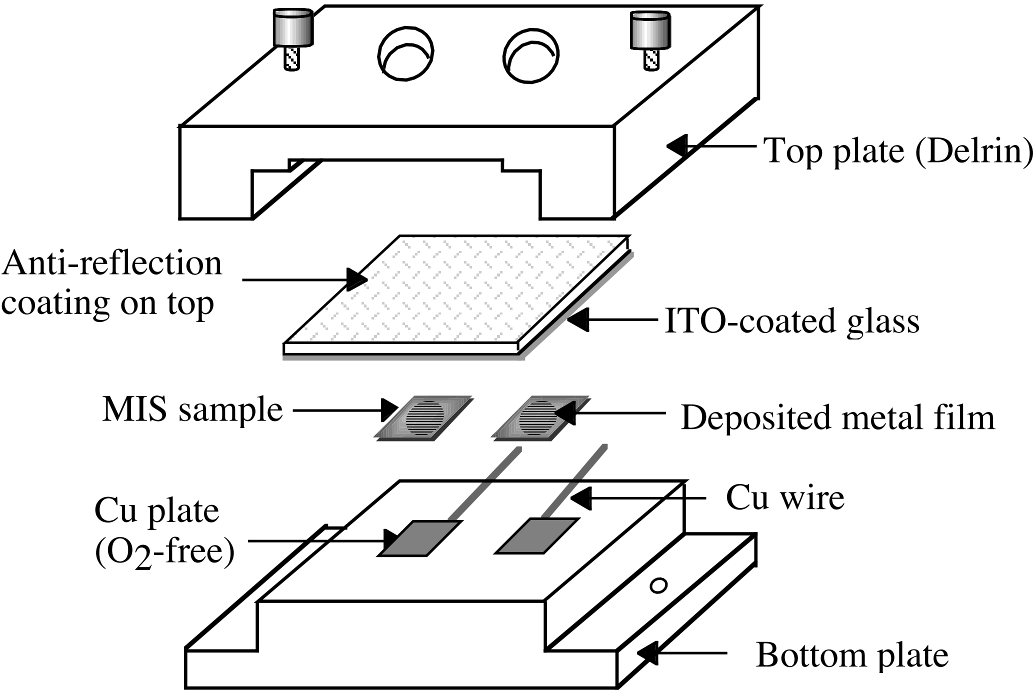

Figure 3.4

An illustration of the third-generation MIS device. The Si surfaces were modified and followed by immediate metal deposition with a mask to define the electrode area. The back contact was made the same way as the second-generation cell. The front contact was made by using pre-patterned ITO-coated glass to make an electrical contact with the deposited metal film. The antireflection coating ensured that the illumination intensity was not greatly affected by the presence of a glass slide. The cell was assembled and held tight with screws, and could hold two MIS samples for electrical measurements.

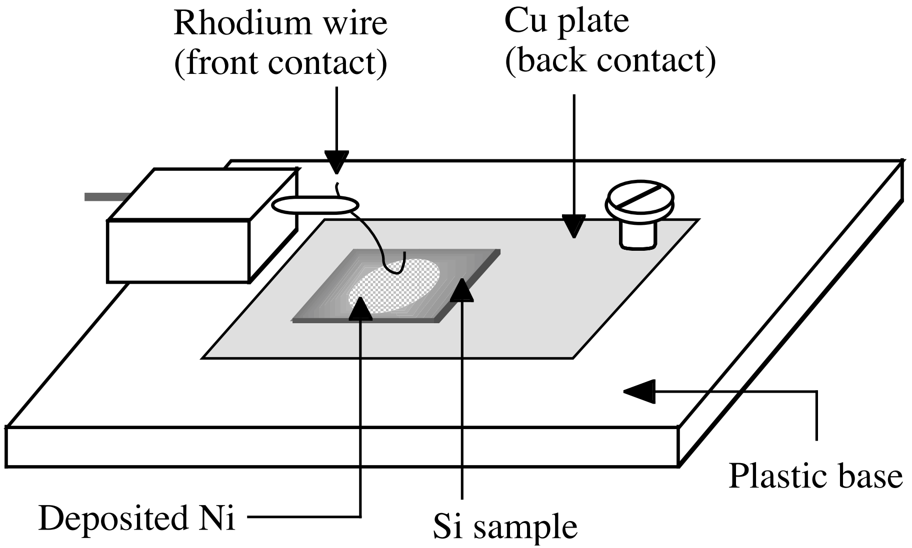

Figure 3.5

An illustration of the fourth-generation MIS device. A large Cu plate secured on a plastic base was used to back contact the MIS sample. A soft flexible Rh wire was gently place on the deposited metal film for front contact. The ohmic contact of Si was bonded to the Cu plate using silver print. A mask was also used to deposit a metal film of a circular shape with an area of 0.1257 cm^2.

2.5. Surface Characterization

All surfaces were characterized by x-ray photoelectron spectroscopy (XPS). The experiments were conducted in an M-probe surface spectrometer (VG Instrument) pumped by a CTI Cryogenics-8 cryo pump. Samples could be introduced into the UHV system using either the atmospheric load lock or the glove box load lock. The atmospheric load lock was pumped by a Varian model V80 turbo pump and a Varian model SD-300 mechanical pump, and allowed samples to be introduced into the UHV from air. The glove box load lock was pumped by a Varian model V200 turbo pump and a Varian model SD-300 mechanical pump, and enabled samples to be transferred into the UHV through a gate valve that opened to the N_2(g)-purged glove box. These load locks were brought to the atmospheric pressure by back-filling with N_2(g), and can be pumped down to approximately 10^{-7} Torr in about 10 min. Samples were mounted on a stainless steel or aluminum stub with screws.

The XPS chamber was maintained at a base pressure of less than 5×10^{-10} Torr, although the operating pressure was 5×10^{-9} to 2×10^{-8} Torr. Monochromatic Al K_α x-rays (hν = 1486.6 eV) incident at 35° from the sample surface were used to excite electrons from the sample, while the emitted electrons were collected by a hemispherical analyzer at a take-off angle of 35° from the plane of the sample surface. Data collection and analysis were done with the M-probe package software version 3.4. Survey scans were collected in the scanned mode with an elliptical spot of dimensions 800 μm × 1200 μm incident on the sample surface. The high-resolution scans were recorded in an unscanned mode with the same spot size. A typical XPS characterization of a surface consisted of one survey scan from 0–700 eV binding energy and a high resolution scan of the Si 2p region (97.57–104.59 eV binding energies).

2.6. Electrical Measurements

Electrical characterization of MIS samples was performed using a two-electrode configuration with the ohmic contact to the back of the Si as the working electrode and the metal contact on the front of the electrode as the counter/reference electrode. The electrodes and cell devices were positioned so that incident light arrived normal to the sample surface.

Current density vs. potential (*J–E*) measurements were performed using a Solartron Model 1287 potentiostat or an EG&G Princeton Applied Research (PAR) Model 173 potentiostat/galvanostat equipped with an EG&G PAR Model 175 universal programmer. When EG&G PAR Model 173 potentiostat/galvanostat was used, traces were recorded on a Houston Instruments Omnigraphic 2000 chart recorder. All curves were recorded at a scan rate of 100 mV s^{-1}. Light intensities were controlled by the use of a 300 W ENH-type tungsten-halogen bulb in conjunction with neutral density filters (ND-50, Hoya Optics). A 10 cm path-length flowing water column was used to filter out the infrared portion of the lamp output and thereby prevent excess heating of the sample.

The photoresponse experiments involved collecting the photocurrent density (J_{ph}) and the open-circuit voltage (V_{oc}) values at different illumination intensities. Direct measurements of V_{oc} and J_{ph} were taken by reading the appropriate quantities through a Fluke 27 digital multimeter. The reverse saturation current (J_0) and the diode quality factors (γ) of C_nH_{2n+1}-terminated Si (n = 2–8) /Ni junctions were obtained.

The current-voltage properties for most semiconductor diodes are found to obey the equation:[23]

$$J = J_0\left[\exp\left(\frac{-qV}{\gamma kT}\right) - 1\right] \qquad (3.2)$$

where $J_0 = A^{**}T^2[\exp(-q\phi_b/kT)]$, q is the charge on an electron, V is the applied potential, γ is the diode quality factor, k is Boltzmann's constant, T is the absolute temperature, and A^{**} is the modified Richardson's constant (for n-Si, $A^{**} \approx 120$ A/cm^2·K^2).[24] Dark J–E measurements allow the preparation of a plot of ln$J$ vs. V, which should give a linear relationship of the form:

$$\ln J \approx \frac{-qV}{\gamma kT} + \ln J_0 \qquad (3.3)$$

where J_0 and γ can be extracted from the data. When the diode is under illumination, the current can be described by adding the current from photogenerated carriers to the dark current.[25,26] Equation 3.11 can be modified to describe the J–E relationship under illumination:

$$J = J_{\mathrm{ph}} - J_0\left[\exp\left(\frac{-qV}{\gamma kT}\right) - 1\right] \qquad (3.4)$$

At open circuit ($J = 0$), Equation 3.10 is rearranged to yield the following expression:[27]

$$V_{\mathrm{oc}} \cong \frac{\gamma kT}{q}\ln\left(\frac{J_{\mathrm{ph}}}{J_0}\right) \text{ for } J_{\mathrm{ph}} >> J_0 \qquad (3.5)$$

Following this equation, a photoresponse experiment can also provide an experimental value for both γ and J_0.

Since most MS diodes are dominated by thermionic emission (i.e., $\gamma = 1$),[26] the barrier heights can be calculated from the following:

$$\phi_{\mathrm{b}} = \frac{kT}{q}\ln\left(\frac{A^{**}T^2}{J_0}\right) \qquad (3.6)$$

By using metals with different work functions to construct equivalent MS and MIS diodes, a comparison of the two measured barrier heights will allow verification of the effectiveness of the interfacial alkyl layer.

3. Results

3.1. Surface Modification

The surface modification process was monitored and verified using XPS. Figure 3.6 displays the XP spectra obtained at each step of the surface modification process. A successful etching procedure produced an H-terminated Si surface with a clean spectrum showing large Si 2p and Si 2s peaks at 99 eV and 149 eV binding energies. The smaller peaks present at successive intervals of 17.5 eV binding energy higher than the main Si 2p and 2s peaks were plasmon loss peaks, and were characteristic of Si surfaces.[28,29] Small signals due to adventitious carbon and oxygen were often observed at 284.6 eV (C 1s) and 532 eV (O 1s). The presence of adventitious carbonaceous material on the silicon surface was a result of wet chemical etching and subsequent brief handling of samples in air.[30,31] The lack of signal in the 101 to 104 eV region of the Si 2p high-resolution XP spectra collected with each survey scans suggested that the oxygen signal observed in survey spectra was not due to silicon oxide.

Figure 3.6b shows the representative spectrum of a chlorinated Si surface. Addition peaks were observed at 270 eV and 200 eV binding energies, which correspond to Cl 2s and Cl 2p peaks.[16] The subsequent Grignard reaction displaced the surface chlorine atoms, and the alkylated surface was confirmed by the disappearance of the Cl peaks and the concomitant increase in magnitude of the C 1s peak in the XP survey spectrum (Figure 3.6c). For alkyl chain lengths of up to 8 carbons, the modification process was straightforward without complication. However, the attempt to attach decyl groups to the Si surfaces resulted in significant oxide growth during the Grignard reaction.

Figure 3.6

XP survey spectra of (a) H-terminated Si, (b) Cl-terminated Si, (c) C3-terminated Si, (d) C6-terminated Si, and (e) C10-terminated Si. All spectra were normalized relative to the intensity of the Si 2p peak. The small C 1s and O 1s peak in (a) were due to advantageous C and O as a result of wet chemical etching and brief handling in air. Spectra (c)–(e) display the relative intensities of C 1s peak for 3 Si surfaces modified with alkyl chains of different lengths. The C 1s peak intensity generally increases as longer alkyl chains were attached.

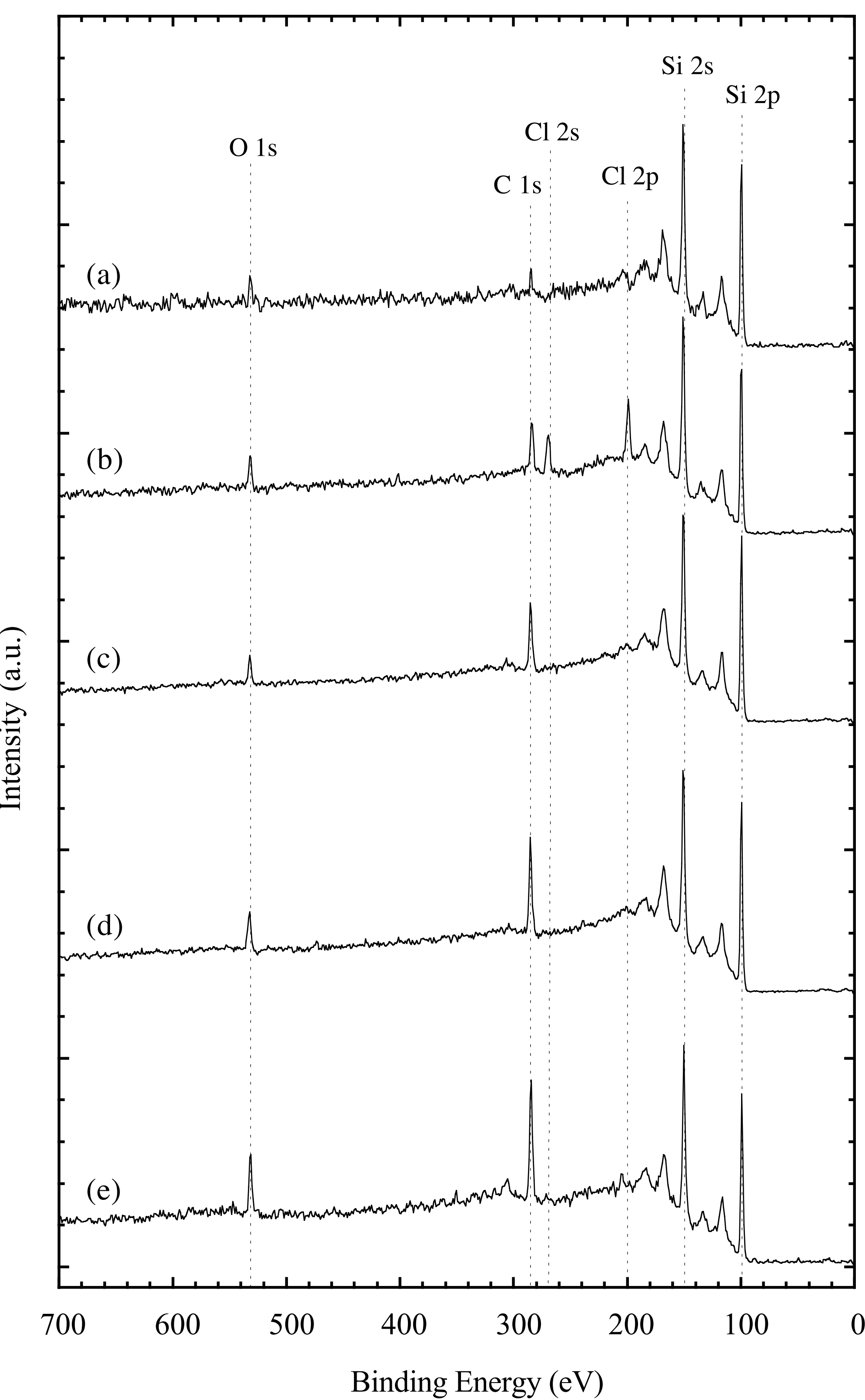
O 1s
C 1s
Cl 2s
Cl 2p
Si 2s
Si 2p
(a)
(b)
(c)
(d)
(e)
Intensity (a.u.)
700
600
500
400
300
200
100
0
Binding Energy (eV)

3.2. The *J–E* Behaviors of MIS Diodes

Figure 3.7 display the *J–E* behaviors of an H-terminated Si/Ni contact and a C_3H_7-terminated Si/Ni contact, respectively. The measurements were performed using the first-generation device. The introduction of the covalently attached propyl layer showed significant lowering of the J_0 and slight increases in the V_{oc} values at similar J_{ph}. This provided promising result for the concept of making MIS devices using alkyl chains as insulating layers. However, reproducibility in *J–E* behaviors was not achieved, as *J–E* curves looked somewhat different from one electrode to another.

The second-generation device did not work very well. The Cu dots did not make good enough electrical contacts with the deposited Ni film. The cell resistance was measured to be as high as 350 Ω. The cell resistance was lowered when silver print was used to aid the front electrical contact, however, due to the small dimension of the Cu dots, the use of silver print was somewhat difficult. In many cases the silver print dripped down the side of the sample and short-circuited the front and the back contact.

The device was modified to incorporate the use of highly conductive ITO-coated slides to make front contacts with MIS samples. This third-generation cell device certainly provided more reliable front contacts. The cell resistance was typically under 60 Ω. Although still suffered from irreproducibility between samples, a set of *J–E* behavior data was collected using a series of C_nH_{2n+2}-terminated Si (n = 2, 4, 6, and 8) modified at the same time along with an H-terminated Si. A thin layer of Ni (114 Å) was deposited on these samples at a rate of ≤2.0 Å s^{-1}. Figure 3.8 displays the *J–E* properties of these MIS junctions in the dark. The Si-H/Ni junction had a large anodic current at reverse biases indicating a very week diode behavior due to a large J_0. With an ethyl layer in between the Si and the Ni, the *J–E* curve improved significantly, although still exhibited a large reverse saturation current. When the *J–E* behaviors of C_4H_9-, C_6H_{13}-, and C_8H_{17}-terminated Si/Ni junctions were plotted together with H- and C_2H_5-terminated

Si/Ni junctions, it was clear that the insulating layers were capable of lowering the J_0 and also resulted in larger V_{oc} values.

The photoresponses of these MIS devices were also measured at several different illumination intensities. The $\ln J_{sc}$ vs. V_{oc} data were plotted in Figure 3.9. Again, the results showed the same effect observed in earlier *J–E* experiments. The C_8H_{17}-terminated Si/Ni junction was the best choice of all devices tested, with a lower J_0 and higher V_{oc} value compare to the other junctions tested. Because the *J–E* behaviors of both Si-H and Si-C_2H_5/Ni junctions did not follow the diode equation, and anodic currents did not level out in the reverse bias region studied, a quantitative calculation was not possible. A time dependence of several C_8H_{17}-terminated Si/Ni junctions *J–E* behaviors was also performed. The samples were left in the air for 3 days and the *J–E* curve of each device was collected every 24 hours. As depicted in Figure 3.10, this junction was not air stable and the *J–E* characteristics deteriorate quickly to show large resistance in the forward bias region.

Since the third-generation device still did not allow reproducible data to be collected, the fourth-generation device that was very similar to the device used for prior MIS study in our laboratory was tested.[15] A larger number of the same surface was made at the same time to insure the same quality control. The attempts to achieve reproducible *J–E* behaviors for several types of surfaces were unsuccessful.

Figure 3.7

J–E behaviors of (a) H-terminated and (b) C_3H_7-terminated Si in contact with 450 Å of Ni. The plots were collected using the first-generation cell device. The plots were collected at a scan rate of 100 mV s^{-1}. A significant lowering of the anodic currents at reverse biases suggested that the junction recombination current was lowered when an insulating layer was introduced between the Si and the contacting Ni. The illumination intensities were kept the same for both devices.

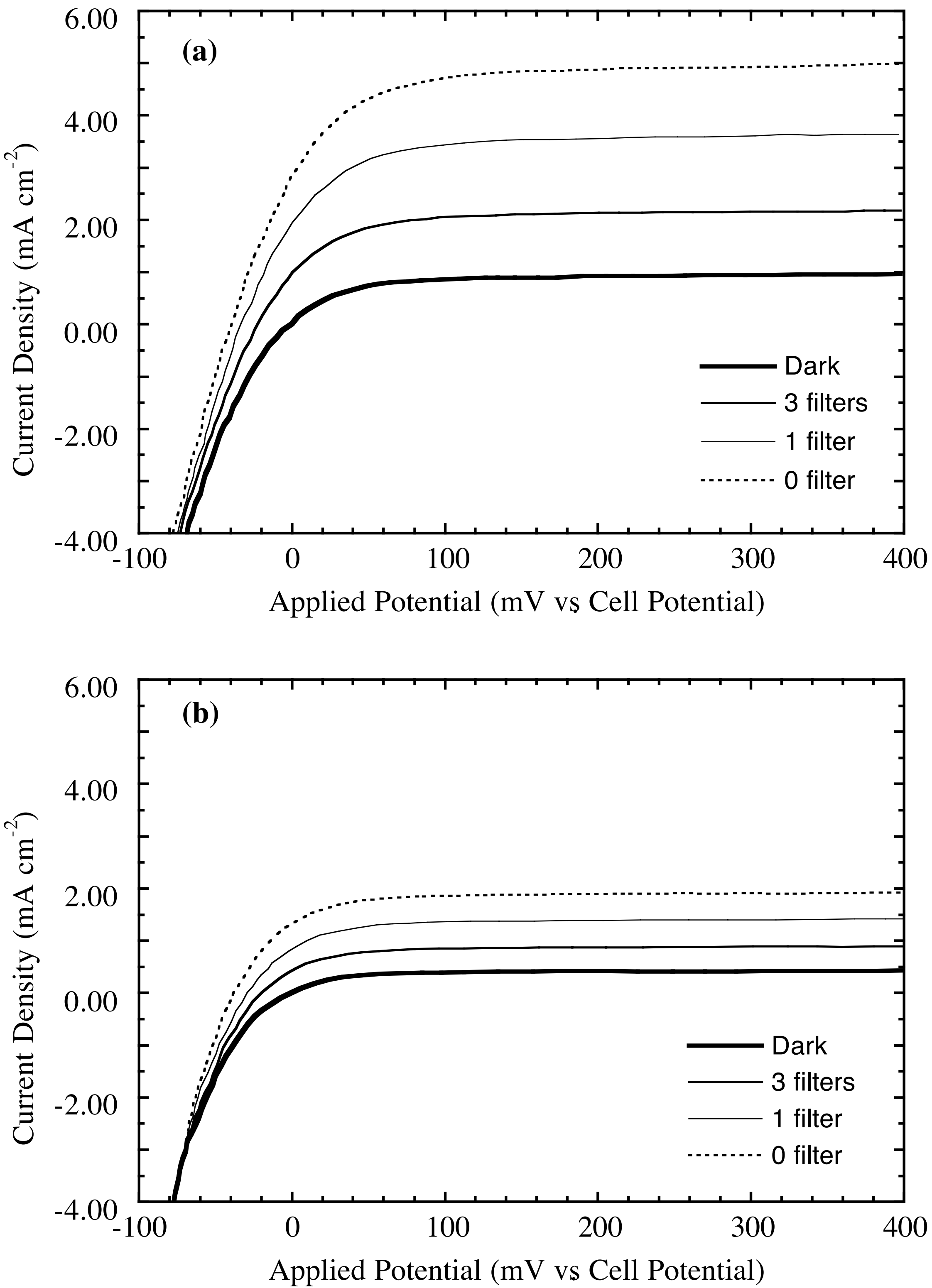
(a)
6.00
4.00
2.00
0.00
-2.00
-4.00
-100
0
100
200
300
400
Current Density (mA cm-2)
Applied Potential (mV vs Cell Potential)
Dark
3 filters
1 filter
0 filter
(b)
6.00
4.00
2.00
0.00
-2.00
-4.00
-100
0
100
200
300
400
Current Density (mA cm-2)
Applied Potential (mV vs Cell Potential)
Dark
3 filters
1 filter
0 filter

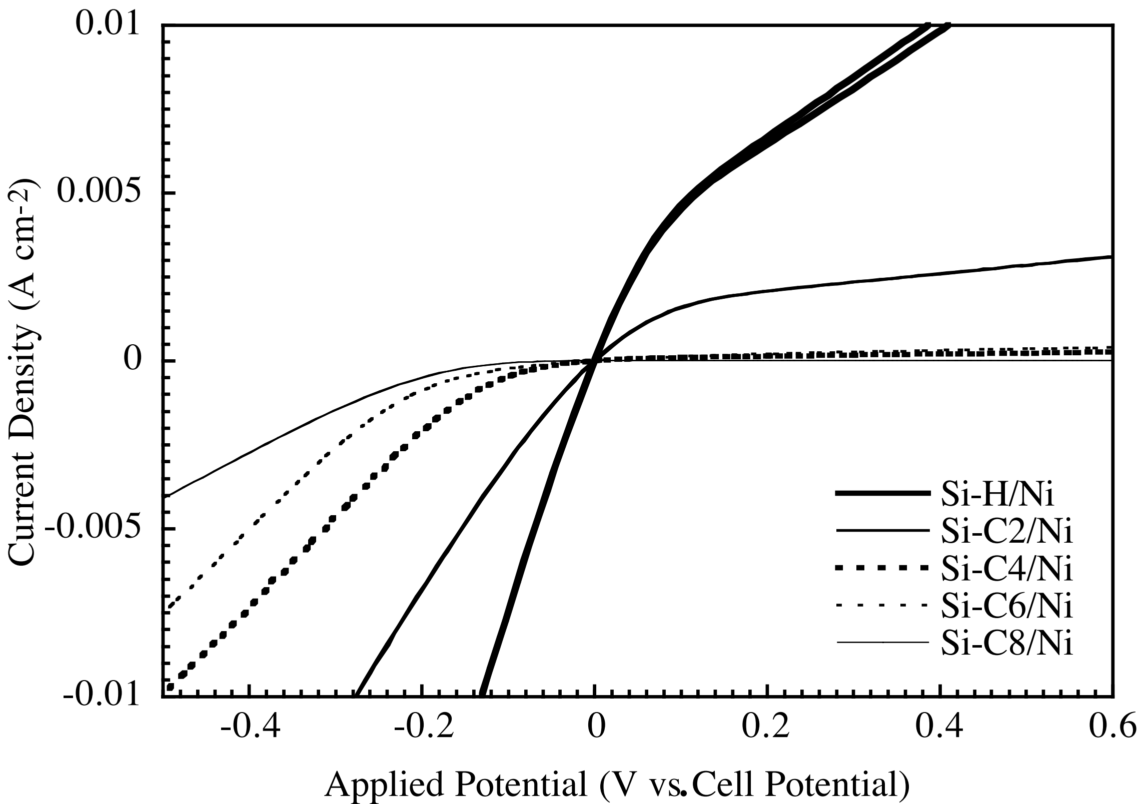

Figure 3.8

J–E behaviors of a series of C_nH_{2n+1}-terminated Si/Ni (n = 2, 4, 6, and 8) and an H-terminated Si/Ni junctions in the dark. The data show the dependence of the MIS junction *J–E* behavior on the alkyl chain length. The MIS junction with the longest insulator chain length exhibited the lowest anodic current at reserve biases. The MIS diode constructed using a thicker insulator was more resistive at forward bias.

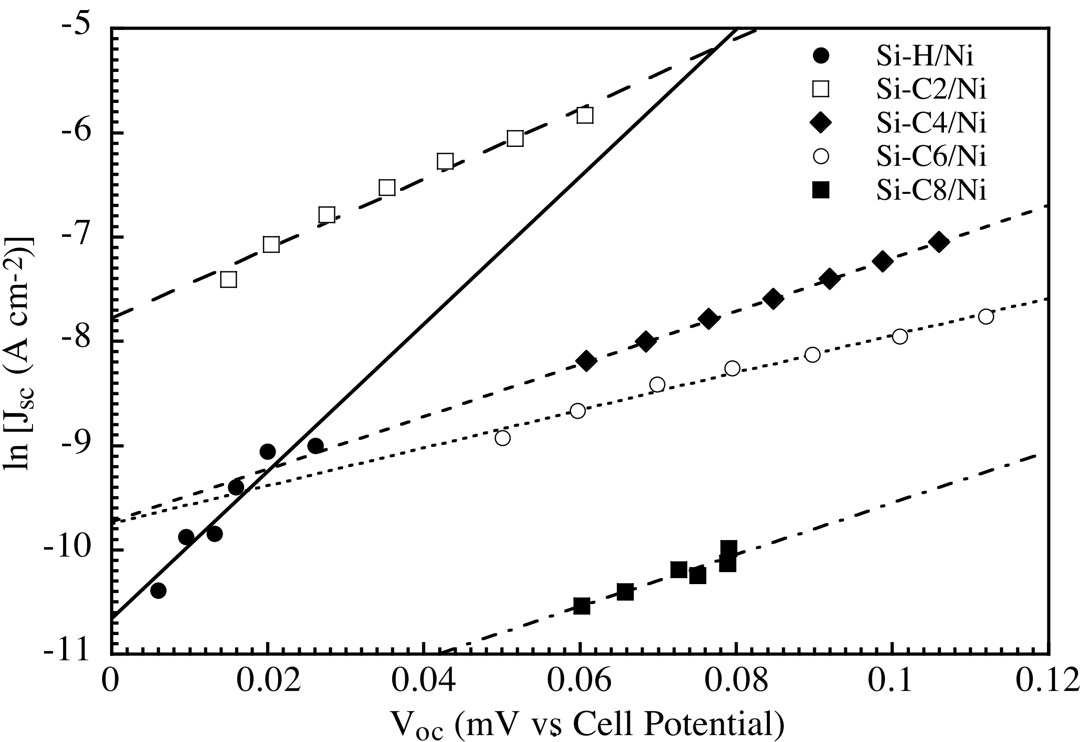

Figure 3.9

Photoresponses of a series of C_nH_{2n+1}-terminated Si/Ni (n = 2, 4, 6, and 8) and an H-terminated Si/Ni junctions. These are plots of the individual photoresponses of the same devices investigated in Figure 3.8.

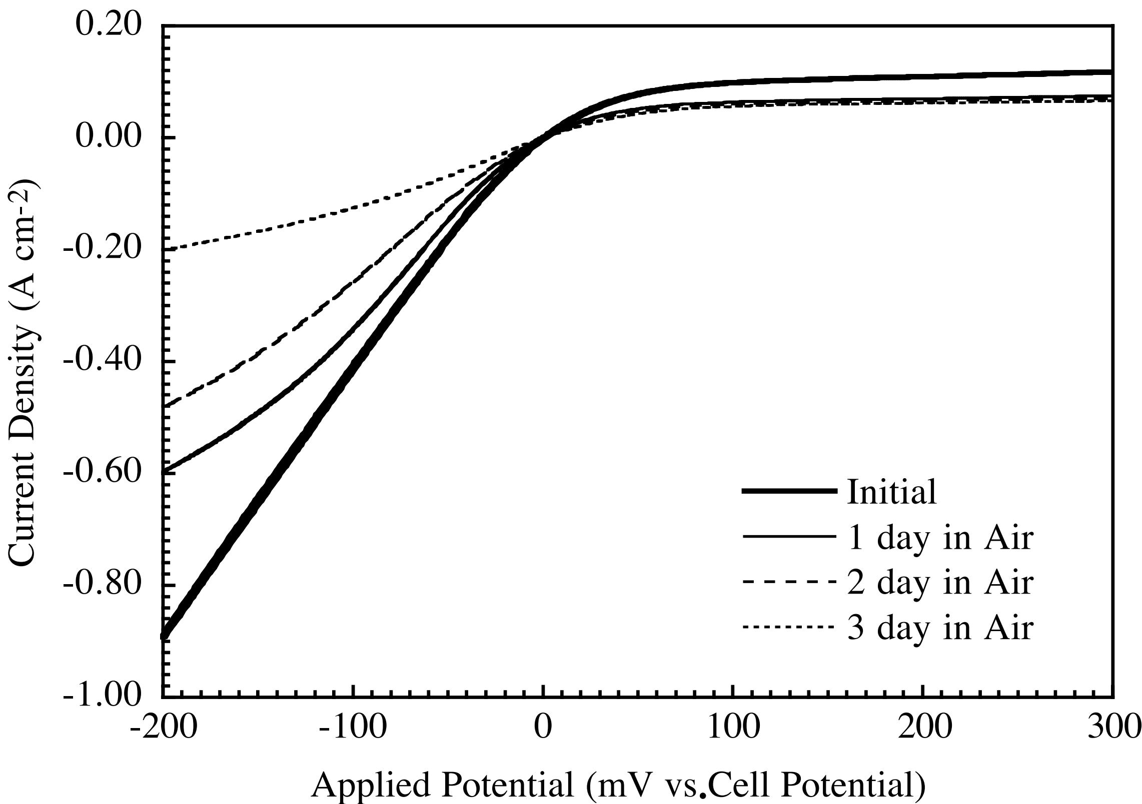

Figure 3.10

Time-dependent *J–E* behavior of a C_8H_{17}-terminated Si/Ni junction in the dark. The MIS device constructed was not stable in air. The device resistance increased during the course of 3 days, which suggested the possibility of unfavorable interfacial reaction.

4. Discussions

The XPS data confirmed that the two-step chlorination/alkylation method yielded reproducible alkyl overlayer on a Si(111) surfaces. The model suggested that the best possible coverage for an alkylated Si is a half-monolayer coverage (as a 2×1 unit cell), with the exception of methylated surface, which could exhibit one-monolayer coverage. Since the area of the 2×1 unit cell on Si(111) surface is significantly larger than the area required for an alkyl chain in a tightly packed environment, the alkyl overlayer could be quite porous.[22] Although the methyl overlayer could provide a better coverage, it was too thin to alter the electrical properties of an H-terminated Si/Ni contact. In fact, the data showed that there was no significant effect when an alkyl chain of shorter than 3 carbons was used as the insulating layer. A longer alkyl chain, on the other hand, could tilt to make the overlayer surface less porous and provide a necessary barrier against silicide formation. However, the possible introduction of an additional series resistance was observed in J–E plots.

The irreproducibility problem could arise from the junction formation process rather than the design of devices for measurements. Thermal evaporation of Ni requires relatively high temperature, and the organic layers on these samples could disintegrate or get damaged under excess heat. The dust could also introduce problems during evaporation and result in inconsistent interfaces. If the metal was deposited in the pin holes or if the hot metal burnt through the organic insulator, the MIS junctions could produce unreliable data, making it difficult to analyze the experimental results quantitatively.

As an alternative to the porosity problem, linear fluorocarbon chains can be used to derivatize the Si surface instead of alkyl chains. The larger head groups of fluorocarbon chains could serve as a blocking layer and might result in a much more

chemically impenetrable coverage, therefore a better barrier against metal penetration in a MIS contact.

Different metal deposition methods can also be investigated. Electroless deposition of gold or nickel onto GaP has been reported to yield almost ideal Schottky diodes.[32] Palladium and copper contacts to Si have also been made using an electroless process.[33,34] Metal-binding agents such as thiols can be incorporated into the monolayer head group, which can in turn bind colloidal Au and Pt.[35,36] Electrodeposition can also be adapted to plate a metal layer on the alkyl monolayer-Si substrate with a well controlled thickness.[37,38] There are however other concerns for liquid phase deposition. It is unclear as to how the trapped liquid molecules might affect the electrical properties of the junction. Since the alkyl layer is somewhat porous, the liquid could actually come in contact with Si substrate and either induce oxide growth or allow the metal deposition to occur directly on the Si surface where it's not covered. Electroplating current would prefer to go through the areas with the least resistance, and this could mean that it is easier for metal plating to occur at the sites of pin holes, which again decreases the effectiveness of insulating layer.

Another approach for the fabrication of MIS diodes is mass production of the same junction. By making large batches of junctions for measurements, it would be possible to recognize and discard unreliable data from each set of measurement. This could be achieved by modifying the surfaces of large wafers instead of smaller size samples, followed by depositing metal dots or islands to form a large number of junctions on each modified wafer. Since it is easier to have a smaller area of modified surface to be free of defect than the whole sample surface, those metal dots that were deposited on a region that has no pin hole would be able to provide reliable data for junction characterizations.

Once an effective alkyl monolayer is obtained, different metals should be deposited onto both H-terminated Si and derivatized Si to make equivalent MS and MIS

diodes. In an order of decreasing metal work functions, metals that can be used are Pt, Pd, Au, Rh, Ni, Co, Cu, Cr, Al, and Ag. Pt, Pd, and Au should yield large barrier heights at unpinned metal/*n*-type Si junctions, while Ag, Al, and Cr/*n*-Si interfaces should produce a $V_{oc} \approx 0$ due to theoretically low barrier heights.

5. Summary

Several different chain lengths of alkanes, from methyl to octyl groups, have been successfully attached to the *n*-Si(111) surface using a two-step chlorination/alkylation method. Contacting Ni layers of thicknesses ranging from 115 Å to 500 Å have been thermally evaporated onto both freshly etched H-terminated and alkyl-terminated Si, and the *J–E* behaviors of these resulting junctions have been investigated. Introduction of a monolayer with a chain length longer than 4 carbons between the Ni and the Si was shown to consistently lower the value of J_0 while an increase in the values of V_{oc} were observed. A general trend of an increased effectiveness was shown for longer alkyl chains, but the thicker films also introduced larger cell resistances. Although reproducibility of the MIS *J–E* properties could not be achieved despite the use of several different cell devices, some suggestions were presented for possible future work.

6. Acknowledgments

I thank Reynold Johnson in the Department of Applied Physics for assisting with the photoresist patterning.

7. References

(1) Braun, F. *Ann. Phys. Chem.* **1874**, *153*, 556.

(2) Sharma, B. L., Ed. *Metal-Semiconductor Schottky Barrier Junctions and Their Applications*; Plenum: New York, 1984.

(3) Schottky, W.; Stromer, R.; Waibel, F. *Hochfrequenztechnik* **1931**, *37*, 162.

(4) Schottky, W. *Naturwissenschaften* **1938**, *26*, 843.

(5) Mott, N. F. *Proc. Camb. Phil. Soc.* **1938**, *34*, 568.

(6) McGill, T. C. *J. Vac. Sci. Technol.* **1974**, *11*, 935.

(7) Bardeen, J. *Phys. Rev.* **1947**, *71*, 717.

(8) Heine, V. *Phys. Rev. A* **1965**, *138*, 1689.

(9) Schmid, P. E.; Ho, P. S.; Foll, H.; Tan, T. Y. *Phys. Rev. B-Condens Matter* **1983**, *28*, 4593.

(10) Schmid, P. E. *Helv. Phys. Acta* **1985**, *58*, 371.

(11) Rhoderick, E. H.; Williams, R. H. *Metal-Semiconductor Contacts*; 2nd ed.; Oxford University Press: New York, 1988.

(12) Ottaviani, G.; Tu, K. N.; Mayer, J. W. *Phys. Rev. Lett.* **1980**, *44*, 284.

(13) Freeouf, J. L.; Rubloff, P. S.; Ho, P. S.; Kuan, T. S. *J. Vac. Sci. Technol.* **1980**, *17*, 916.

(14) Andrews, J. M.; Phillips, J. C. *Phys. Rev. Lett.* **1975**, *35*, 56.

(15) Rosenblum, M. D. Ph. D., Stanford University, 1988.

(16) Bansal, A.; Li, X.; Lauermann, I.; Lewis, N. S.; Yi, S. I.; Weinberg, W. H. *J. Am. Chem. Soc.* **1996**, *118*, 7225.

(17) Linford, M. R.; Chidsey, C. E. D. *J. Am. Chem. Soc.* **1993**, *115*, 12631.

(18) Linford, M. R.; Fenter, P.; Eisenberger, P. M.; Chidsey, C. E. D. *J. Am. Chem. Soc.* **1995**, *117*, 3145.

(19) Higashi, G. S.; Chabal, Y. J.; Trucks, G. W.; Raghavachari, K. *Appl. Phys. Lett.* **1990**, *56*, 656.

(20) Wyman, D. P.; Wang, J. Y. C.; Freeman, W. R. *J. Org. Chem.* **1963**, *28*, 3173.

(21) Hassler, K.; Koll, W. *J. Organomet. Chem.* **1995**, *487*, 223.

(22) Bansal, A. Ph. D., California Institute of Technology, 1997.

(23) Sze, S. M. *The Physics of Semiconductor Devices*; 2nd ed.; Wiley: New York, 1981.

(24) Andrews, J. M.; Lepselter, M. P. *Solid State Elec.* **1970**, *13*, 1011.

(25) Fonash, S. J. *Solar Cell Device Physics*; Academic: New York, 1981.

(26) Fahrenbruch, A. L.; Bube, R. H. *Fundamentals of Solar Cells: Photovoltaic Solar Energy Conversion*; Academic: New York, 1983.

(27) Kumar, A.; Wilisch, W. C. A.; Lewis, N. S. *CRC Critical Rev.* **1993**, *18*, 327.

(28) Stinespring, C. D.; Wormhoudt, J. C. *J. Appl. Phys.* **1989**, *65*, 1733.

(29) Cheng, K. L. *Japan. J. Appl. Phys.* **1995**, *34*, 5527.

(30) Tufts, B. J.; Kumar, A.; Bansal, A.; Lewis, N. S. *J. Phys. Chem.* **1992**, *96*, 4581.

(31) Mende, G.; Finster, J.; Flamm, D.; Schulze, D. *Surf. Sci.* **1983**, *128*, 169.

(32) Gol'dberg, Y. A.; Posse, E. A.; Tsarenkov, B. V. *Electron. Lett.* **1971**, *7*, 601.

(33) Datta, A. K.; Ghosh, K.; Mitra, R. N.; Daw, A. N. *Solid-St. Electron.* **1980**, *23*, 99.

(34) Datta, A. K.; Ghosh, K.; Chowdhury, N. K. D.; Daw, A. N. *Solid-St. Electron.* **1980**, *23*, 905.

(35) Natan, M. J.; Thackeray, J. W.; Wrighton, M. S. *J. Phys. Chem.* **1986**, *90*, 4089.

(36) Freeman, R. G.; Grabar, K. C.; Allison, K. J.; Bright, R. M.; Davis, J. A.; Natan, M. J. *Science* **1995**, *267*, 1629.

(37) Bocking, C.; Christie, I. R. *Inter. Sci. Rev.* **1992**, *17*, 239.

(38) Searson, P. C. *Solar Energ Mater Solar Cells* **1992**, *27*, 377.

Chapter 4

Transient Photoconductivity Decay Measurements of Polymer-Terminated Silicon Surfaces

1. Introduction

The fabrication of conducting and/or nonconducting organic overlayers on crystalline Si surfaces is of interest for inhibiting of surface corrosion processes,[1] for providing routes to chemical control over the electrical properties of Schottky barrier-like structures,[2] for enabling novel lithographic strategies that utilize contact printing and photopatterning,[3-5] for producing novel metal-insulator-semiconductor devices,[6] and for controlling the electrical recombination properties of Si surfaces,[7,8] amongst other applications. To obtain acceptable electrical device properties, many of these applications require direct functionalization of the Si surface in a fashion that does not introduce significant densities of interfacial electronic defect levels. The presence of a native oxide on Si is largely unacceptable for such purposes because the resulting Si/Si oxide interface is often highly electrically defective.[9,10] In addition, the oxide acts as a tunneling barrier for charge carriers and the uniformity of this barrier is difficult to control at the molecular level. Thermally grown silicon oxides generally contain fixed positive charge,[9,11-13] which also limits the types of electrical device behavior that can be obtained from such interfaces. The ability to form electrically conductive or nonconductive overlayers of controlled thickness on Si without relying on reactions that utilize functionality arising from native and/or thermally grown Si oxides would be important and desirable for future technological advancements.

Langmuir-Blodgett techniques[14] have been used to synthesize organic thin films with controlled structure and composition; however, the fragility of the resulting films represents a major obstacle to practical implementation. Another method that has been adopted for controlling the surface properties of a solid is by functionalizing the surface with tethered polymer chains, called polymer brushes. Polymer brushes are polymers confined to a small volume near an interface, and restrictions due to steric requirement

force the chains to stretch away from the grafting point to the edge of polymer layer. Several strategies have been employed to prepare brush-type polymer layers, including selective physisorption of block copolymers,[15-17] chemical grafting of preformed polymer chains onto the surface ("grafting to"),[18-20] and "grafting from" methods that involve surface-initiated polymerization.[21-27] As adsorbed block copolymers face a disadvantage of thermal instability, more robust films have been obtained using polymers with functionalities appropriate for covalent attachment to surfaces. The significant improvement in physical properties, however, generally is accompanied by a loss of control over the order and composition of the overlayer. The "grafting to" approach also produces polymer layers with low grafting density. Crowding of the chains at the surface occurs as more polymers are grafted onto the substrate, which hinders the diffusion of reactive chain ends to the surface for further grafting. The surface-initiated polymerization can overcome this limitation by first attaching reactive units that are able to initiate polymerization on the substrate, leaving the propagating polymer chains to grow away from the surface. Since the smaller monomer can readily access the initiator site at the end of propagating chain, the grafting density is greatly increased. Examples of the "grafting from" method for Si surface modification include radical chain polymerization initiated by surface-bound azo compounds,[24] sequential cationic and atom transfer radical polymerization,[25] living free radical polymerization,[27] polymerization by organometallic initiators,[26] and ring-opening metathesis polymerization.[21] However, all these polymerization techniques utilize the reactions between chlorosilane moieties and silicon oxide surfaces, and result in an intervening Si oxide layer between the Si and surface functionality (see Figure 4.1). In order to prepare polymer-modified Si surfaces that are suitable for electronic device applications, a method was developed for the formation of an organic overlayer directly on the Si substrate through a covalent Si-C linkage.

Crystalline Si has recently been functionalized using a variety of approaches;[28-42] notably, alkylation of crystalline, (111)-oriented Si using a two-step chlorination/alkylation procedure can produce functionalized surfaces that have a very low surface recombination velocity.[8,43] This modification method was developed and thoroughly characterized by Ashish Bansal, and was crucial for the work of this chapter. The work described in this chapter was also inspired in part by a prior study of Weck et al., who first showed the possibility of producing surface-immobilized polymer brushes using surface-initiated ring-opening metathesis polymerization (ROMP). They reported the polymerization of substituted norbornenes from a modified gold surface using a Ru-based alkylidine as initiator, though only small amounts of polymer chains were formed.[44] This chapter describes the extension of chlorination/alkylation chemistry, combined with ROMP methods, to produce polymer overlayers that are covalently attached directly to a Si(111) surface and provide molecular-level control over the thickness and electronic properties of the resulting Si/polymer contacts.

Figure 4.1

Examples of polymer-terminated Si reported in literature utilizing “graft from” approach to form covalently attached polymers or block copolymers on Si surfaces. The surface-initiated polymerization method includes (a) radical chain polymerization initiated by surface-bound azo compounds,[24] (b) sequential cationic and atom transfer radical polymerization,[25] (c) living free radical polymerization,[27] (d) polymerization by organometallic initiators,[26] and (e) ring-opening metathesis polymerization.[21] All above methods relied on chlorosilane chemistry to link the polymer layer to the SiO_2 substrate, and resulted in an intervening oxide layer which can be unsuitable for electronic device applications that require a low surface defect density.

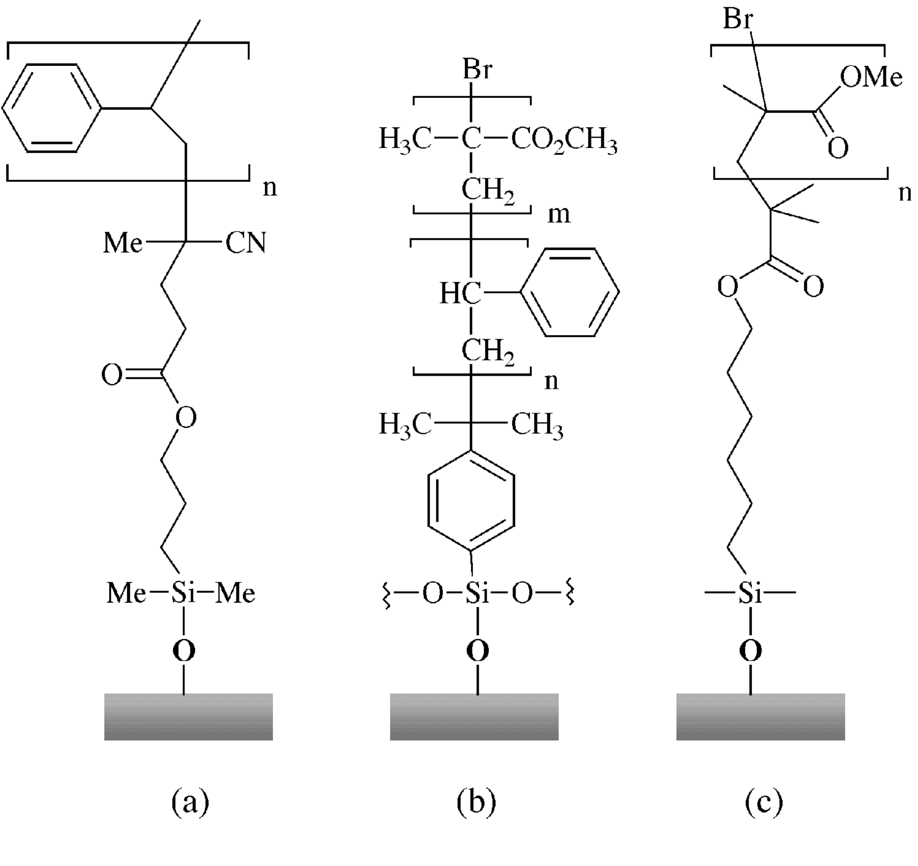
Br
OMe
O
n
Me
CN
O
O
Me-Si-Me
O
Br
$H_3C-C-CO_2CH_3$
CH_2
m
HC
CH_2
n
$H_3C-C-CH_3$
O-Si-O
O
Si
O
O
(a)
(b)
(c)

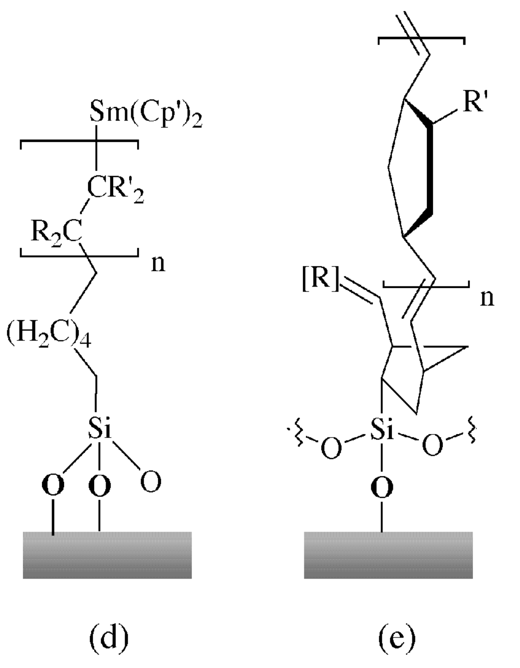
Sm(Cp')$_2$
CR'$_2$
R$_2$C
n
(H$_2$C)$_4$
Si
O O O
R'
[R]
n
O-Si-O
O
(d)
(e)

2. Experimental

2.1. Chemicals

All solvents used for surface modification, including acetonitrile, chlorobenzene, 1,2-dichloroethane, dichloromethane, methanol, and tetrahydrofuran (THF), were purchased from Aldrich or Acro in the anhydrous form and used as received. Solvents were stored over activated 3 Å molecular sieves (EM Science) in an N_2(g)-purged glove box. Solvents used for wafer degreasing, acetone, dichloromethane, methanol, and 1,1,1-trichloroethane, were either reagent grade (GR) or Omnisolve grade obtained from EM Science and used as received. Hydrogen peroxide (30%) was purchased from EM Science, and H_2SO_4(aq) was obtained from J.T. Baker. Hydrofluoric acid buffered with ammonium fluoride (NH_4F/HF, buffered HF) and 40% ammonium fluoride (NH_4F) solutions were purchased from Transene Co. Phosphorus pentachloride (PCl_5), benzoyl peroxide, allylmagnesium chloride (CH_2=$CHCH_2MgCl$, 1.0 M in THF) were obtained from Aldrich and were used without further purification. The ring-opening metathesis catalyst [$RuCl_2$(=CHPh)$(PCy_3)_2$, Cy = cyclohexyl] (**1**) was obtained from Materia while [$RuCl_2$(=CHPh)(PCy_3)($IMesH_2$), IMes = dimesityl-imidazolidene] (**2**) was provided by O. A. Scherman.[45] Monomers norbornene (Aldrich) and dicyclopentadiene (DCPD, Materia) were dissolved in anhydrous 1,2-dichloroethane and anhydrous dichloromethane, respectively. 1,3,5,7-Cyclooctatetraene (COT) was obtained from BASF and dried over CaH_2, while 1,5-Cyclooctadiene (COD) was purchased from Aldrich. Both COD and COT were distilled before used. C5, C4, and C6 olefin Grignard reagents, 4-pentenylmagnesiumbromide (CH_2=$CH(CH_2)_3MgBr$, ~1.0 M in THF), 3-butenylmagnesiumbromide (CH_2=$CH(CH_2)_3MgBr$, ~1.5 M in THF) and the 5-

hexenylmagnesiumbromide (CH_2=CH(CH_2)$_4$MgBr, ~1.0 M in THF), were provided by O. A. Scherman.

2.2. Preparation of Substrates

Single-crystal, (111)-oriented, *n*-type float-zone silicon wafers were obtained from Topsil Semiconductor Materials. The double-side polished wafers were 280 ± 20 μm thick, and phosphorous-doped with resistivities of 3500–6500 Ω·cm as specified by the manufacturer. The bulk lifetime of 6760 μs was measured by the photoconductive decay method at the manufacture. The silicon wafers were first oxidized in a "Pirhana" solution which consisted of 3:1 (v/v) concentrated H_2SO_4(aq):H_2O_2 (30%) heated to approximately 100 °C for one hour.[33] **Caution:** *The acidic "Pirhana" solution is extremely dangerous, particularly in contact with organic materials and should be handled carefully*. The wafers were then rinsed with copious amount of 18.0 MΩ·cm resistivity water (obtained from a Barnstead Inc. Nanopure water purification system), dried under pressurized N_2(g), and stored for future use. Before surface modifications, the wafer was cut into approximately 9 mm × 9 mm size samples. Each piece was briefly sonicated in 18.0 MΩ·cm resistivity water, degreased by rinsing sequentially with methanol, acetone, 1,1,1-trichloroethane, dichloromethane, 1,1,1-trichloroethane, acetone, and methanol, and followed by another brief sonication in water. After blow drying with N_2(g), the samples were etched in NH_4F/HF (buffered HF) for 30 seconds, and then directly immersed in 40% NH_4F for 15–20 min.[46] Following the etching process, the samples were rinsed with 18.0 MΩ·cm resistive water (obtained from Barnstead E-pure filtration system), and dried under a stream of N_2(g). The samples were quickly mounted onto the XPS stubs and introduced into ultrahigh vacuum (UHV) system that houses the x-ray photoelectron spectroscopy (XPS) via an atmospheric load lock for immediate surface characterization.

2.3. Surface Modification

All surface modification procedures were carried out in an N_2(g)-purged glove box which is connected to the UHV system housing the XPS spectrometer via a gate valve. Figure 4.2 depicts the schematic experimental approach: (i) an alkenyl linker of variable length is coupled to a chlorinated Si surface using a Grignard reaction; (ii) an olefin cross-metathesis reaction is used to obtain a surface-bound ruthenium ring-opening metathesis polymerization (ROMP) catalyst layer, and (iii) a monomer is added to effect growth of polymer onto the surface.

2.3.1. Chlorination

After verifying that the etching process was successful as determined by the absence of oxide on the Si surfaces, the samples were brought into the N_2(g)-purged glove box directly through the gate valve. The stock chlorinating solution was prepared by dissolving excess PCl_5 in chlorobenzene to form a saturated solution (typically 0.6–0.7 M). The solution was warmed to about 60 °C for at least 1 hour to dissolve as much PCl_5 as possible. Immediately before use, a small portion of the stock chlorinating solution was poured into a small beaker, and a few grains of benzoyl peroxide were added (approximately 30–40 mg of benzoyl peroxide in 10 ml of PCl_5-chlorobenzene solution) as a radical initiator.[47,48] With the samples completely immersed in this solution and the beaker covered by a watch glass, the reaction was heated to 90–100 °C for 45–60 min. The samples were then taken out of the chlorinating solution, rinsed with anhydrous THF followed by anhydrous methanol or anhydrous dichloromethane, and dried in a stream of N_2(g). Some samples were mounted on the XPS stub and brought into the UHV system for surface characterization.

2.3.2. Terminal-Olefin Addition via Grignard Reaction

The chlorinated Si samples were placed in separate test tubes so that Si pieces were in standing position and the surfaces did not touch the bottom of reaction vessels. The olefin Grignard reagent was then added to each test tube and heated to 65–80 °C for 8–18 hours. The reaction time varied according to the chain length of the terminal olefin group (see Table 4.1). Two procedures requiring different types of test tubes and rinsing solvents were adapted depending on the Grignard reagent used. When allylmagnesium chloride (Aldrich) or C4 olefin Grignard was used, the reaction took place in test tubes capped with septa. Following the overnight reaction, the samples were rinsed with copious amount of anhydrous THF and anhydrous methanol, individually immersed in anhydrous methanol in screw-capped vials, and taken out of the glove box for sonication. The derivatized samples were sonicated in anhydrous methanol and anhydrous acetonitrile for 5 min each, dried in a stream of $N_2(g)$ before being mounted on the XPS stub, and introduced into UHV through atmospheric load lock for surface characterization.

Due to a longer reaction time when C5 or C6 olefin Grignard was used, it was necessary to eliminate as much methanol vapor in the glove box as possible. Prior to the reaction, fresh phosphorous pentaoxide (P_2O_5) powders were poured into an evaporation dish and used as a drying agent to absorb solvent vapors in the glove box. Anhydrous dichloromethane was used in place of anhydrous methanol throughout the surface modification procedures. The samples were immersed in anhydrous dichloromethane when taken out of the glove box and sonicated in anhydrous dichloromethane, anhydrous methanol, and anhydrous acetonitrile for 5 min each. During the reaction, the samples were also isolated from the glove box atmosphere by using teflon-lined screw-capped test tubes instead of septa-capped ones. For each experiment, only a fresh portion of homemade Grignard reagent was brought into the glove box in a Schlenk tube, and the

portion was defrosted by warming to ~45 °C immediately before use. Allylmagnesium chloride bottle was stored in the glove box for no more than one month, and the solution was drawn with a syringe through the Sure/Seal cap.

2.3.3. Catalyst Addition

Olefin-terminated-Si samples were placed into several screw-capped vials containing a ruthenium-alkylidine ring-opening metathesis catalyst solution for at least 3 hours. Then the samples were washed copiously with anhydrous dichloromethane and dried with a stream of N_2(g). The ruthenium catalyst solution was made immediately prior to use by dissolving $Cl_2(Cy_3P)_2Ru$=CHPh (**1**, ~25 mM) in anhydrous dichloromethane. A more powerful catalyst $Cl_2(H_2IMes)(PCy_3)Ru$=CHPh (**2**, ~10 mM in anhydrous dichloromethane) was also used for some experiments involving polymerizing cyclooctatetraene (COT) and norbornene.

2.3.4. Polymerization

The stock norbornene solution (2.44 M) was made by dissolving norbornene in anhydrous 1,2-dichloroethane and stored in a Schlenk tube covered with an aluminum foil. In screw-capped vials, less concentrated norbornene solutions (0.01 M, 0.05 M, 0.09 M, 0.15 M, 0.18 M, 0.27 M, and 0.45 M) were made from the stock prior to catalyst addition reaction. This is to minimize the exposure of the stock solution to any ruthenium catalyst in the glove box atmosphere. Small vials that allow only the edges of a sample to touch the vial wall and the bottom were used. The desired monomer solution was then added into the vials and the vials were capped quickly. The standard reaction time for norbornene, COD, and COT was 30 min at room temperature, and then washed with copious amount of anhydrous dichloromethane and dried in a stream of N_2(g). The dicyclopentadiene (DCPD) polymerization was carried out by first immersing the samples in a DCPD solution (2.5 M in dichloromethane) for 30 min at room temperature.

Then the DCPD solution was drained, and the vials and samples were washed with anhydrous dichloromethane. A fresh portion of anhydrous dichloromethane was added into the vials, and the samples were then heated to ~40–50 °C for 5–10 min to allow cross-linking of attached polymer. Samples were washed and dried the same way.

At least one sample per batch was characterized by XPS, and these samples were not used in the photoconductivity decay measurements. The XPS samples were mounted onto the stub and transferred into the glove box load lock through the gate valve, while samples for the photoconductivity decay measurements were placed separately in the open glass vessels and pumped in the antichamber of the glove box for at least 3 hours. Before performing the photoconductivity decay measurements, samples were taken into the glove box and sealed in glass vessels under N_2(g), and then brought out of the glove box for measurements. For overlayer thickness measurements and scanning electron microscopy, samples were mounted onto the XPS stub, characterized by XPS, and then taken out through the atmospheric load lock.

2.4. Surface Characterizations

2.4.1. X-ray Photoelectron Spectroscopy

The XPS experiments were conducted in an M-probe surface spectrometer (VG Instrument) pumped by a CTI Cryogenics-8 cryo pump. Samples could be introduced into the UHV system using either the atmospheric load lock or the glove box load lock. The atmospheric load lock was pumped by a Varian model V80 turbo pump and a Varian model SD-300 mechanical pump, and allowed samples to be introduced into the UHV from air. The glove box load lock was pumped by a Varian model V200 turbo pump and a Varian model SD-300 mechanical pump, and enabled samples to be transferred into the UHV through a gate valve that opened to the N_2(g)-purged glove box. These load locks

were brought to the atmospheric pressure by back-filling with N_2(g), and can be pumped down to approximately 10^{-7} Torr in about 10 min. Samples were mounted on a stainless steel or aluminum stub with screws.

The XPS chamber was maintained at a base pressure of less than 5×10^{-10} Torr, although the operating pressure was 5×10^{-9} to 2×10^{-8} Torr. Monochromatic Al K_α x-rays (hν = 1486.6 eV) incident at 35° from the sample surface were used to excite electrons from the sample, while the emitted electrons were collected by a hemispherical analyzer at a take-off angle of 35° from the plane of the sample surface. Data collection and analysis were done with the M-probe package software version 3.4. Survey scans were collected in the scanned mode with an elliptical spot of dimensions 800 μm × 1200 μm incident on the sample surface. The high-resolution scans were recorded in an unscanned mode with the same spot size. A typical XPS characterization of a surface consisted of one survey scan from 0–700 eV binding energies and a high resolution scan of the Si 2p region (97.57–104.59 eV binding energies). In certain cases when Si 2p peak was very small or undetected, the high-resolution scan was omitted.

2.4.2. Overlayer Thickness Measurements: Ellipsometry and Profilometry

The thicknesses of polymer overlayers formed using different concentrations of norbornene and DCPD were measured by either ellipsometry or profilometry. Ellipsometric measurements were performed on a Gaertner variable angle ellipsometer model L116C using a helium-neon laser (λ = 632.8 nm) and a 45° polarizer, with an incident angle set to 70°. The film thickness was calculated using the software package provided by Gaertner. The index of refraction N_S and the absorption coefficient K_S of the substrate were determined using a freshly etched Si, and these numbers were used as standards when film thicknesses were measured. An indexes of refraction N_F = 1.46 was used for both terminal olefin and polymer layers. Film thickness was measured at six

different locations on each sample, and two measurements were done at each spot. The measured thickness values for all samples were ±1 Å for a particular spot.

Profilometric measurements of several polynorbornene-terminated Si samples polymerized from 0.15M, 0.45 M, and 2.44 M norbornene solution were performed using Sloan Dektak 3030 surface profiling measuring system with a diamond stylus (12.5 μm radius). The stylus force was set to 10 mN, and with the speed set to low, scan length of 4 mm was selected for most measurements. A stainless steel spatula was used to scrape away a thin stripe of the polynorbornene overlayer, and the profile of the surface features was plotted. By measuring the depth of the scribe, the thickness of the polymer was determined.

2.4.3. Scanning Electron Microscopy

Images of polynorbornene overlayers and sample cross section were obtained using Camscan series II scanning electron microscope (SEM). It was equipped with an Everhart-Thornley secondary-electron imaging, a Robinson-type backscattered electron detector for atomic-number-contrast imaging, and a relatively slow speed absorbed current imaging system. An on-board frame averaging system was used to integrate several scan frames in order to reduce noise, and the working resolution of the Camscan was approximately 100 nm. Digital imaging was performed using the 4Pi Systems Scanning Interface Unit for digital beam control, and images were acquired under an operating pressure of 10^{-5} Torr. The acquired digital images were stored in a computer and processed off-line using NIH Image program. Samples with different polynorbornene overlayer thicknesses were prepared using 0.15 M, 0.45 M, and 2.44 M norbornene solutions. The surface uniformity of the polymer layers was examined under a 500× magnification. A cross-sectional SEM image of a sample prepared using 2.44 M norbornene/1,2-dichloroethane solution was also obtained under a 1500× magnification and the polymer thickness was estimated from the image.

Figure 4.2

Experimental approach to produce a variety of covalently attached polymer overlayers on Si surfaces using surface-initiated ring-opening metathesis polymerization method. The structures of two metathesis catalysts used are shown in the box.

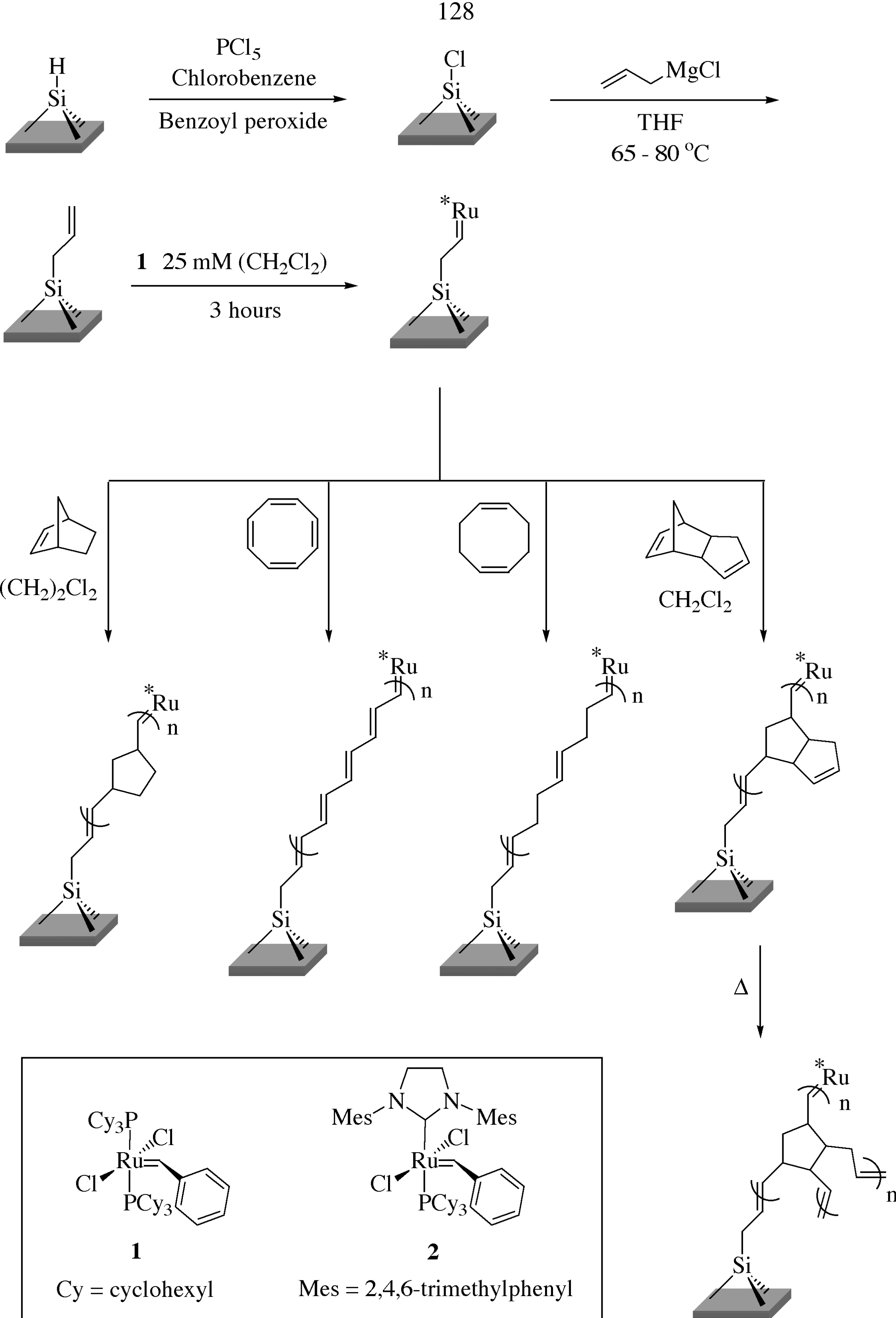
H
Si
PCl5
Chlorobenzene
Benzoyl peroxide
Cl
Si
MgCl
THF
65 - 80 °C
Si
1 25 mM (CH2Cl2)
3 hours
*Ru
Si
(CH2)2Cl2
CH2Cl2
*Ru
n
Si
Δ
m
Cy3P
Cl
Ru
PCy3
1
Cy = cyclohexyl
Mes
N
2
Mes = 2,4,6-trimethylphenyl

Table 4.1

List of reagents and reaction conditions used for each step of the Si surface modification procedure.

Reaction	Reagents	Reaction Time	Reaction Temperature
Chlorination	PCl_5 in chlorobenzene + benzoyl peroxide	45 – 60 min	90 – 100 ˚C
Terminal Olefin Addition[a]	MgCl	8 – 15 hr	65 – 80 ˚C
	MgBr	8 – 15 hr	65 – 80 ˚C
	MgBr	14 – 18 hr	65 – 80 ˚C
	MgBr	16 – 18 hr	65 – 80 ˚C
Catalyst Addition[b]	Ru complex **1**	3 hr	Room Temp.
	Ru complex **2**	3 hr	Room Temp.
Polymerization	Norbornene in 1,2-dichloroethane	30 min	Room Temp.
	(1) DCPD in dichloromethane	30 min	Room Temp.
	(2) Heat treatment in dichloromethane	5 min	40 – 50 ˚C

[a] The solvent used for this reaction was THF, and the approximate Grignard reagent concnetrations were 1–1.5 M.

[b] The solvent used to dissolve Ru complexes was anhydrous dichloromethane.

2.5. Photoconductivity Decay Measurements

A schematic of the contactless radio frequency (rf) conductivity apparatus used to measure photoconductivity decays is shown in Figure 4.3. In this system, the rf output from a high-frequency generator (Wavetek 2500A) operating at 450 MHz was connected to a power splitter (Mini-Circuits ZSC2-1W). One output from the power splitter was connected through an amplifier (ANZAC AM-147, +17 dB gain) and a phase-shifter (General Radio 847-LTL) to the local oscillator input of a double-balanced frequency mixer (Mini Circuits ZAY-2), and was used as a reference rf signal. The other output from the power splitter was connected through an amplifier (Mini-Circuits ZHL-1A, +20 dB gain) to the coupled port of a directional coupler (Merrimac CR-20-500, 20 dB isolation). An inductor-capacitor (LC) circuit consisting of a variable coupling capacitor (1-11 pF, air gap), a variable matching capacitor (1-11 pF, quartz), and a three-turn coil (Cu wire, 1.1 mm diameter) placed in close proximity to the sample, was connected to the input port of the directional coupler. The output port of the directional coupler was then connected through an attenuator (Kay 0/400A, 0 to –13 dB) to the reference oscillator port of the double-balanced frequency mixer. The output of the double-balanced frequency mixer was connected to a digital oscilloscope (Tektronix TDS-210) for the measurement of the photoconductivity decay signals.

Prior to a measurement, the LC circuit was tuned to the resonant frequency of the sample by adjusting the variable capacitors and monitoring the amplitude of the reflected rf signals on a separate high-frequency digital oscilloscope (Tektronix TDS-680c). A Spectra-Physics INDI-30 Nd:yttrium–aluminum–garnet laser (1064 nm) operating at a repetition rate of 10 Hz was used to illuminate samples with 10 ns pulses. The power density of the laser beam was attenuated using a beam splitter and neutral density filters (Hoya Optics), and the beam was expanded to approximately 2 cm^2 using a beam expander (Gallilean). A spatially uniform beam profile was produced by placing a

holographic diffuser (Coherent, 1°) directly above the sample. The measurements were obtained under high-level injection conditions by adjusting the power density of the expanded incident beam to ~1×10^{-3} mJ pulse^{-1} using neutral density filters. The incident beam power was determined using a power meter (Coherent Fieldmaster GS) equipped with a pyroeletric sensor (Coherent LM-P10i). The intensity of the light pulse at high-level injection was sufficient to eliminate equilibrium potential drop that might exist in the solid. Therefore imply that the changes in the observe carrier recombination lifetime are primarily due to changes in surface state density and/or the carrier-capture rate constants by surface traps. The sample was placed in a seal glass vessel which allows the sample to be in contact with either air or N_2(g) during the period of measurement. Time constants were obtained by fitting the average of 128 decays to a single exponential and averaging over a minimum of three samples for each type of surface and storage condition.

Time-resolved photoconductivity decays of six types of surfaces stored in a controlled environment at 21 °C and 7% relative humidity (R.H.) were recorded. In addition, three types of surfaces were subjected to a harsher environment at 40 °C and 80–90% R.H., and the effects on the photoconductivity decays were studied over a period of one month. The initial measurement for each type of surface was performed immediately after samples, sealed in the glass vessels under N_2(g), were taken out of the glove box. Then the glass vessels were opened to the air and the samples were stored under one of the two controlled environmental conditions.

The 21 °C/7% R.H. environmental chamber was made by feeding a constant flow of house air into a desiccator cabinet. An in-line oil-removal coalescing filter (Parker) in conjunction with a microalescer filter (Wilkerson) was used to remove oil droplets and vapor from the house air. Figure 4.4 displays the setup of the 40 °C/80–90% R.H. environmental chamber. The filtered house air was first split into two paths, and two Bel-Art Riteflow flowmeters were used to control the amount of air going through each

path. One path directed the air through a custom-made bubbler filled with deionized water (kept at ~45 °C) to allow saturation of water vapor, and then passed through a heat-exchange Cu coil immersed in a 45 °C constant-temperature bath/circulator (National Instrument Type SCI). The warmed water-vapor-saturated air was then combined with dry house air from the other path to create 80–90% R.H. and was introduced into a insulated chamber where the samples were stored. The warm water in the constant-temperature bath/circulator was also circulated through the outside jacket of the bubbler, and another heat-exchange Cu coil inside the insulated chamber designed to keep the air temperature at 40 °C. Samples were placed in separate test tubes while being stored in the 40 °C/80–90% R.H. chamber, and in plastic dishes if stored in the 21 °C/7% R.H. chamber. The relative humidity of each chamber was measured by a hygrometer (Control Company).

Figure 4.3

A schematic of the radio frequency (rf) apparatus used to perform photoconductivity decay measurements. The splitter separates the rf into reflected and reference signals. The imbalance in the circuit caused by the sample is phase detected by a double-balance frequency-mixer and then digitized. The attenuator in the reference branch of the circuit was bypassed in these experiments. The excess carriers generated by the light pulse injection cause an increase in electrical conductivity in the sample. The conductivity then decreases when these excess carriers recombine. The change in conductivity can be monitored by rf reflectance measurement, and the value of charge-carrier recombination lifetime can be obtained by analyzing the transient of the reflected rf power.

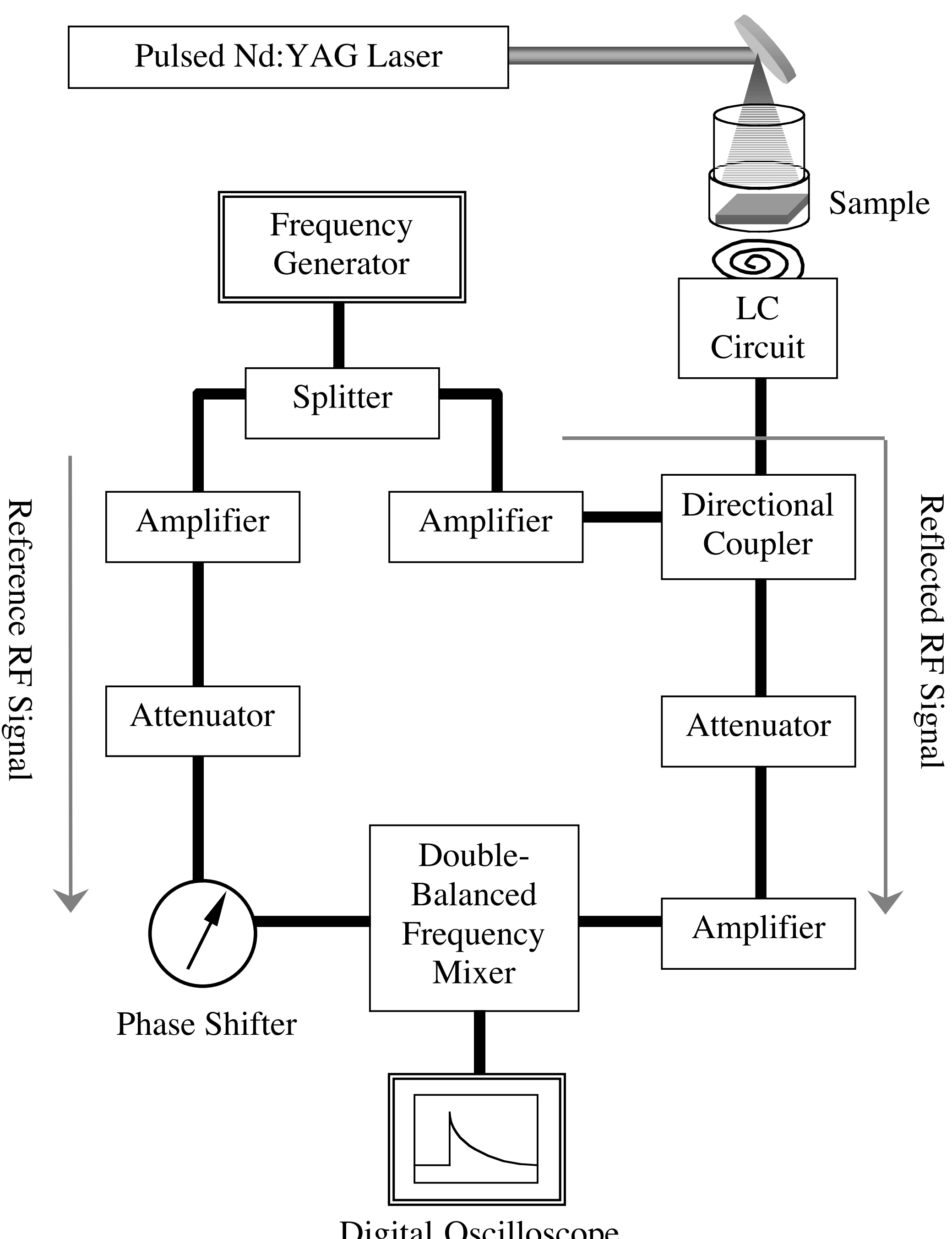

Pulsed Nd:YAG Laser
Sample
Frequency Generator
LC Circuit
Splitter
Reference RF Signal
Amplifier
Amplifier
Directional Coupler
Reflected RF Signal
Attenuator
Attenuator
Double-Balanced Frequency Mixer
Amplifier
Phase Shifter
Digital Oscilloscope

Figure 4.4

(a) A schematic of the controlled-environment chamber for sample storage under an elevated temperature and relative humidity condition. Filtered house air is split into two paths; one path is designed to saturate the air with water vapor at 45 °C, and the other path delivers original dry filtered house air. With the aid of flowmeters, two paths were then combined to create an environment with an air temperature of 40 °C and 80–90% relative humidity. (b) A photograph of the controlled-environment setup. (c) A detailed photograph showing the interior of the chamber. The 45 °C water was circulated through the Cu tubing to provide heating inside the chamber. The test tubes were used to hold the samples being stored.

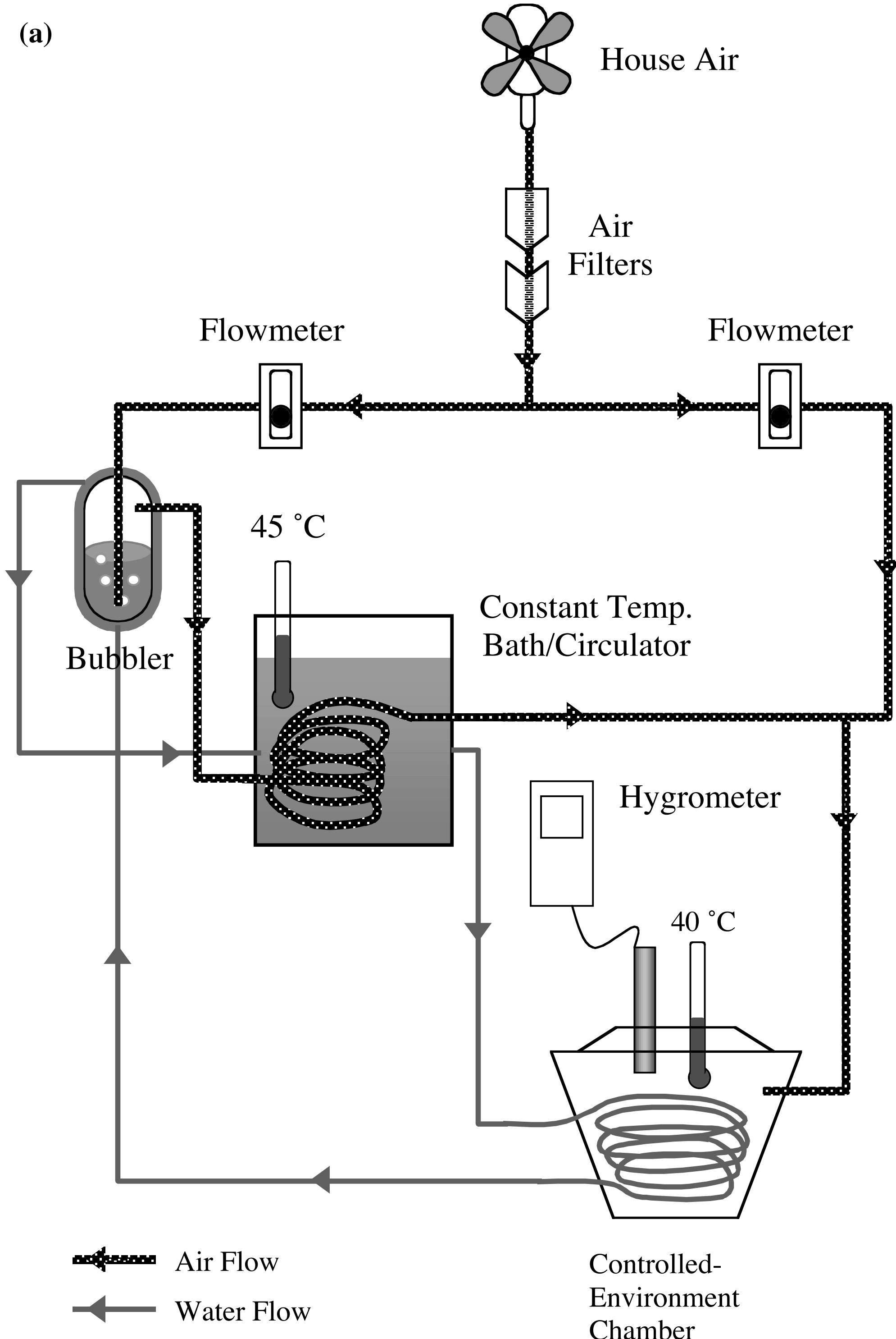
(a)
House Air
Air
Filters
Flowmeter
Flowmeter
45 ˚C
Constant Temp.
Bath/Circulator
Bubbler
Hygrometer
40 ˚C
Air Flow
Water Flow
Controlled-
Environment
Chamber

(b)

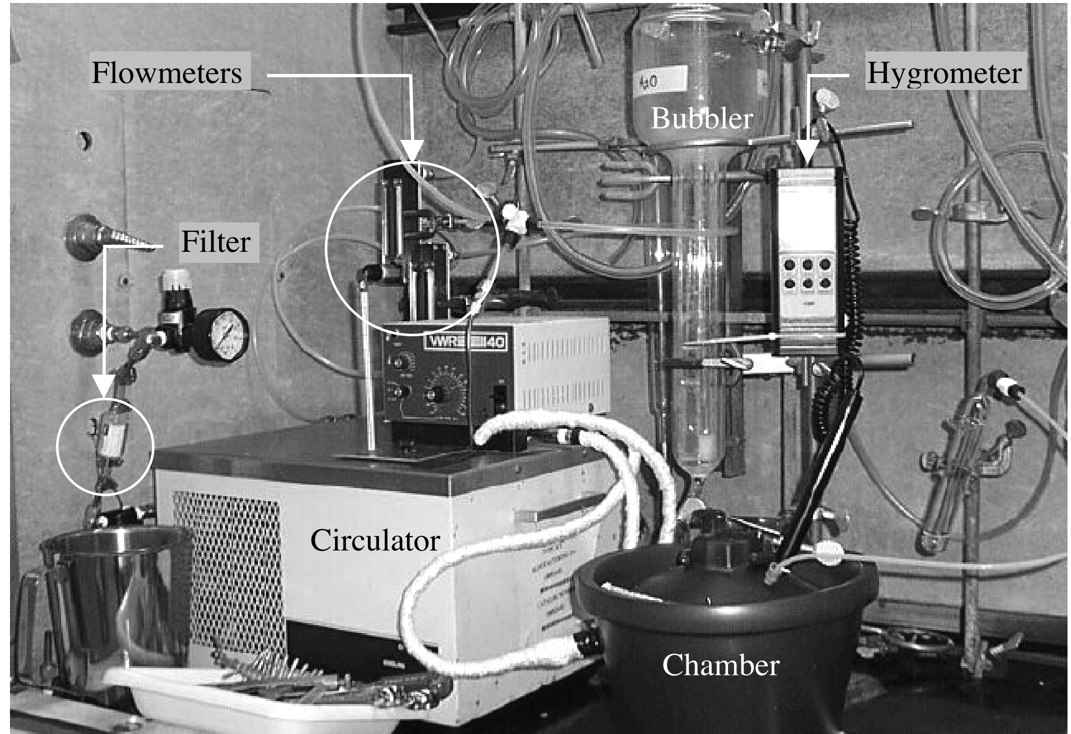

(c)

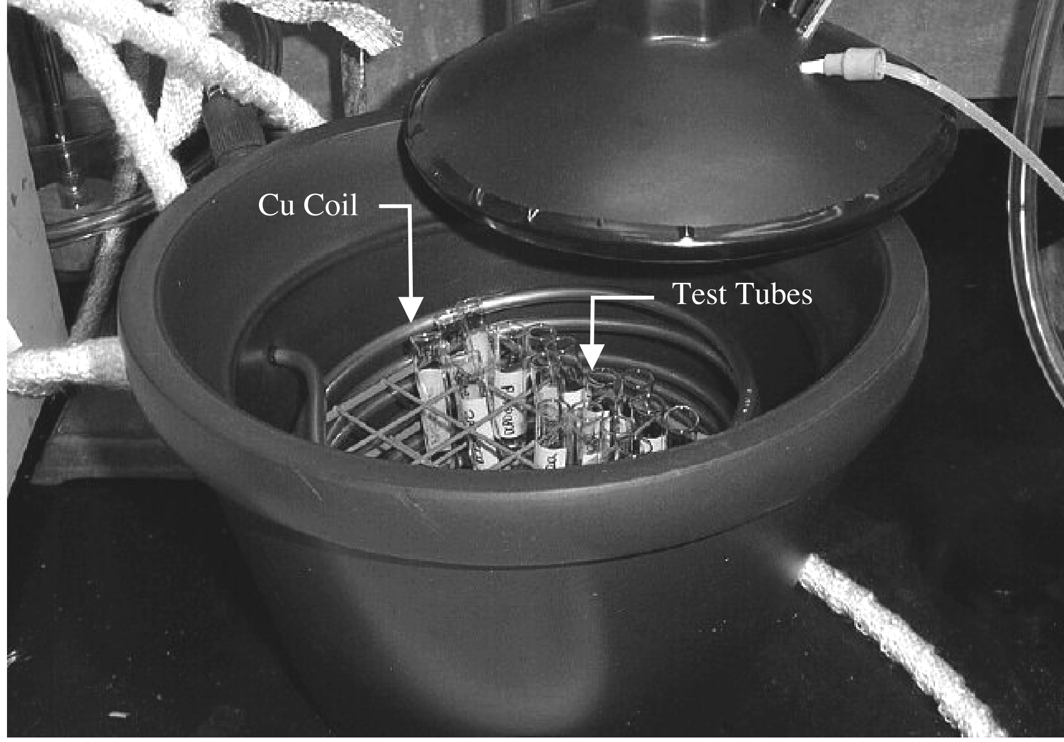

3. Results

3.1. Surface Modifications

Four monomers were used for the modification of Si(111) surfaces using ring-opening metathesis polymerization (ROMP) method. The x-ray photoelectron spectroscopy (XPS) results suggest that both norbornene and dicyclopentadiene (DCPD) were successfully polymerized on the Si surfaces, but surface-initiated ROMP did not produce detectable polymer overlayers with either cyclooctadiene (COD) or cyclooctatetraene (COT) monomer.

The surface modification process was monitored and verified using XPS. Figure 4.5 displays the XP spectra obtained at each step of the surface modification process. A successful etching procedure produces an H-terminated Si surface with a clean spectrum showing large Si 2p and Si 2s peaks at 99 eV and 149 eV binding energies. The smaller peaks present at successive intervals of 17.5 eV binding energy higher than the main Si 2p and 2s peaks were plasmon loss peaks, and were characteristic of Si surfaces.[49,50] Small signals due to adventitious carbon and oxygen were often observed at 284.6 eV (C 1s) and 532 eV (O 1s). The presence of adventitious carbonaceous material on the silicon surface was a result of wet chemical etching and subsequent brief handling of samples in air.[51,52] The lack of signal in the 101 to 104 eV region of the Si 2p high-resolution XP spectra collected with each survey scans suggested that the oxygen signal observed in survey spectra was not due to silicon oxide.

Figure 4.5b shows the representative spectrum of a chlorinated Si surface. Addition peaks were observed at 270 eV and 200 eV binding energies, which correspond to Cl 2s and Cl 2p peaks.[43] Attachment of the terminal olefin was confirmed by the disappearance of the Cl peaks and the concomitant increase in magnitude of the C 1s

peak in the XP survey spectrum (Figure 4.5c). However, a direct evidence of the attachment of Ru catalyst could not be confirmed using XPS data (Figure 4.5d). The subsequent growth of polymer film and a set of control experiments offered indirect but convincing confirmations of the catalyst addition reaction.

3.1.1. Polynorbornene-Terminated Si

For most polynorbornene films, growth of polymer was evidenced by the disappearance of the Si signals and the formation of an overlayer that only displayed C peaks in the XP survey scan (Figure 4.5e). When a low concentration (<0.09 M) norbornene solution was used for polymerization, the observed survey spectrum displayed an increase in magnitude of the C 1s peak while the magnitude of the Si peaks were decreased but still visible. The surfaces of polynorbornene-terminated Si made with higher concentration (2.44 M) norbornene solutions appeared colorful and the films were thick enough to be visible by the naked eyes. Both C3 olefin- and C5 olefin-polynorbornene-terminated Si surfaces were successfully made.

3.1.2. PolyDCPD-Terminated Si

The ROMP of DCPD was monitored using XPS in the same fashion as described. Figure 4.6 displays the XPS survey spectra of polyDCPD-terminated Si surfaces made from four different DCPD concentrations (0.27 M, 0.45 M, 0.98 M, and 2.5 M in dichloromethane). The ROMP of DCPD did not produce polymer films of the same thickness as seen with norbornene. Although the ring-strains of norbornenes and DCPDs are very similar, the larger size of a DCPD monomer unit could hinder monomer diffusion to the surface-bound Ru initiator and thus limit the film thickness. However, the film thickness could still be controlled by the monomer concentrations as evidenced by XPS analysis. When polymerized DCPD is subject to heat (~40–50 ˚C) the remaining cyclic olefins are expected to undergo ring-opening polymerization and cross-link with

neighboring olefins. Although the cross-linking property of polyDCPD on surfaces was not investigated in this work, considering that the surface-bound polyDCPD chains are immobilized, the extent of cross-linkage could be somewhat limited.

3.1.3. ROMP of COD and COT

Attempts to produce polyCOD- and polyCOT (polyacetylene)-terminated surfaces were unsuccessful. The XP spectra showed no polymer formation on the Si surfaces following either immersion of **1**-modified Si into COD or immersion of **2**-modified Si into COT. Since COT is less strained than norbornene and COD, a more powerful Ru catalyst **2** was used in place of **1** to initiate the ROMP reaction. The XP survey spectrum shows no significant increase in the magnitude of C 1s peak. To be certain that the catalyst **2** would initiate ROMP on a surface in a similar fashion as the catalyst **1**, it was used to polymerize norbornene (2.44 M in 1,2-dichloroethane). The resulting XP spectrum revealed a large C 1s peak and no detectable Si peaks, and a colorful film was seen on the surface as observed when norbornene was polymerized using catalyst **1**. Thus, surface bound **2** was successful at polymerize norbornene.

3.1.4. Control Experiments

Additional experiments were performed to establish that (i) the polymerization of norbornene was directly initiated by **1**, and (ii) the resulting polymer film was attached covalently to the Si surface. When an olefin-terminated Si substrate was exposed to a solution of norbornene, no polymer was observed by XPS (Figure 4.7a). In addition, when an H-terminated Si surface was exposed to a solution of norbornene, no polymer formed and the XPS signals showed only Si and a very small amount of adventitious C and O (Figure 4.7b). Exposure of an H-terminated Si surface to a solution of **1** followed by exposure to a solution of norbornene produced a polymer that did not persist on the Si surface after washing with dichloromethane (Figure 4.7c). These wet chemical

experiments imply that the technique described in this chapter did in fact produce covalently attached polymeric films on the Si surface, and the polymerization could not occur without the Ru initiators.

Figure 4.5

XP survey spectra of (a) H-terminated Si, (b) Cl-terminated Si, (c) allyl-terminated Si, (d) allyl-terminated Si after immersing in a solution of **1** for 3 hours, and (e) covalently attached polynorbornene on Si. Spectra in (a)–(d) were normalized relative to the intensity of the Si 2p peak. Typical Si 2p:C 1s:O 1s peak ratios were (a) 1:(0.35 ± 0.06):(0.36 ± 0.09), (b) 1:(0.54 ± 0.03):(0.39 ± 0.04) (average of 2 spectra), (c) 1:(0.82 ± 0.22):(0.68 ± 0.22), and (d) 1:(2.04 ± 0.26):(0.46 ± 0.12) (average of 2 spectra).

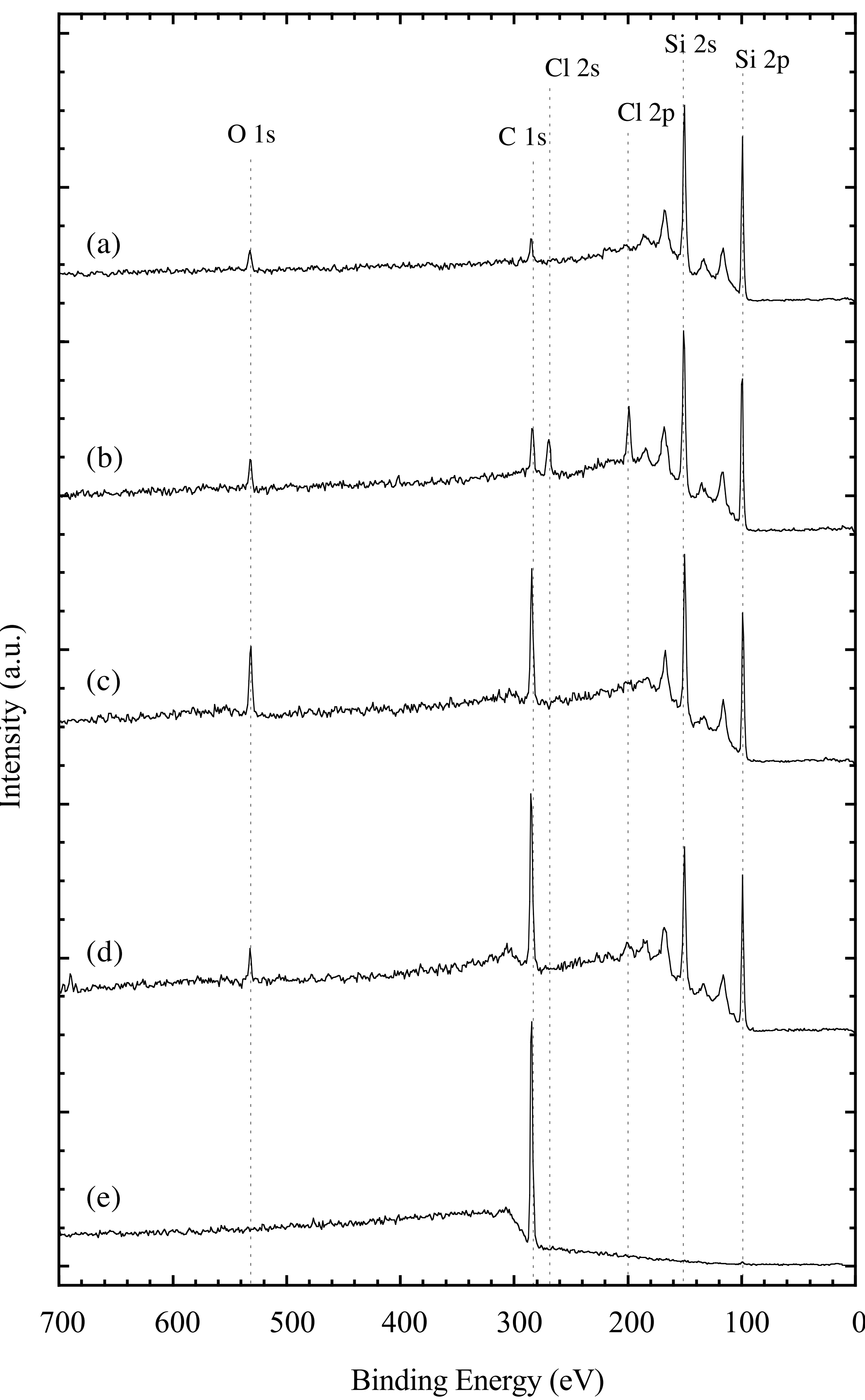
O 1s
C 1s
Cl 2s
Cl 2p
Si 2s
Si 2p
(a)
(b)
(c)
(d)
(e)
Intensity (a.u.)
700
600
500
400
300
200
100
0
Binding Energy (eV)

Figure 4.6

XP survey spectra of polyDCPD-terminated Si made from solutions of (a) 0.27 M, (b) 0.45 M, (c) 0.98 M, and (d) 2.5 M DCPD in dichloromethane. All spectra were normalized relative to the intensity of the Si 2p peak.

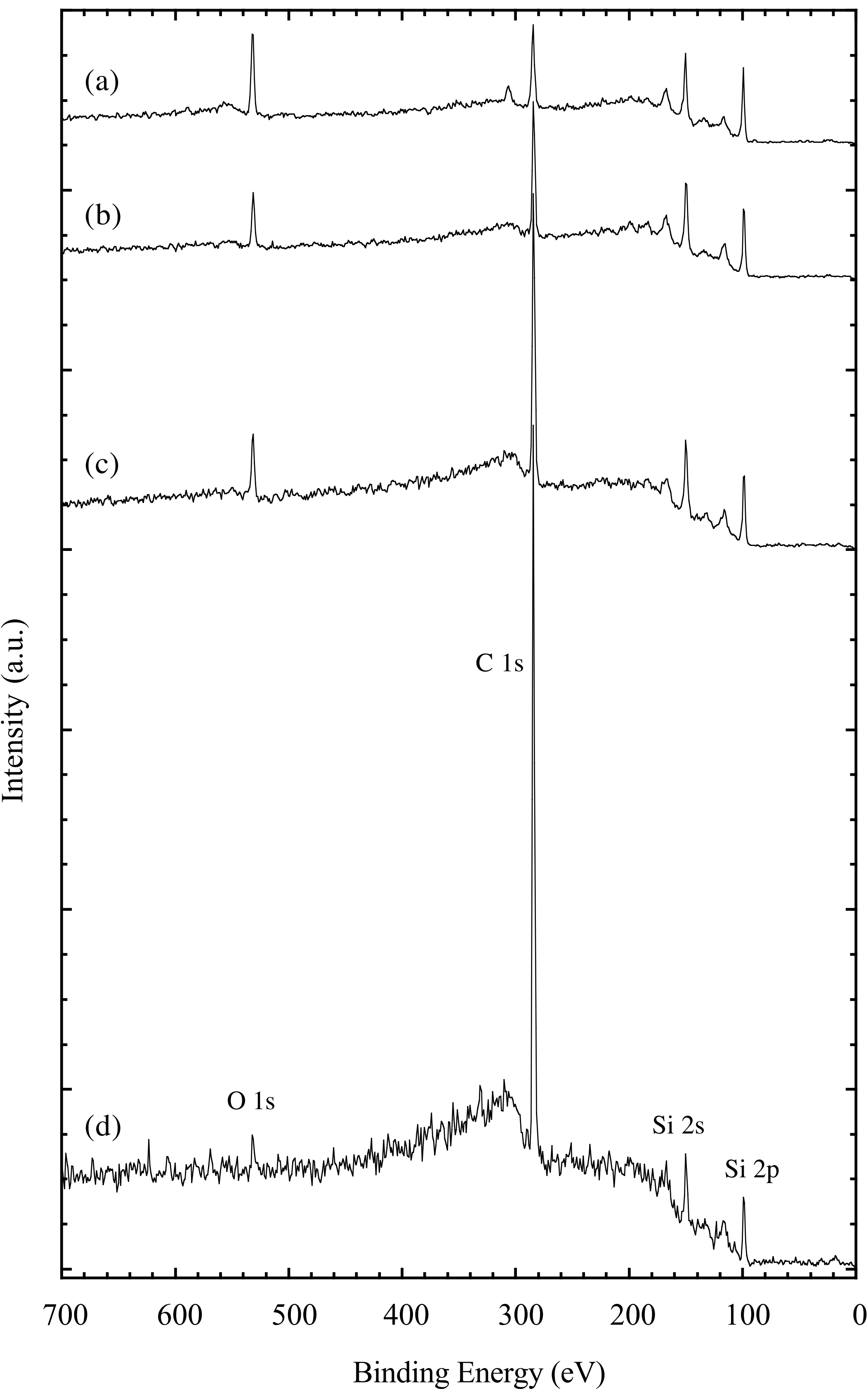
(a)
(b)
(c)
(d)
C 1s
O 1s
Si 2s
Si 2p
Intensity (a.u.)
700
600
500
400
300
200
100
0
Binding Energy (eV)

Figure 4.7

XP survey spectra of (a) C4 olefin-terminated Si following immersion in norbornene (2.44 M in 1,2-dichloroethane) for 30 min, (b) H-terminated Si following immersion in the same norbornene solution for 30 min, and (c) H-terminated Si after being immersed in a solution of **1** and then norbornene. All surfaces were rinsed with anhydrous dichloromethane after each immersion. All spectra were normalized relative to the intensity of the Si 2p peak. Compare to the spectrum of a polynorbornene-terminated Si (Figure 4.5e), spectra (a)–(c) indicated no significant polymer growth after these surface treatments.

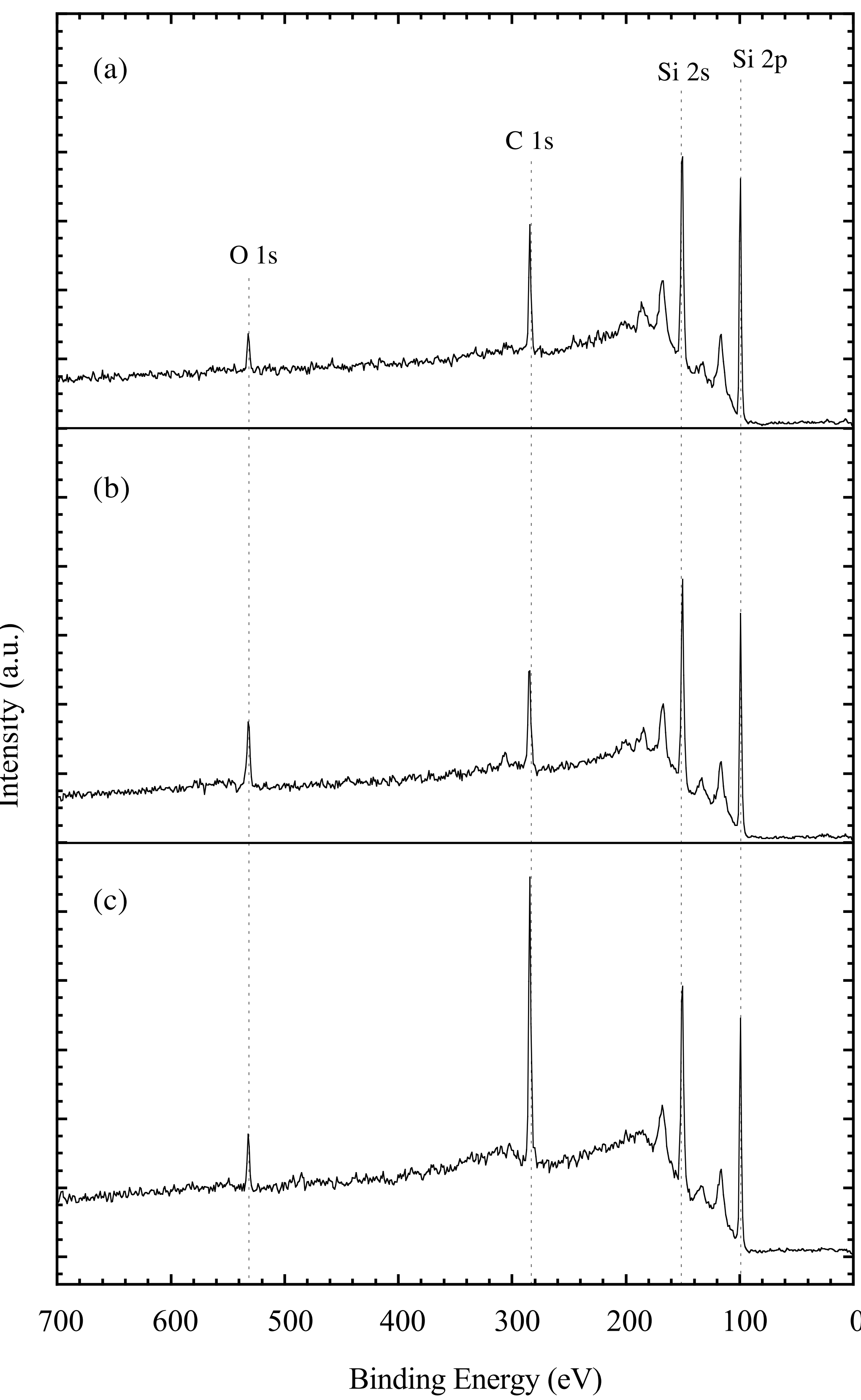
(a)
(b)
(c)
O 1s
C 1s
Si 2s
Si 2p
Intensity (a.u.)
Binding Energy (eV)
700
600
500
400
300
200
100
0

3.2. Surface Characterizations

3.2.1. Polymer Thickness Measurements

Because ROMP initiated by **1** is a controlled polymerization process,[53,54] different film thicknesses could be obtained by varying the concentration of monomer solutions. Table 4.2 summarizes the thicknesses of several polynorbornene films produced at a fixed reaction time (30 min) in response to variation in the concentration of monomer in the solution. The standard deviation in the ellipsometrically derived thickness measured at several different spots for each sample was usually less than ±10% of the mean thickness value, indicating that the polymer film covered the entire Si substrate. Figure 4.8a displays a partial surface profile of a polynorbornene-terminated Si made from a 2.44 M norbornene solution. This profile includes a feature representing the area of a spatula scrape as shown in the SEM image of the same sample (see Figure 4.8b). The upward spikes at the edges of the feature are most likely the result of polymer being pushed and piled up to the sides when the spatula was used to scraped off small amount of polymer on the surface. The center parts of these features are very flat and smooth, which is a good indication of that being the flat surface of a Si substrate. The measured profilometric thicknesses of both 0.15 M and 0.45 M polynorbornene films were consistent with the ellipsometric data (Table 4.2). The polymer films formed using a 2.44 M solution were too thick for ellipsometric measurements, therefore only the profilometric result is reported.

3.2.2. Scanning Electron Microscopy

Figure 4.9 shows two top-view images of polynorbornene-terminated Si samples ([norbornene] = 0.15 M and 2.44 M) at 500× magnification. A thinner polynorbornene overlayer appears to be smoother compared to a thicker overlayer at the same

magnification. This observation is consistent with the polymer thickness measurements displaying larger standard deviation values when thicker polymer films were grown. Figure 4.10 displays a SEM image of the cross section of a sample (obtained after immersion of a **1**-treated, allyl-terminated Si sample into a 2.44 M solution of norbornene in 1,2-dichloroethane for 30 min) at 1500× magnification. A film thickness of 5.3 ± 0.2 μm over a distance of 75 μm was measured from this micrograph. The SEM images also indicate that the Si substrates were indeed covered entirely by polynorbornene. The estimated thickness of the polymer film from SEM images of two samples at 1500× magnification is 5.6 ± 0.06 μm, which agrees with the thickness of 5.39 ± 0.14 μm measured using profilometry.

Table 4.2

Dependence of the polymer overlayer thickness on the concentration of norbornene in the solution.

[Norbornene] (M)	Thickness[a] (Å)	Number of Samples	Number of Spots Per Sample
0.01	9 ± 2	4	6
0.05	83 ± 65	2	7
0.09	119 ± 16	4	6
0.15	297 ± 40	2	7
0.18	374 ± 130	6	5
0.27	1130 ± 38	5	6
0.45	2230 ± 410	2	7
2.44	53920 ± 1420[b]	1	2

[a] Each thickness value is an average of measurements on the corresponding number of samples, with the reported number of spots measured on each sample. The standard deviation between measurements at different locations of one sample was usually less than ±10% of the mean film thickness value of that sample; therefore the quoted standard deviation in this table only reflects the differences in polymer overlayer thickness between different samples or different experimental trials.

[b] The thickness data of this sample was acquired using profilometry.

Figure 4.8

(a) A partial surface profile of a polynorbornene-terminated Si surface obtained through profilometry. The polymer overlayer was grown using 2.44 M norbornene solution. By scraping a thin strip of polymer off the substrate and running the stylus of a profilometer across the scratch, the height of examined surface was plotted and the thickness of the overlayer could be determined from the height difference between the bottom of the feature and the surrounding polymer layer. The surface feature plotted corresponds to one of the spatula scraps shown in (b), which is a SEM image of the same surface at 30× magnification. The spatula scratches revealed the bare surface of the Si substrate.

(a)

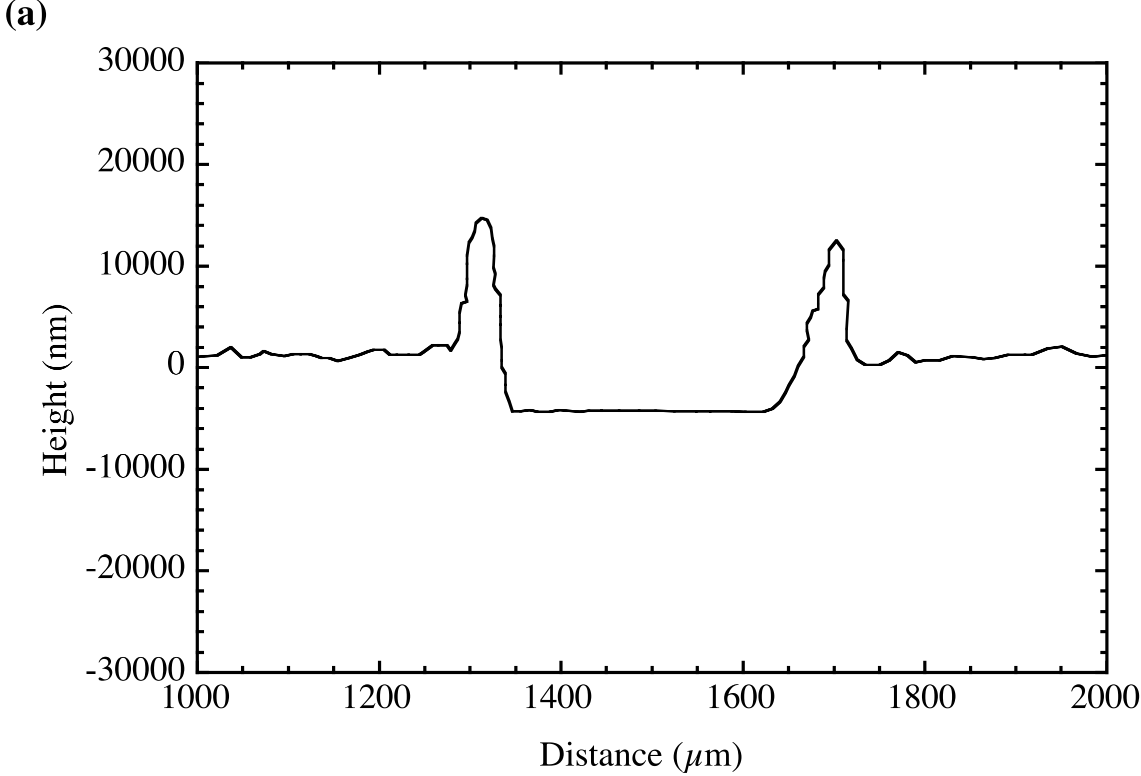

(b)

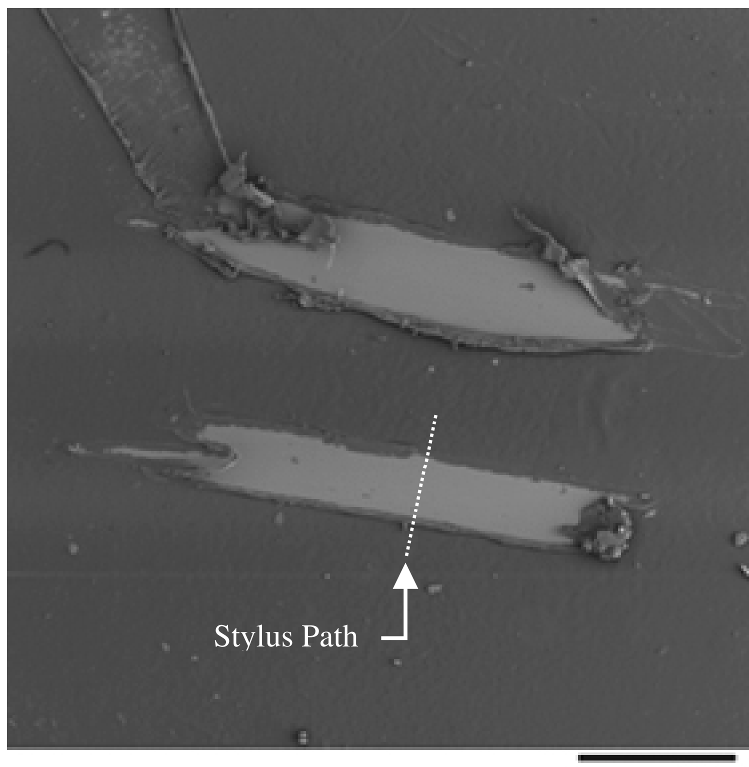

Figure 4.9

SEM top-view images of two polynorbornene-terminated Si surfaces made from (a) 0.15 M and (b) 2.44 M norbornene/1,2-dichloroethane solutions. The overlayer thicknesses of two samples were 271 ± 20 Å and 53920 ± 1420 Å, respectively. The samples with thicker polymer overlayers were found to have larger standard deviations in their thickness measurements, which can be explained by the SEM image showing a rougher surface for a thicker overlayer under the same magnification.

(a)

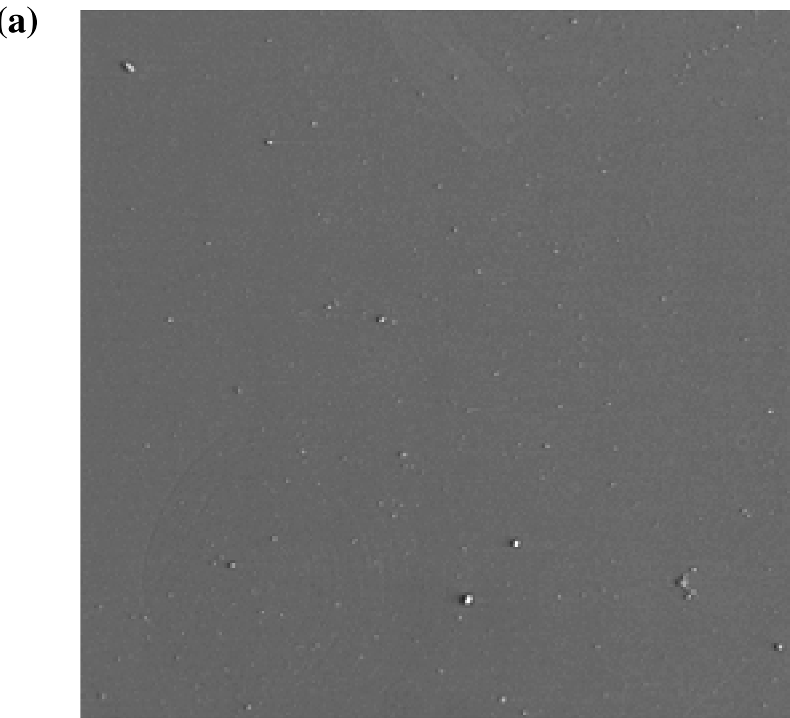

(b)

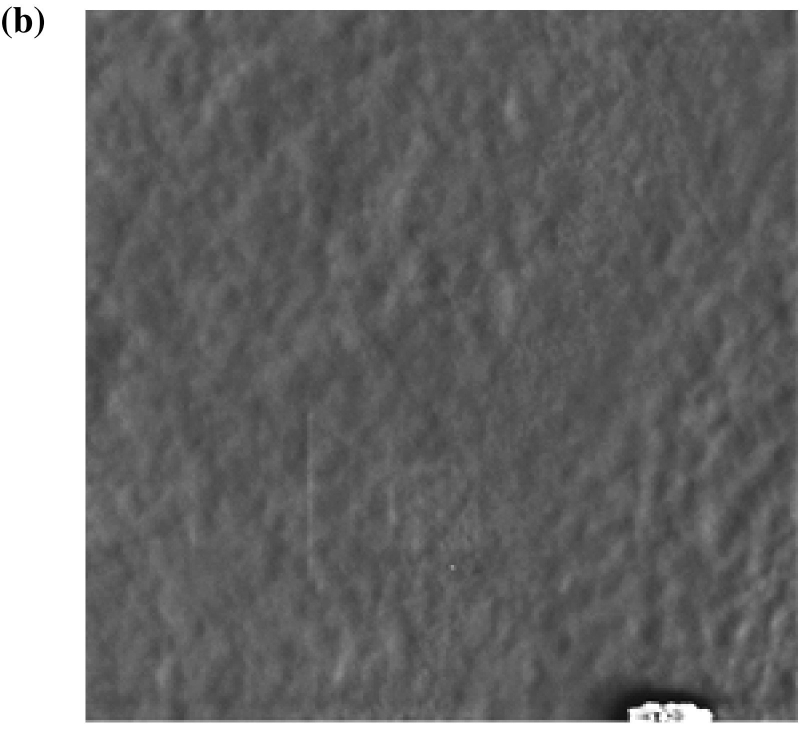

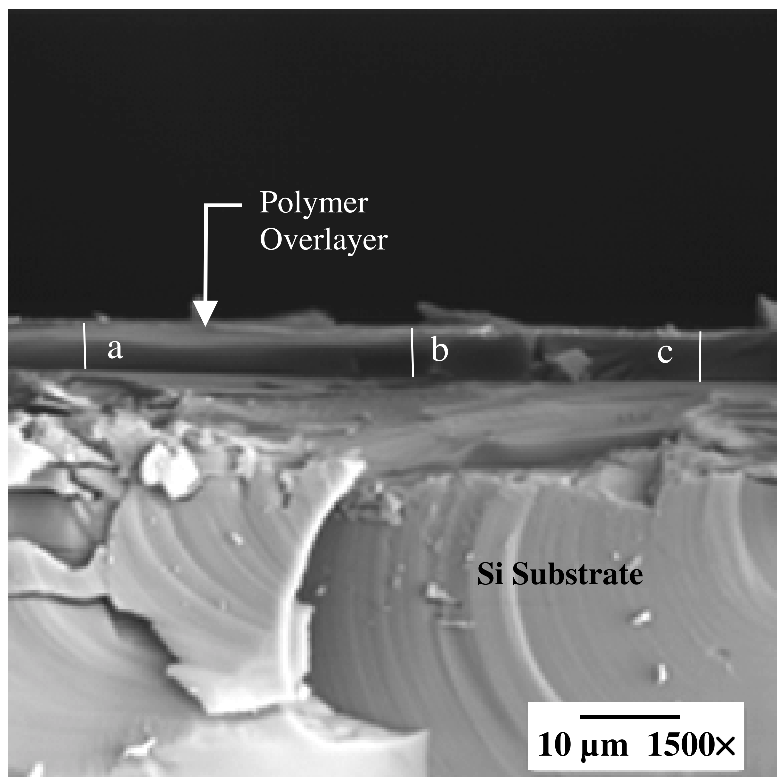

Figure 4.10

A cross-sectional SEM image of a polynorbornene-covered Si surface at 1500× magnification. The polymer film covered the entire Si substrate, and the estimated film thicknesses at points a, b, and c from the SEM image are 5.0, 5.5, and 5.4 μm, respectively. These values are in good agreement with the mean polymer thickness of 5.39 ± 0.14 μm that was determined for the same sample using profilometry.

3.3. Photoconductivity Decay Measurements

Time-resolved photoconductivity decay curves of various surfaces are included in the following sections. Each shown curve is the average of 128 decays, and is fit by a single exponential to extract the time constant for carrier recombination. The observed lifetime τ can be related to the bulk lifetime τ_b and the surface recombination velocity S through this equation:[55-57]

$$\frac{1}{\tau} = \frac{1}{\tau_b} + \frac{2S}{d} \tag{4.1}$$

where d is the sample thickness. The S reported in this chapter were calculated assuming that the experimentally observed lifetime is dominated by surface recombination with no contribution from charge-carrier recombination in the bulk ($\tau_b = \infty$); therefore, it is important to note that the reported S values represent the upper limit to the true S values.

3.3.1. C3 Olefin-Terminated and C3 Olefin-Polymer-Terminated Si Surfaces

Figure 4.11 displays the transient photoconductivity decay behaviors of C3 olefin-terminated, C3 olefin-polynorbornene-terminated, and C3 olefin-polyDCPD-terminated Si surfaces in an N_2(g) ambient. The initial photoconductivity decays of C3-olefin-modified Si surfaces were relatively slow, with a mean charge-carrier lifetime of 250 ± 60 μs. When a C3 olefin-terminated surface was further modified with either polynorbornene or polyDCPD, the mean charge-carrier lifetime decreased to 230 ± 90 μs and 170 ± 10 μs, respectively. The initial S values of these three surfaces were calculated using Equation 4.1. Assuming an infinite bulk lifetime and d = 294 μm, the upper bound S values were determined to be 59 ± 10 cm s^{-1}, 64 ± 20 cm s^{-1}, and 88 ± 3 cm s^{-1}, respectively.

Figure 4.12 shows the time-dependent mean carrier lifetimes of all three surfaces in air (21 °C and 7% R.H.). The Si surfaces modified with C3 olefin were not able to preserve the initial surface quality and the lifetime value dropped very quickly following the air exposure. Furthermore, the polymer overlayers were found to be ineffective in protecting the Si surfaces after the C3 olefin layers had failed, and the mean lifetimes of both polynorbornene- and polyDCPD-modified surfaces also decreased, though not as quickly as the C3 olefin-terminated Si. Within 5 hours after the C3 olefin-terminated samples were exposed to the air, the mean lifetime had already exhibited a fivefold decrease to <50 μs. Within 30 hours of the air exposure, the mean carrier lifetimes of polymer-terminated surfaces had also dropped to about 50 μs. After being exposed to the air for 120 hours, C3 olefin- and C3 olefin-polyDCPD-terminated surfaces were found to have S values of 1600 ± 500 cm s^{-1} and 610 ± 40 cm s^{-1}. The degradation of the lifetime for a C3 olefin-terminated surface was very similar to that of an unmodified Si–H surface in air. Although the polymer overlayers added some protection to the C3 olefin-modified surfaces, a more effective olefin linker could improve the charge-carrier lifetime at the modified Si/air interface.

The mean carrier lifetimes of three different C3 olefin-polynorbornene overlayer thicknesses were also investigated to determine the optimal polymer thickness that worked the best to preserve the modified surfaces after exposure to the air. Although the thicker polymer layer was expected to be a better barrier against oxidation of the Si surface which leads to an increased surface defects, no such trend was observed when the time-dependent S of samples made using 0.09 M, 0.18 M, and 0.27 M norbornene solutions were plotted. For following experiments, polynorbornene overlayers made from a 0.27 M solution were used unless otherwise stated.

3.3.2. Effects of Olefin Linker Chain Length

Several terminal olefin linkers were investigated for the purpose of finding the one that is capable of generating well-preserved surfaces for further modification steps. Figure 4.13 displays the time dependence of the mean carrier lifetimes of Si surfaces modified with mixed methyl/allyl (50%:50%, C1/C3 olefin), C3 olefin, C5 olefin, and C6 olefin linkers. With a suspicion that C3 olefin did not provide enough surface coverage to prevent the oxidation of Si substrate, an olefin layer of better surface coverage was desired for improving the charge-carrier lifetime of modified Si. Since methyl groups are small enough to bind to neighboring Si atoms on the surface,[58] and may be able to fill in the pinholes created by C3 olefin modification, methyl Grignard was mixed in with allyl Grignard to generate mixed C1/C3 olefin-terminated surfaces. However, this mixed linker was not able to preserve the carrier lifetime, and the *S* value of this surface following 90 hour of air exposure was almost as high as that of an unmodified Si–H and a C3 olefin-terminated surfaces in air, though the rate of the lifetime degradation was slower for this type of surfaces.

Longer terminal olefin linkers are more flexible and the tilted chains might be able to cover the surface better. When C6 olefin-terminated Si was found to have a stable carrier lifetime after 120 hours of air exposure, C5 olefin-terminated surfaces were also tested. Interestingly, the C5 olefin termination not only had a stable lifetime, but it also exhibited a longer carrier lifetime. The C5 olefin was therefore used as a linker for all further surface modifications.

3.3.3. C5 Olefin-Terminated and C5 Olefin-Polymer-Terminated Si Surfaces

Figure 4.14 displays the transient photoconductivity decay behaviors of C5 olefin-terminated, C5 olefin-polynorbornene-terminated, and C5 olefin-polyDCPD-terminated Si surfaces in an N_2(g) ambient. The initial photoconductivity decays of C5-

olefin- modified Si surfaces yielded a mean charge-carrier lifetime of 360 ± 10 μs. Further modification with either polynorbornene or polyDCPD produced surfaces with mean carrier lifetimes of 200 ± 30 μs and 190 ± 110 μs, which are comparable with the C5 olefin-polymer modified surfaces. The initial S values of these three surfaces were calculated using Equation 4.1. Assuming an infinite bulk lifetime and d = 294 μm, the upper bound S values were determined to be 41 ± 1 cm s^{-1}, 75 ± 10 cm s^{-1}, and 76 ± 50 cm s^{-1}, respectively.

Figure 4.15 plots the time dependence of the carrier lifetime of each surface in air under different temperature/humidity conditions. Although the carrier lifetime of C5 olefin-terminated Si was very high initially, it was decreasing very slowly over the course of 700 hours, and the lifetime drop was slightly more pronounced for samples stored under the 40 °C/80–90% R.H. condition (Figure 4.15a). On the other hand, the carrier lifetimes of both C5 olefin-polynorbornene- and C5 olefin-polyDCPD- terminated surfaces were not affected by the storage condition, and the surfaces recombination velocities remained low after almost one month of air exposure.

Figure 4.16 shows the time-dependent mean carrier lifetimes of all three surfaces in air (21 °C and 7% R.H.); after prolong exposure of these surfaces in air, all still exhibited low surface recombination velocities. Following 650 hours of air exposure, the S values were found to be 49 ± 7 cm s^{-1}, 61 ± 10 cm s^{-1}, and 66 ± 10 cm s^{-1} for C5 olefin-terminated, C5 olefin-polynorbornene-terminated, and C5 olefin-polyDCPD-terminated Si surfaces, respectively. The capability for C5 olefin-polymer-terminated surfaces to reserve the initial low surface-defect-density of the modified Si surfaces in N_2(g) was confirmed.

Figure 4.17 displays the time-dependent mean carrier lifetimes of all three surfaces in air under an elevated temperature and humidity environment (40 °C and 80–90% R.H.). Again, after prolonged exposure of these surfaces in air, all still exhibited low surface recombination velocities. Following 600 hours of air exposure, the S values

were found to be 70 ± 30 cm s^{-1}, 51 ± 8 cm s^{-1}, and 59 ± 10 cm s^{-1} for C5 olefin-terminated, C5 olefin-polynorbornene-terminated, and C5 olefin-polyDCPD-terminated Si surfaces, respectively. Although the mean carrier lifetime of the C5 olefin surfaces has decreased slightly after 600 hours of air exposure, it was still comparable with the lifetimes of both polymer-terminated Si. The time-dependent carrier lifetime and surface recombination velocity data are summarized in Table 4.3.

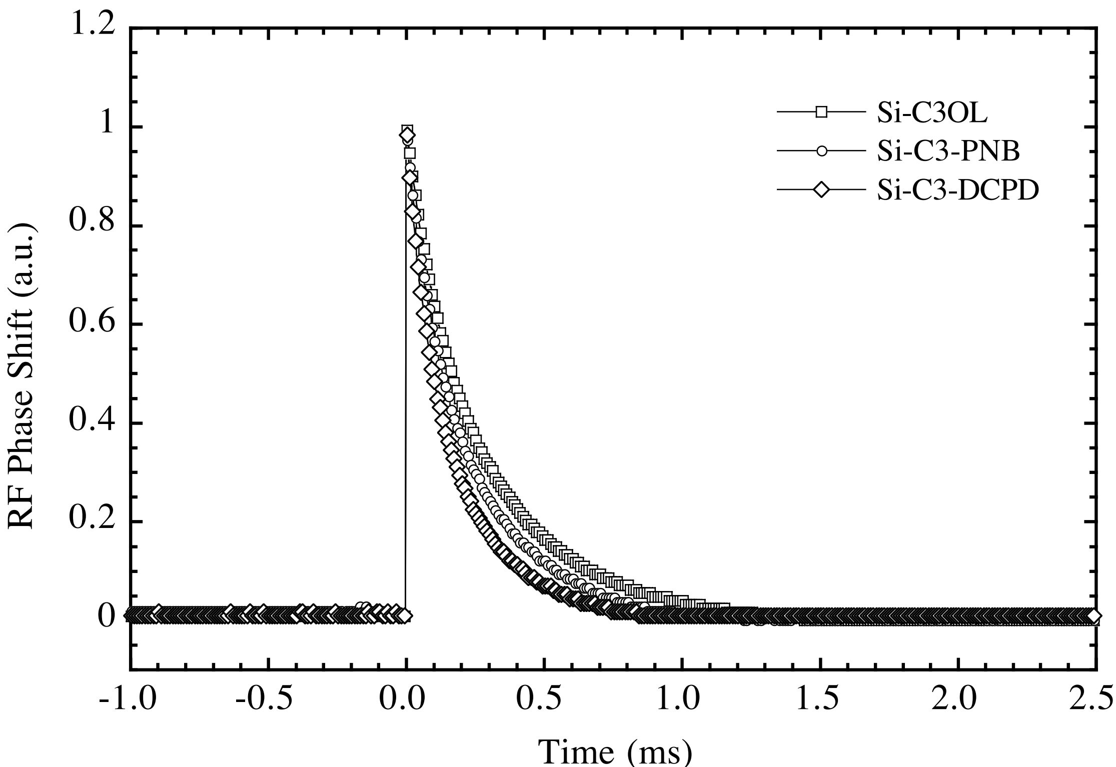

Figure 4.11

Time-resolved photoconductivity decay curves of C3 olefin-terminated (squares), C3 olefin-polynorbornene-terminated (circles), and C3 olefin-polyDCPD-terminated (diamonds) Si surfaces in an N_2(g) ambient. The decays were obtained under high-level injection conditions. Single exponential fits to these decay curves (not shown) yielded a time constant of 280 μs, 220 μs, and 168 μs, respectively.

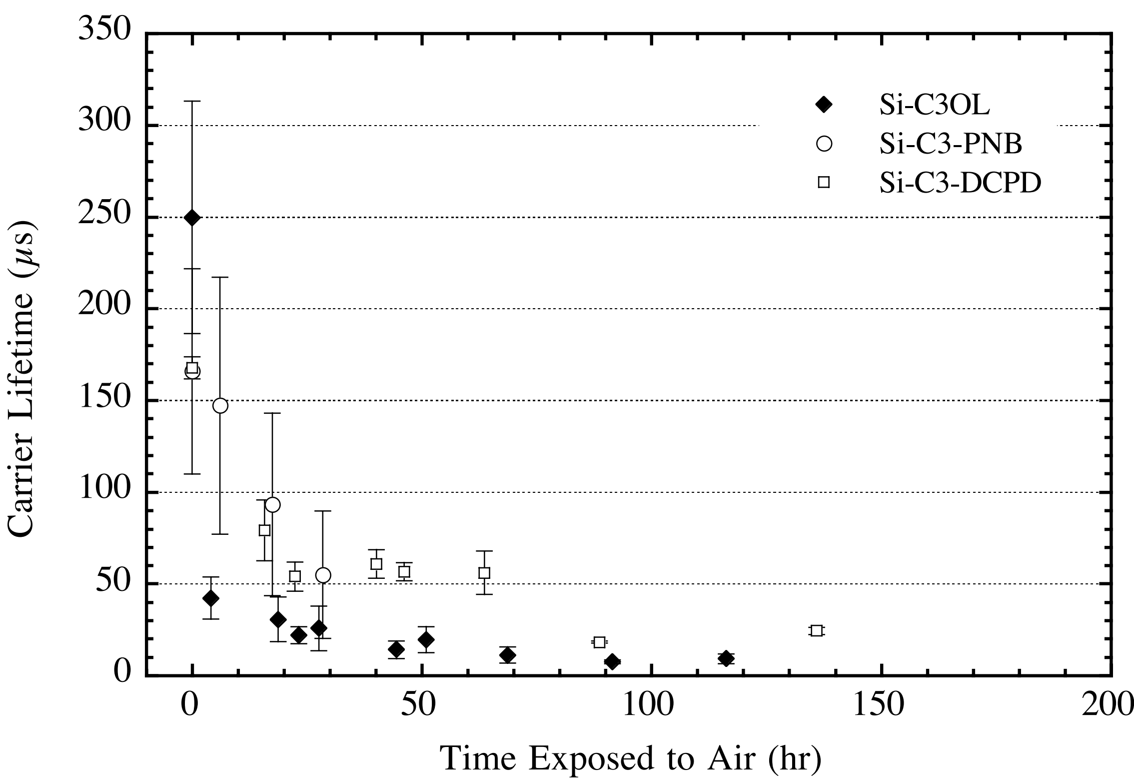

Figure 4.12

Time dependence of the mean carrier lifetimes for C3 olefin-terminated (filled diamonds), C3 olefin-polynorbornene-terminated (open circles), and C3 olefin-polyDCPD-terminated (open squares) Si in air. The samples were stored in a dark controlled environmental chamber with an air temperature of 21 °C and a relative humidity of 7% in between measurements. All data were acquired under high-level injection conditions. The error bars represent the standard deviations for measurements obtained from at least three samples.

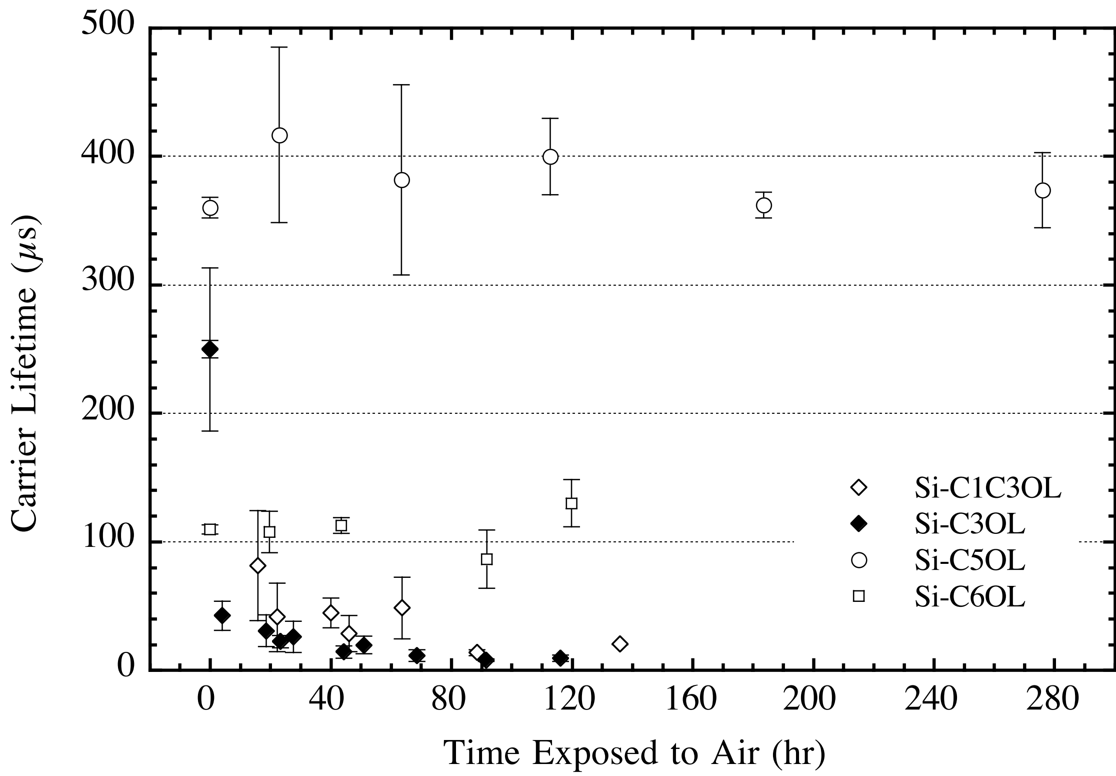

Figure 4.13

Time dependence of the mean carrier lifetimes for mixed methyl/C3 olefin-terminated (open diamonds), C3 olefin-terminated (filled diamonds), C5 olefin-terminated (open circles), and C6 olefin-terminated (open squares) Si surfaces in air. The samples were stored in a dark controlled environmental chamber with an air temperature of 21 °C and a relative humidity of 7% in between measurements. All data were acquired under high-level injection conditions. The error bars represent the standard deviations for measurements obtained from at least two samples.

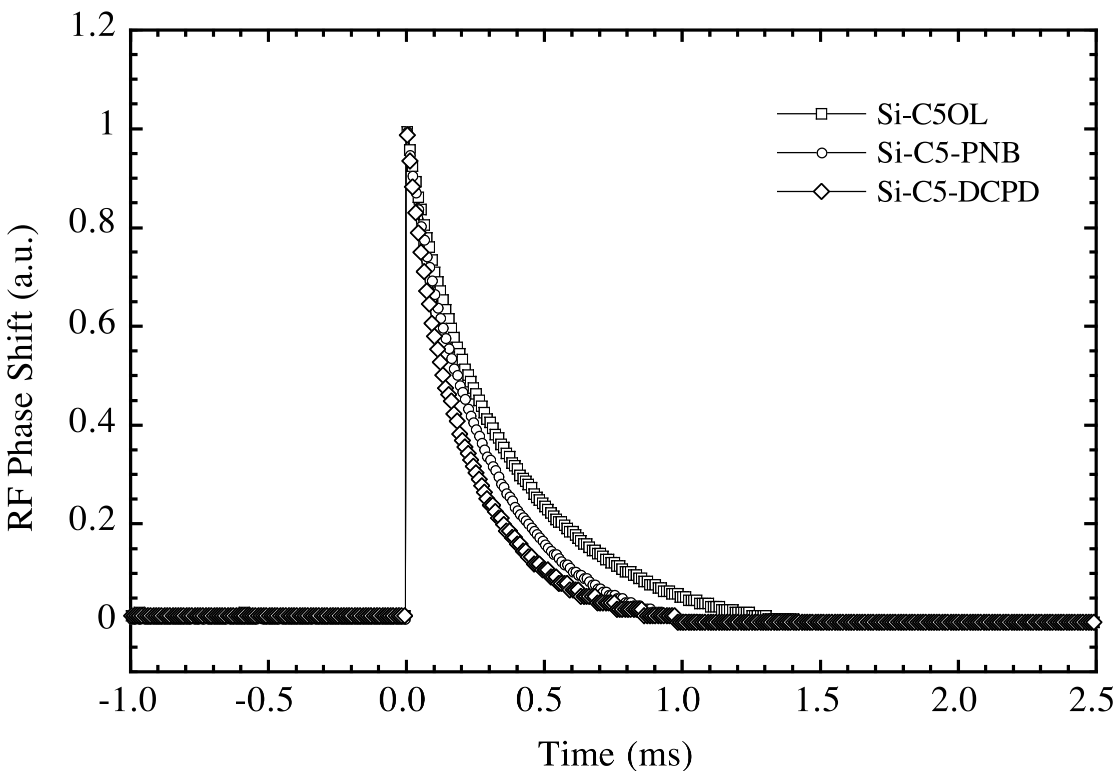

Figure 4.14

Time-resolved photoconductivity decay curves of C5 olefin-terminated (squares), C5 olefin-polynorbornene-terminated (circles), and C5 olefin-polyDCPD-terminated (diamonds) Si surfaces in an N_2(g) ambient. The decays were obtained under high-level injection conditions. Single exponential fits to these decay curves (not shown) yielded a time constant of 366 μs, 273 μs, and 219 μs, respectively.

Figure 4.15

Time dependence of the mean carrier lifetimes for (a) C5 olefin-terminated, (b) C5 olefin-polynorbornene-terminated, and (c) C5 olefin-polyDCPD-terminated Si surfaces exposed to elevated temperature/humidity (open circles) and low temperature/humidity (filled circles) conditions. The samples exposed to the elevated temperature/humidity condition were stored in a dark controlled environmental chamber with an air temperature of 40 °C and a relative humidity of 80–90% in between measurements. The samples exposed to the low temperature/humidity condition were stored in a dark controlled environmental chamber with an air temperature of 21 °C and a relative humidity of 7% in between measurements. All data were acquired under high-level injection conditions. The error bars represent the standard deviations for measurements obtained from at least two samples.

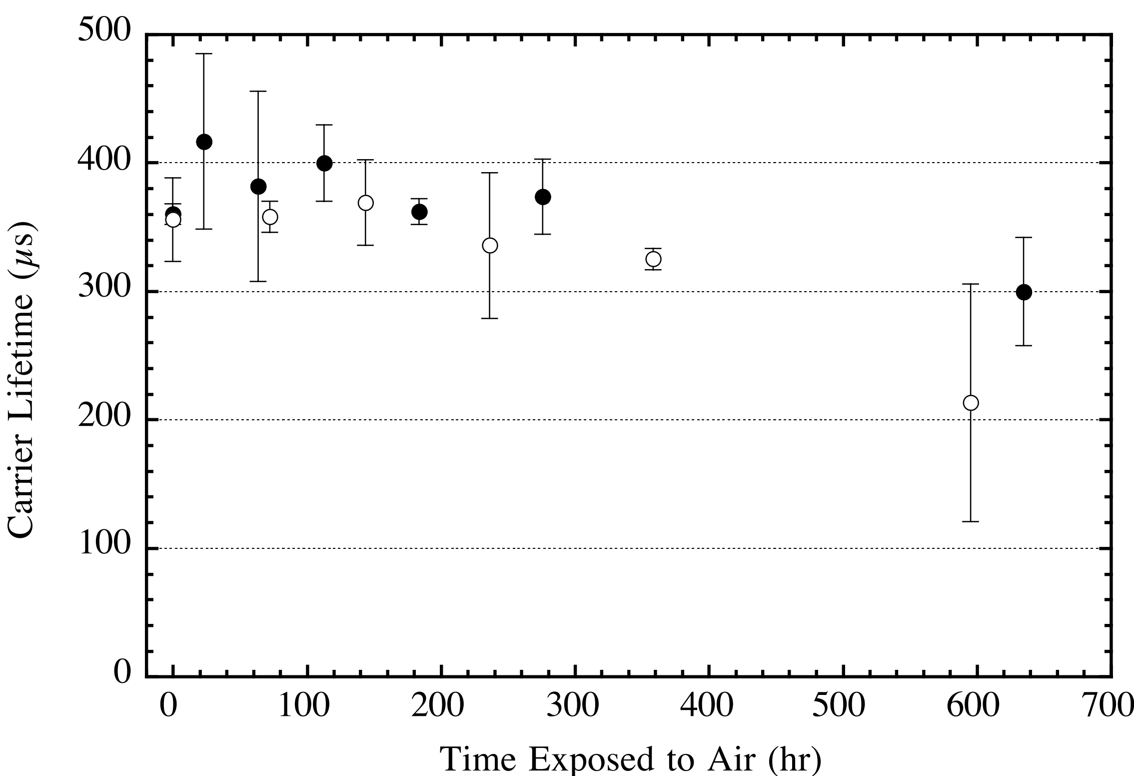

Figure 4.15a

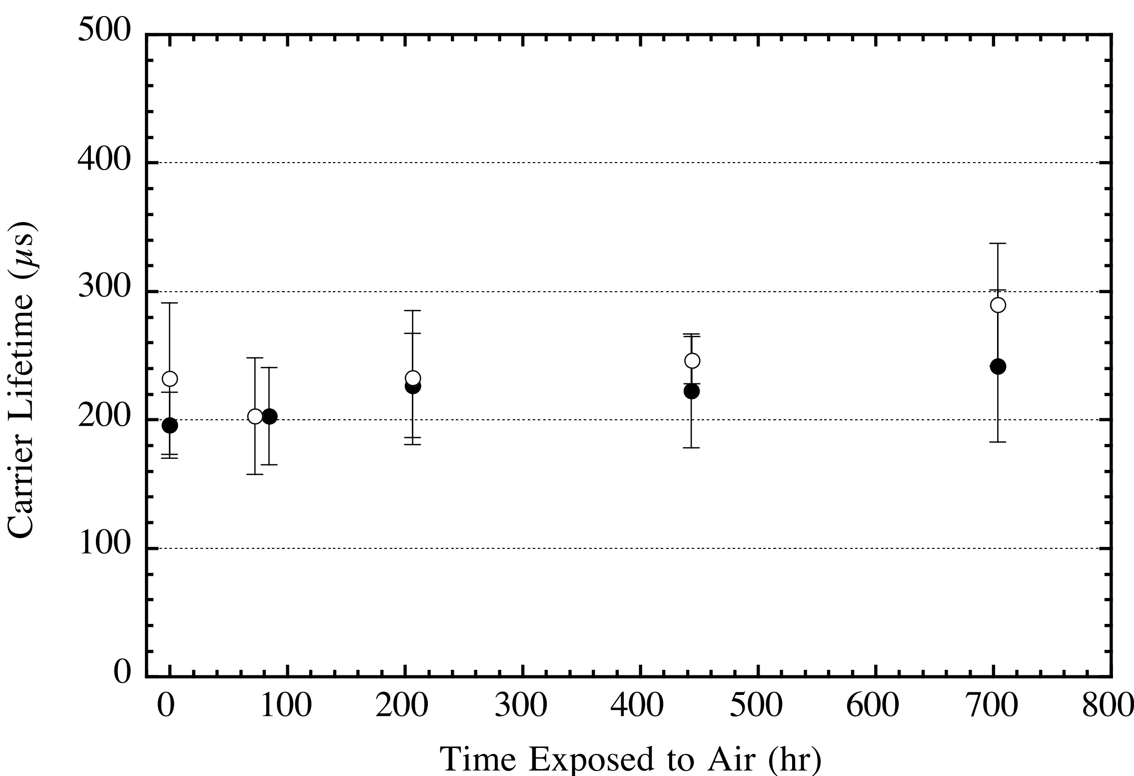

Figure 4.15b

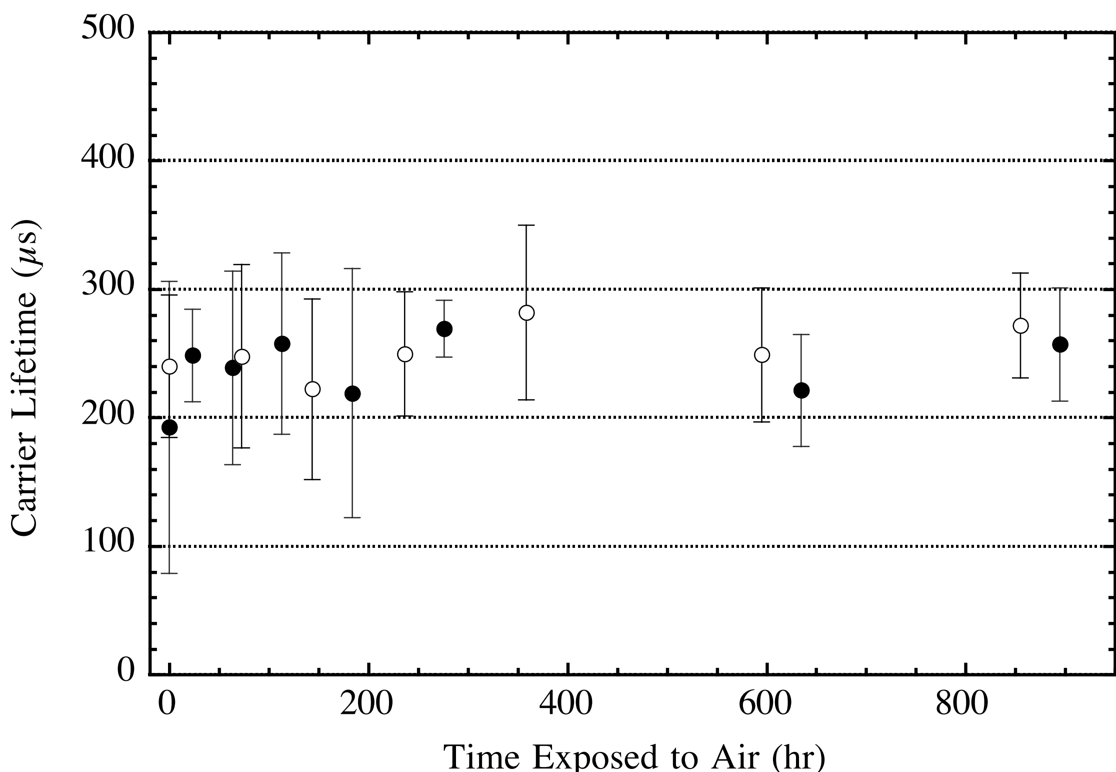

Figure 4.15c

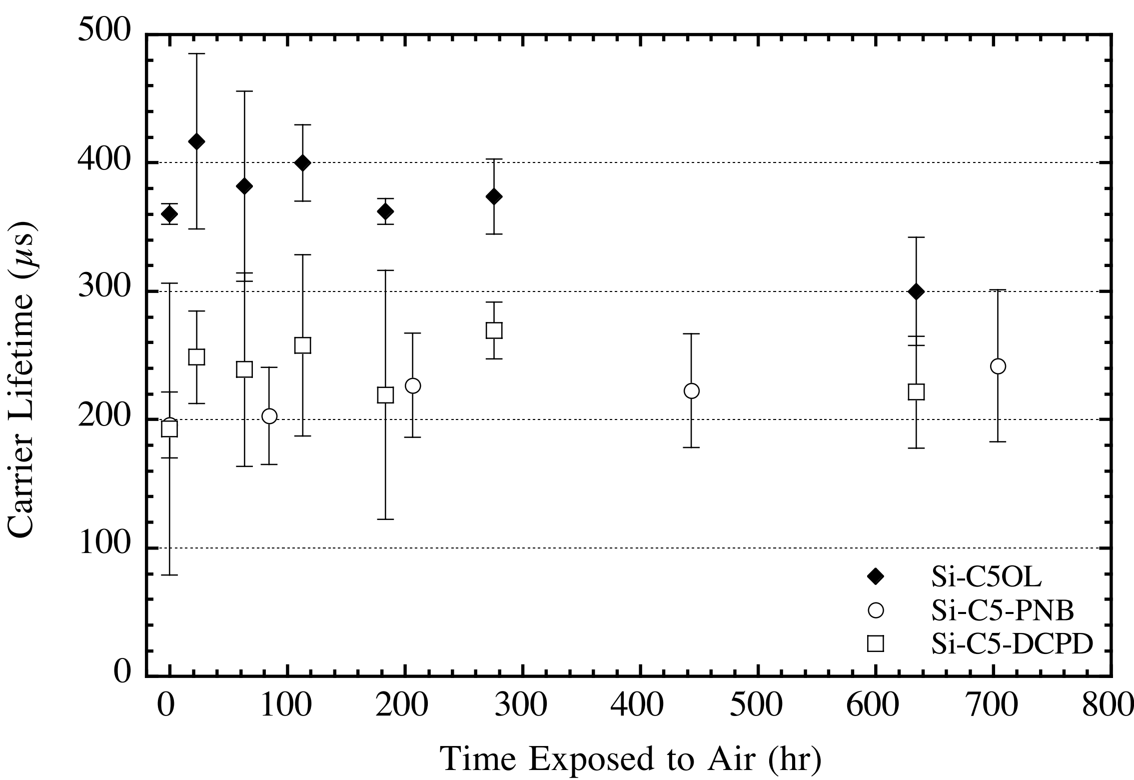

Figure 4.16

Time dependence of the mean carrier lifetimes for C5 olefin-terminated (filled diamonds), C5 olefin-polynorbornene-terminated (open circles), and C5 olefin-polyDCPD-terminated (open squares) Si surfaces exposed to a low temperature/humidity condition. The samples were stored in a dark controlled environmental chamber with an air temperature of 21 °C and a relative humidity of 7% in between measurements. All data were acquired under high-level injection conditions. The error bars represent the standard deviations for measurements obtained from at least two samples.

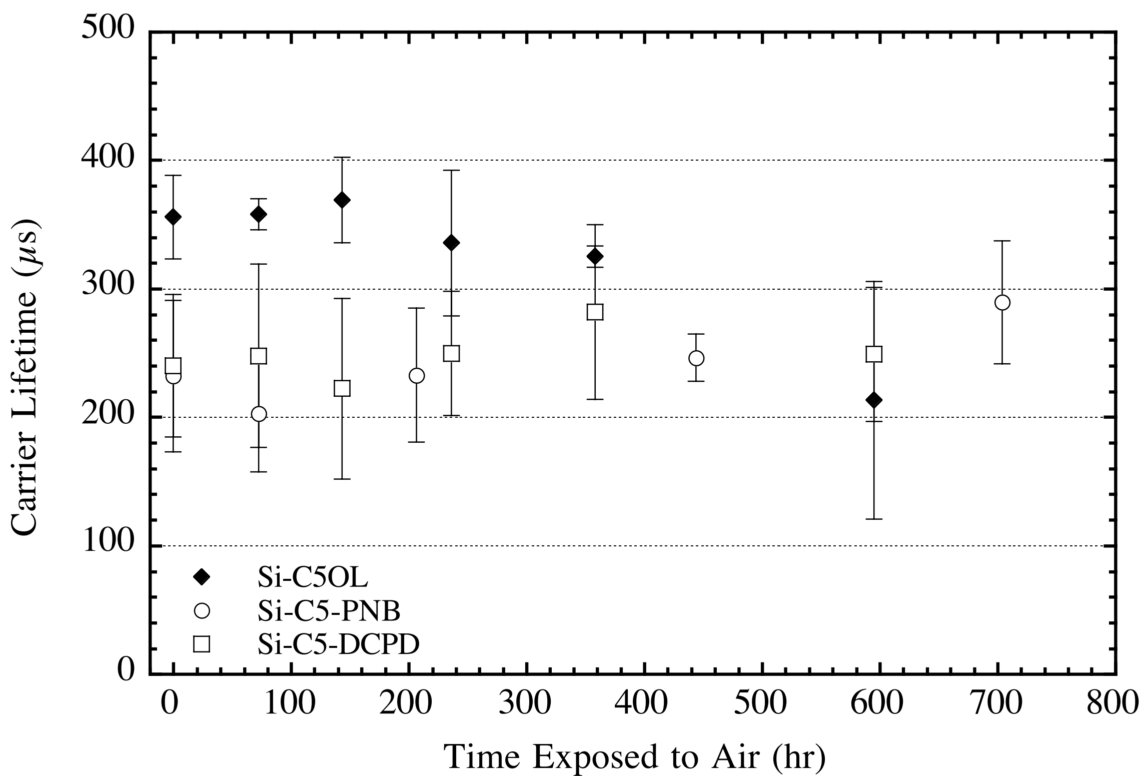

Figure 4.17

Time dependence of the mean carrier lifetimes for C5 olefin-terminated (filled diamonds), C5 olefin-polynorbornene-terminated (open circles), and C5 olefin-polyDCPD-terminated (open squares) Si surfaces exposed to an elevated temperature/humidity condition. The samples were stored in a dark controlled environmental chamber with an air temperature of 40 °C and a relative humidity of 80–90% in between measurements. All data were acquired under high-level injection conditions. The error bars represent the standard deviations for measurements obtained from at least two samples.

Table 4.3

Time-dependent measured carrier recombination lifetimes and surface recombination velocities for various modified Si surfaces. Values of S were calculated assuming an infinite bulk lifetime.

Overlayer	τ (μs)	S (cm s^{-1})	τ (μs)	S (cm s^{-1})	τ (μs)	S (cm s^{-1})
21 °C/7% R.H.	**In N_2(g)**		**After ~30 hr in Air**		**After ~120 hr in Air**	
C3 olefin	250 ± 60	59 ± 10	26 ± 10	570 ± 270	9 ± 3	1600 ± 500
C3 olefin-polynorbornene	230 ± 90	64 ± 20	55 ± 30	270 ± 170	--[a]	--[a]
C3 olefin-polyDCPD	170 ± 10	88 ± 3	57 ± 5	260 ± 20	24 ± 2	610 ± 40
21 °C/7% R.H.	**In N_2(g)**		**After ~150 hr in Air**		**After ~600 hr in Air**	
C5 olefin	360 ± 10	41 ± 1	360 ± 10	41 ± 1	300 ± 40	49 ± 7
C5 olefin-polynorbornene	200 ± 30	75 ± 10	230 ± 40	65 ± 10	240 ± 60	61 ± 10
C5 olefin-polyDCPD	190 ± 110	76 ± 50	220 ± 100	67 ± 30	220 ± 40	66 ± 10
40 °C/80–90% R.H.	**In N_2(g)**		**After ~150 hr in Air**		**After ~600 hr in Air**	
C5 olefin	360 ± 30	41 ± 4	370 ± 30	40 ± 4	210 ± 90	70 ± 30
C5 olefin-polynorbornene	230 ± 60	63 ± 20	230 ± 50	63 ± 10	290 ± 50	51 ± 8
C5 olefin-polyDCPD	240 ± 60	61 ± 10	220 ± 70	66 ± 20	250 ± 50	59 ± 10

[a] Charge-carrier lifetimes were not measured.

3.4. Time-Dependent XPS Studies: Oxidation of Modified Si surfaces in Air

While C5 olefin- and C5 olefin-polymer-terminated surfaces exhibited stable carrier lifetimes when exposed to air under both low temperature/humidity and elevated temperature/humidity conditions, the effectiveness of the overlayers in preventing the oxidation of Si substrates was investigated by monitoring the change in the Si 2p region of XP high-resolution spectra. The thickness of the SiO_2 layer was calculated from the relative areas of the bulk Si 2p and oxidized Si 2p peaks in the high-resolution XP spectrum. A simple substrate–overlayer model was adapted for this calculation.[59,60]

$$d = \lambda_{\text{ov}} \sin\theta \left\{ \ln\left[1 + \left(\frac{I^0_{\text{Si}}}{I^0_{\text{ov}}} \right) \left(\frac{I_{\text{ov}}}{I_{\text{Si}}} \right) \right] \right\} \tag{4.2}$$

where d is the oxide overlayer thickness, λ_{ov} is the attenuation factor through the oxide overlayer, θ is the angle of the incident x-ray beam from the sample surface, I^0_{Si}/I^0_{ov} is an instrumental normalization factor related to the ratio of the signals expected for pure Si vs pure SiO_2 and I_{ov}/I_{Si} is the ratio of oxidized Si 2p to bulk Si 2p peak areas. Using 2.6 nm for the value of λ_{ov},[61] 35° for θ, and 1.3 for I^0_{Si}/I^0_{ov},[60] the thickness of the oxide layer was determined. The oxide coverage was then estimated using the SiO_2 monolayer thickness of 0.35 nm.[62]

The time-dependent XP high-resolution spectra of C5 olefin- and C5 olefin-polyDCPD-terminated Si, oxidized under the two conditions described above, are displayed in Figure 4.18, Figure 4.19, Figure 4.20, and Figure 4.21. Oxidation of the Si substrates was observed for both types of surfaces. For C5 olefin modified surfaces, the amount of SiO_2 growth was determined to be 1.00 monolayer after 930 hours of oxidation in a 21 °C/7% R.H. condition and 0.21 monolayers in a 40 °C/80–90% R.H. condition for 860 hours. For C5 olefin-polyDCPD modified surfaces, the SiO_2 growth was 3.04

monolayers and 1.75 monolayers, respectively. In the case of oxidation under the 21 °C/7% R.H. condition, the amount of SiO_2 growth increased with the length of oxidation time. When samples were exposed to the elevated temperature/humidity condition, the oxide growth rate was faster but less overall oxide growth was observed for equivalent oxidation time lengths. For example, in an elevated temperature/humidity condition, the amount of oxide growth on a Si-C5 olefin-polyDCPD during the first 97 hours of oxidation was about the same as for the same type of surface to be oxidized in the low temperature/humidity condition for 384 hours. The oxide growth at an elevated temperature/humidity condition had also reached its maximum when the spectrum was collected after 97 hours of exposure time, while the oxide growth continued for samples stored under the low temperature/humidity condition. For comparison, the XP high-resolution spectra of the Si 2p region showing the time-dependent air oxidation of a hydrogen-terminated Si are displayed in Figure 4.22. The amount of oxide on the Si surface was determined to be 1.10 monolayers after 946 hours of air exposure at 21 ˚C/7% R.H. A summary of the oxide growth monitored by XPS is displayed in Table 4.4.

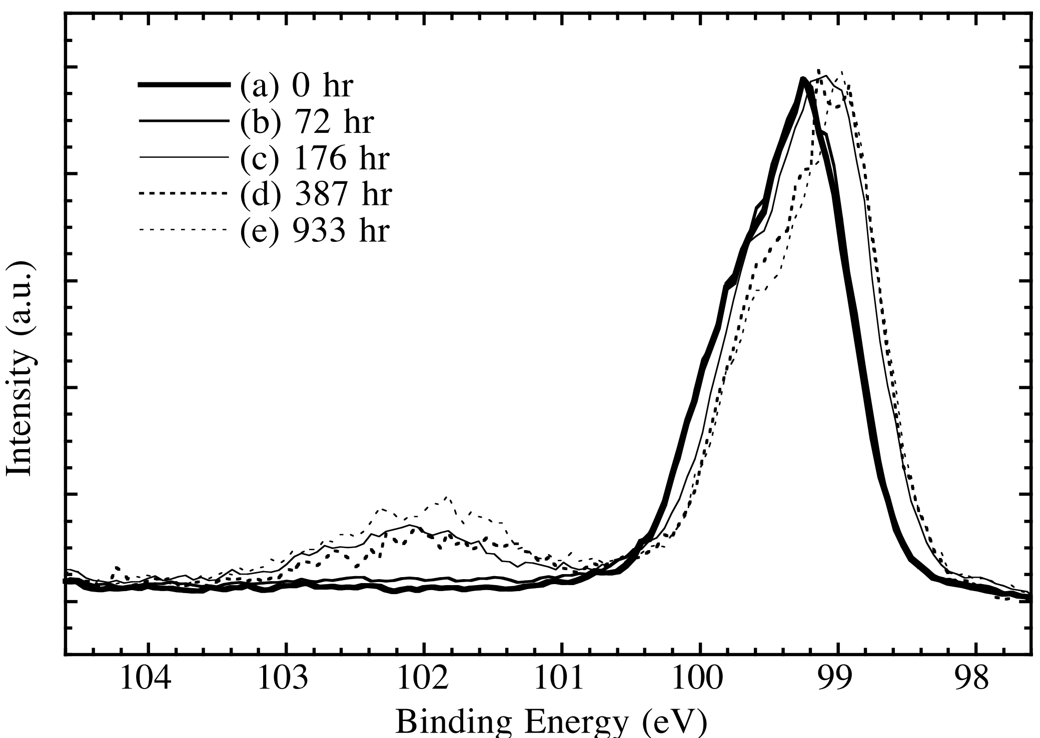

Figure 4.18

High-resolution XP spectra of C5 olefin-terminated Si focusing on the Si 2p region collected (a) before exposing the surface to the air, (b) after 72 hours, (c) after 176 hours, (d) after 387 hours, and (e) after 933 hours of air exposure, under low temperature/humidity condition. The samples were stored in a dark controlled environmental chamber with an air temperature of 21 °C and a relative humidity of 7% in between measurements. These spectra were normalized relative to the intensity of bulk Si 2p peak (98.5–100.4 eV binding energies).

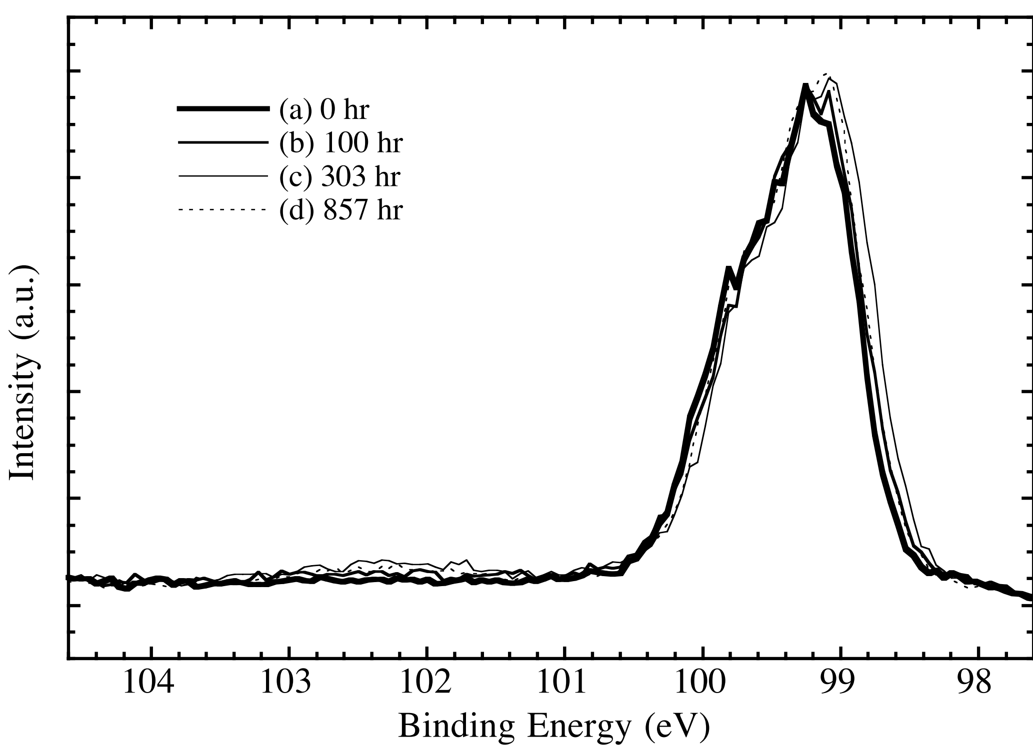

Figure 4.19

High-resolution XP spectra of C5 olefin-terminated Si focusing on the Si 2p region collected (a) before exposing the surface to the air, (b) after 100 hours, (c) after 303 hours, and (d) after 857 hours of air exposure, under elevated temperature/humidity condition. The samples were stored in a dark controlled environmental chamber with an air temperature of 40 °C and a relative humidity of 80–90% in between measurements. These spectra were normalized relative to the intensity of bulk Si 2p peak (98.5–100.4 eV binding energies).

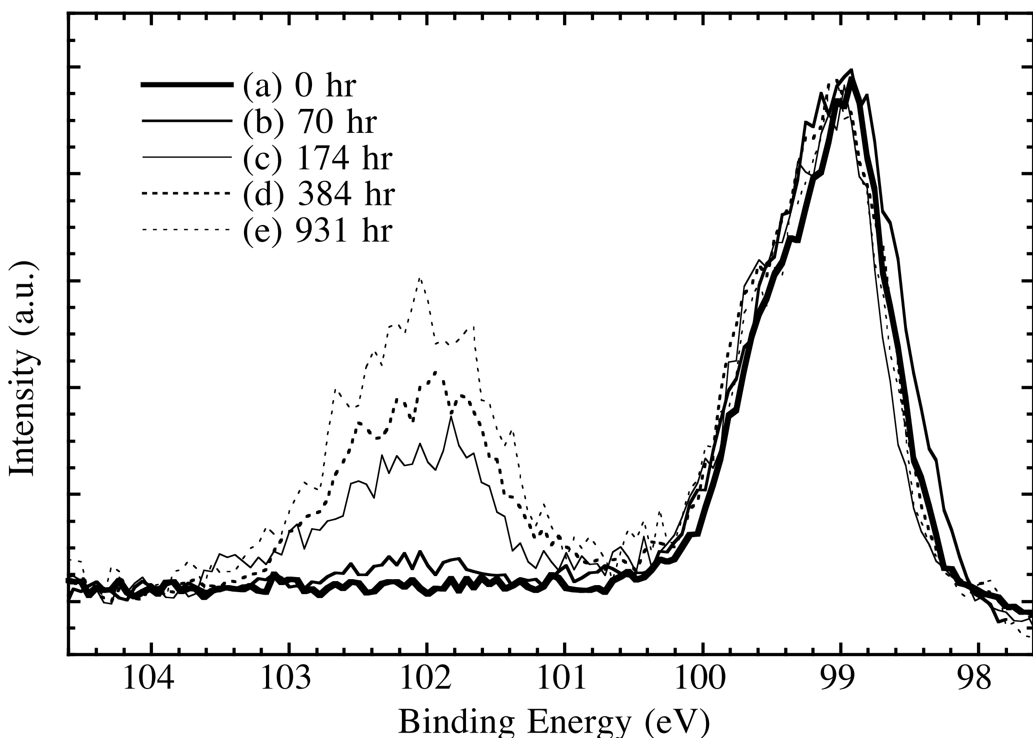

Figure 4.20

High-resolution XP spectra of C5 olefin-polyDCPD-terminated Si focusing on the Si 2p region collected (a) before exposing the surface to the air, (b) after 70 hours, (c) after 174 hours, (d) after 384 hours, and (e) after 931 hours of air exposure, under low temperature/humidity condition. The samples were stored in a dark controlled environmental chamber with an air temperature of 21 °C and a relative humidity of 7% in between measurements. These spectra were normalized relative to the intensity of bulk Si 2p peak (98.5–100 eV binding energies).

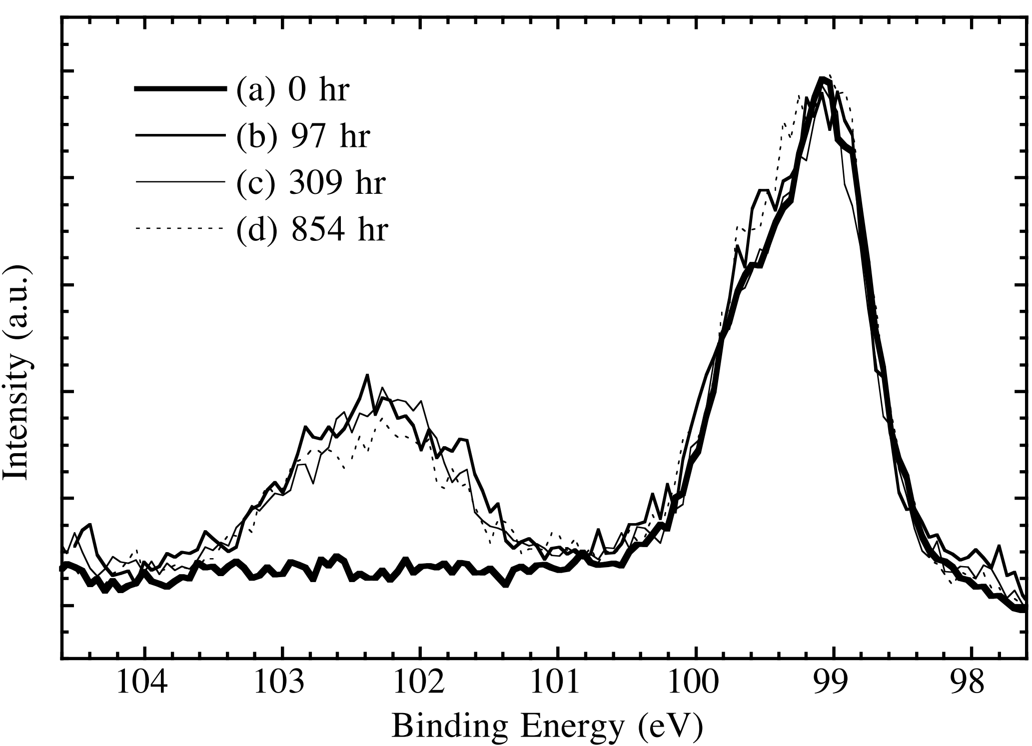

Figure 4.21

High-resolution XP spectra of C5 olefin-polyDCPD-terminated Si focusing on the Si 2p region collected (a) before exposing the surface to the air, (b) after 97 hours, (c) after 309 hours, and (d) after 854 hours of air exposure, under elevated temperature/humidity condition. The samples were stored in a dark controlled environmental chamber with an air temperature of 40 °C and a relative humidity of 80–90% in between measurements. These spectra were normalized relative to the intensity of bulk Si 2p peak (98.5–100.4 eV binding energies).

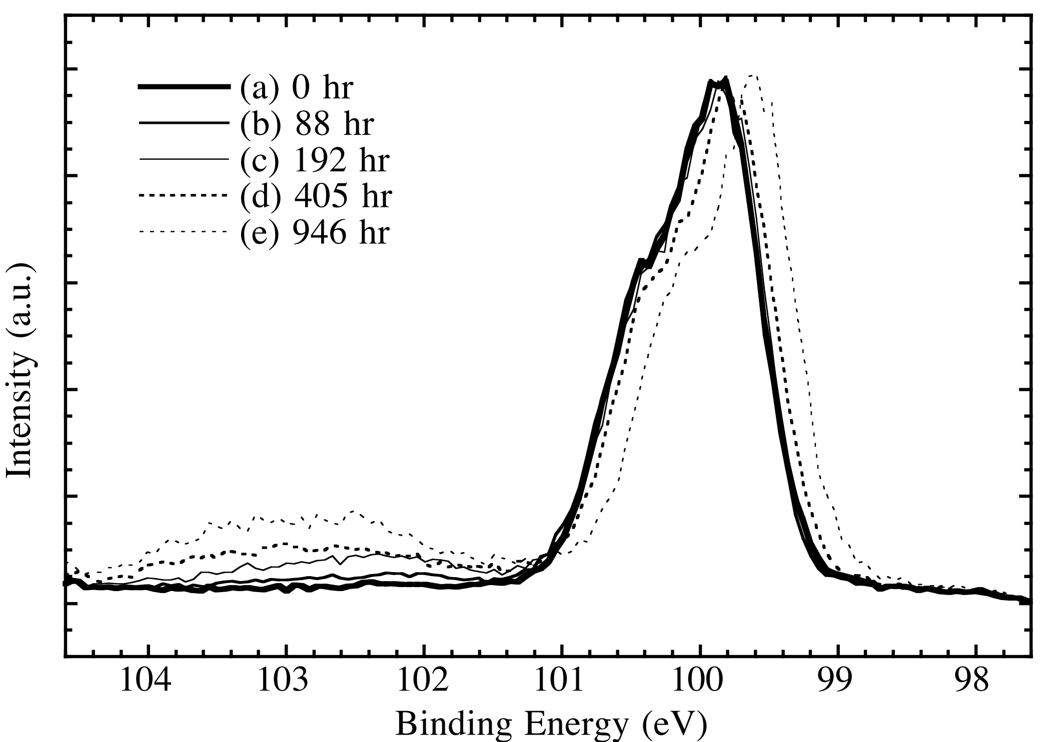

Figure 4.22

High-resolution XP spectra of H-terminated Si focusing on the Si 2p region collected (a) before exposing the surface to the air, (b) after 88 hours, (c) after 192 hours, (d) after 405 hours, and (d) after 946 hours of air exposure, under low temperature/humidity condition. The samples were stored in a dark controlled environmental chamber with an air temperature of 21 °C and a relative humidity of 7% in between measurements. These spectra were normalized relative to the intensity of bulk Si 2p peak (99.2–101 eV binding energies).

Table 4.4

Time dependence of the silicon oxide growth for C5 olefin-terminated and C5 olefin-polyDCPD-terminated Si under both low and elevated temperature/humidity conditions, and for the H-terminate Si under low temperature/humidity condition.

Time Exposed to Air (hr)	Oxidized Si 2p /Bulk Si 2p	Calculated Oxide Layer Thickness[a] (nm)	Equivalent Monolayers SiO_x[b]
Si-C5 olefin in 21 °C/7% R.H.			
72	0.004	0.008	0.02
176	0.108	0.195	0.56
487	0.116	0.209	0.60
933	0.203	0.349	1.00
Si-C5 olefin in 40 °C/80–90% R.H.			
303	0.057	0.106	0.30
857	0.039	0.074	0.21
Si-C5 olefin-polyDCPD in 21 °C/7% R.H.			
70	0.064	0.120	0.34
174	0.386	0.607	1.73
384	0.471	0.713	2.04
931	0.799	1.063	3.04
Si-C5 olefin-polyDCPD in 40 °C/80–90% R.H.			
97	0.503	0.751	2.15
309	0.406	0.633	1.81
854	0.389	0.611	1.75
Si-H in 21 °C/7% R.H.			
88	0.037	0.070	0.20
192	0.072	0.134	0.38
405	0.121	0.219	0.62
946	0.226	0.383	1.10

[a] Calculated using Equation 4.2, where the escape depth of the Si 2p electron through an oxide overlayer was taken to be 2.6 nm, $\theta = 35^{\circ}$, and the I^{0}_{Si}/I^{0}_{ov} in the Si 2p region was determined to be 1.3.

[b] The thickness of a monolayer of SiO_2 was estimated to be 0.35 nm.

4. Discussions

4.1. Surface Modifications and Characterizations

Extended from the two-step chlorination/alkylation reaction developed previously in our laboratory, a reaction sequence was advanced for the modification of Si(111) surfaces with polymers. This method would appear to be general in that a wide range of monomers can be polymerized with **1**[21,44,54,63] and could be used to form overlayers of controlled thicknesses on Si surfaces. When the first polymer layer is electrically insulating (as in the present case), this method should allow formation of metal-insulator-semiconductor structures or of capacitors of controlled thickness, whereas when the first polymer is metallic or semiconducting in nature (e.g., when cyclooctatetraenes, phenylenevinylenes, etc,. are used as feedstocks[64]), the process should provide a route to formation of semiconductor/metal or semiconductor heterojunction structures. Because the polymer was attached to the substrate through a covalent linkage, the polymer overlayer was robust and a relatively uniform growth was afforded as seen in SEM images.

Although XPS data were useful in providing evidences for each step of the surface modification process, there was a limitation that prevented us from obtaining a direct XPS confirmation for the binding of Ru catalysts to the olefin-terminated Si surfaces. The intensity of the Ru signal is expected to be very low when a relatively large amount of C can be detected on the surface. Assuming that reagent **1** has bound onto 50% of the total available groups in a monolayer of olefin on the Si surface implies a 1:41 Ru/C ratio for the atoms in the overlayer. With the atomic sensitivity factors of Ru $3d_{5/2}$ and C 1s being 1.55 and 0.205, respectively,[65] the area of the expected Ru $3d_{5/2}$ peak is calculated to be 18% of the C 1s signal. Because both the Ru $3d_{5/2}$ and Ru $3d_{3/2}$ peak

positions are within 5 eV of the C 1s peak, observation of such small Ru peaks in the presence of a large C 1s signal is not readily possible with our XPS instrument (VG Instruments M-probe Spectrometer, with a full width at half maximum of 1.50 ± 0.01 eV for the Au $4f_{7/2}$ peak in survey scan mode). Although the Ru $3p_{3/2}$ peak does not overlap with C 1peak, the Ru $3p_{3/2}$ peak is about 1/3 as intense as the Ru $3d_{5/2}$ peak. Since the estimated relative peak area of the Ru $3p_{3/2}$ is only 6% of the C 1s peak area, it can not be resolved in the XP spectra of our polymer-terminated samples. Alternatively, the control experiments were used to establish the necessity of the presence of surface-bound Ru complexes for the formation of robust polymer overlayers. The presence of a polymer overlayer with a good coverage was also confirmed by the SEM results.

Both norbornene and DCPD were readily polymerized on Si surfaces using catalyst **1** as an initiator. Although bulk metathesis polymerization of COD using catalysts **1** and **2** and COT using catalyst **2** has been reported previously,[64,66] surface-initiated ROMP of either COD or COT on Si(111) was not successful. When a Si surface was first coated with catalyst **1** by adding a few drops of 25 mM catalyst solution and the solvent was allowed to evaporate, a polymer film was observed following addition of COD to the catalyst-coated Si. The result suggested that while the surface-bound Ru catalyst was able to ROMP the highly strained norbornene; the concentration of surface-bound catalyst may not be high enough to permit detectable surface-initiated ROMP of less-strained COD and COT. The binding of a Ru complex to an olefin linker requires the complex to line up with the double bond of the linker in a certain way, and this can be quite difficult when the linker is fixed on the Si surface. The large dimensions of Ru molecules also post a geometric limitation (see Figure 4.23) which does not allow all olefin linkers on the substrate to bind with Ru; therefore, the low concentration of the surface-bound catalyst is suspected to impede the successful ROMP of less-strained ring monomers.

Another problem encountered during the Si surface modification process was the possible introduction of silicon oxide. The surface modification process involved was very sensitive to any oxygen source including methanol vapor that might be present in the N_2(g)-purged glove box. When the surface modification took place without first eliminating as much methanol vapor as possible, and when septa-capped test tubes were used instead of screw-capped, the success rate for producing oxide-free modified surfaces was very low. During the overnight heated Grignard reaction, the methanol vapor can be drawn into the reaction vessels and can provide the Si with oxygen needed for oxidation. By placing a wide-mouth bottle containing fresh P_2O_5 powders in the glove box before and during the reaction, the P_2O_5 could absorb methanol vapor and reduced the amount of volatile oxygen source. The reaction tubes were also capped tightly to ensure minimal exposure of the reaction contents to the glove box atmosphere.

Other factors that might affect the success rate of surface modification include the freshness of reagents and the possibility of the contamination of rinsing solvents. While the monomer solutions can be stored in aluminum foil-wrapped Schlenk tubes inside the glove box, it is best to use freshly made monomer solutions to assure that the correct monomer concentration was used. There is always a possibility for monomers to polymerize in the Schlenk tube if the solution was contaminated by any catalyst molecule, and this could lead to a lower than expected monomer concentration for polymerization on the substrate. The Grignard reagents purchased from Aldrich should only be used within one month after opening the bottle in the glove box. It is also best to keep the Sure/Seal caps on for all solvents and reagents, and use only syringes to dispense all liquids.

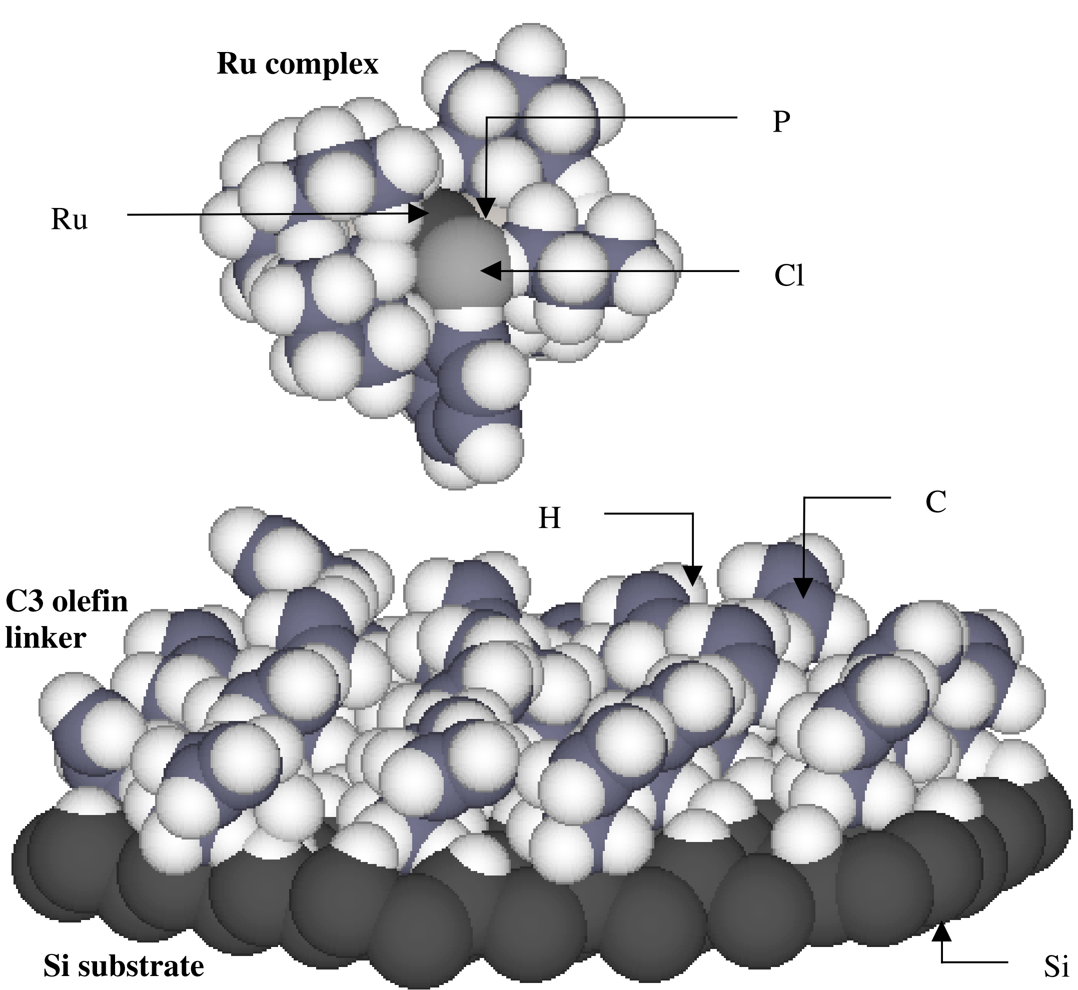

Figure 4.23

A space-filling model showing the relative sizes of the Ru catalyst and the Si surface atoms. The Si surface is covered with C3 olefin linkers. Since the cross section of a Ru complex is much larger than that of an olefin linker, the number of surface-bound Ru molecules is expected to be less than 50% of the number of linkers. The Ru addition requires a cross metathesis reaction between the Ru=C double bond and the terminal C=C double bond of the olefin linker.

4.2. Surface Recombination Velocity and Oxidation

The transient photoconductivity decay behaviors of modified Si surfaces were studied to further investigate the effects of surface modification on the electrical properties of Si. The results indicated the lack of silicon oxide formation during the surface-initiated ROMP of both norbornene and DCPD, and covalently attached polymer overlayers were grown on the Si surfaces. The initial photoconductivity decay measurements of C3 olefin-terminated, C3 olefin-polynorbornene-terminated, and C3 olefin-polyDCPD-terminated Si in an N_2(g) ambient showed that the surface modification procedure did not greatly affect the desirable electrical properties of Si, and all three types of surfaces exhibited low defect density following the reactions. However, the charge-carrier recombination lifetimes decreased quickly upon exposure to an air ambient, suggesting that the attached overlayers were ineffective in preventing the surface degradation of Si in air. When the time dependence of mean carrier lifetimes of these three surfaces were compared, the rates of decreasing lifetime were slower for both polymer-terminated surfaces, despite having shorter initial lifetimes than that of olefin-terminated Si.

When longer terminal olefin linkers, specifically C5 and C6 olefins, were used, the mean carrier lifetimes did not drop upon air exposure. In fact, C5 olefin-terminated surface was found to have an initial lifetime >350 μs, and was capable of preserving the long lifetime for at least 300 hours in air. Presumably the C5 and C6 olefin chains were more flexible while fixed onto the Si surfaces, the slight tilt of these chains could possibly cover some potential oxidation sites and decrease the chances of defect formation. Subsequent growth of polymer overlayers on top of the C5 olefin resulted in slightly shorter initial lifetimes, but both C5 olefin-polynorbornene- and C5 olefin-polyDCPD-terminated Si were capable of keeping the mean carrier lifetimes at

200–300 μs for about one month. The surface recombination velocity can be related to the surface defect density using the equation:[12,57]

$$2S = N_t \upsilon_{th} \sigma \qquad (3.3)$$

where N_t is the number of recombination centers per square centimeter, υ_{th} is the carrier thermal velocity (taken to be $\approx 10^7$ cm s^{-1}), and σ is the carrier-capture cross section. Assuming the σ is 10^{-15} cm^2, these polymer-terminated Si surfaces would have surface defect density of $(0.98–1.5) \times 10^{10}$ cm^{-2}. This is equivalent to having a low defect density of less than one active electrical defect site for every ≈ 68,000 surface atoms. This surface modification sequence using C5 olefin as a linker could therefore prove useful in providing means to functionalize Si without jeopardizing the electrical properties necessary for device applications.

While further XPS analysis of C5 olefin- and C5 olefin-polyDCPD-terminated surfaces revealed silicon oxide formation in an air ambient, the persisting slow surface recombination velocities indicated that the polymer overlayers were still effective in preventing electrical degradation of Si when oxidized. The oxide layer thickness was calculated with an assumption that ejected electrons from both bulk Si and Si oxide were attenuated by the polymer overlayer of a uniform density and thickness. However, if the oxide only grew from Si atoms that were not modified due to geometric limitation of the olefin linker, it is possible that the region of polymer overlayer above the oxide was less dense than the region above a grafting point. In this case, a larger portion of total electrons ejected from Si oxide would escape through the polymer overlayer and being collected by the analyzer compared to the number of escaped electrons originated from the bulk Si. The result would then be translated into a larger oxidized/bulk Si 2p peak ratio and a thicker calculated oxide film. The unusually large oxidized Si oxide peaks observed in the XP spectra of the polyDCPD-terminated surface may be the consequence

of this density variation, and the reported Si oxide thicknesses for this samples may not represent the true values.

Figure 4.24 displays the Si 2p high-resolution XP spectra of oxidized H-terminated, C5 olefin-terminated, and C5 olefin-polyDCPD-terminated Si surfaces after ~930 hours of air exposure under low temperature/humidity condition. A comparison of the oxidized Si 2p peak positions of these samples was made to elucidate the differences in surface oxides that gave rise to very different S. When spectra were shifted to line up bulk Si 2p peaks of these three surfaces, the Si oxide peaks of both C5 olefin-terminated and polyDCPD-terminated surfaces appeared at a slightly higher binding energy compared to that of the air-oxidized H-terminated surface. This finding suggests that a different kind of Si oxide was formed when C5 olefin-terminated and C5 olefin-polymer-modified Si were exposed to air, and this oxide formation did not create additional surface defects that could cause the S to rise. The oxide thickness was very similar between H-terminated and C5 olefin-terminated Si oxidized under the low temperature/humidity condition, but the carrier lifetime of the H-terminated Si was substantially shorter, recorded at as low as 6 μs after 900 hours of air exposure. The ability for C5 olefin-polymer-terminated Si to persist low surface defect density despite the formation of Si oxide when stored in air under both low and elevated temperature/humidity conditions proved the excellence and usefulness of this general surface modification method. This reaction sequence can provide a simple route to grow robust and uniform overlayers of polymers and block copolymers with different functionalities on Si surfaces, especially for novel applications in electrical devices requiring low surface recombination velocity.

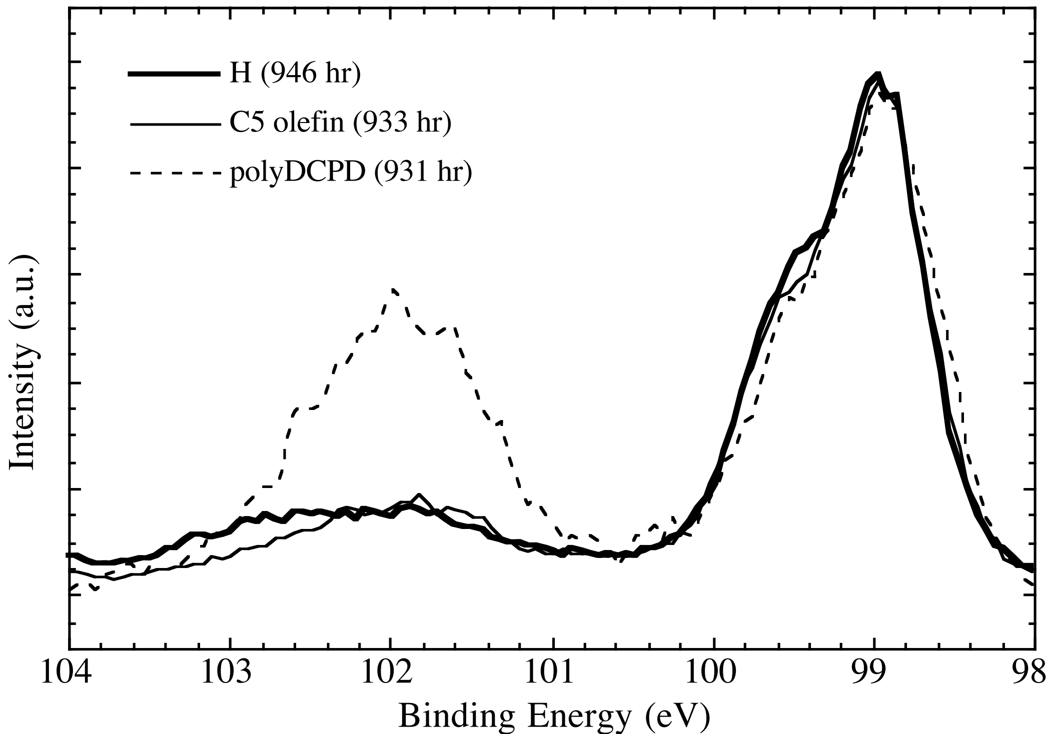

Figure 4.24

The Si 2p high-resolution XP spectra of H-terminated (▬▬), C5 olefin-terminated (——), and C5 olefin-polyDCPD-terminated (-----) surfaces. The spectra were normalized relative to the intensity of bulk Si 2p peak. The silicon oxide peak positions of both polymer-terminated surfaces shifted to slightly lower binding energy, indicating a different kind of silicon oxide was formed.

5. Summary

The growth of robust polymer films that are covalently attached to Si surfaces via a Si-C linkage was demonstrated. Uniform layers of different polymers were formed using a general method combining chlorination/Grignard reaction with ring-opening metathesis polymerization (ROMP). The surfaces of these modified Si were characterized by XPS, SEM, ellipsometry, and/or profilometry. Varying the concentration of monomer can control the thickness of the polymer overlayer, so that polymer thicknesses between 0.9 and 5500 nm can be achieved. The charge-carrier dynamics at olefin- and polymer-terminated Si/air interfaces was investigated using transient photoconductivity decay method. The C5 olefin was determined to be the optimal linker that is capable of preserving the electrical properties of the Si(111) surface when exposed to air. Time-dependent photoconductivity measurements further confirmed the ability for both polynorbornene-terminated and polyDCPD-terminated Si to maintain low surface recombination velocities in air for a period of one month, under both low and elevated temperature/humidity conditions. Instead of acting as a physical barrier against oxidation, the polymer overlayer allows the formation of non-deleterious Si oxide that does not introduce defect site on the surface. This "graft from" method is proven to be a general and simple way to modify Si surfaces with cyclic and derivatized cyclic polymers for future electronic device applications.

6. Acknowledgments

I thank Oren A. Scherman for the collaboration and for the synthesis of Grignard reagents. This work was supported by the National Science Foundation, CHE-9974562 (N.S.L.), and by the Air Force Office of Scientific Research, Grant F49620-96-0035 (R.H.G.).

7. References

(1) Bansal, A.; Lewis, N. S. *J. Phys. Chem. B* **1998**, *102*, 4058.

(2) Sailor, M. J.; Klavetter, F. L.; Grubbs, R. H.; Lewis, N. S. *Nature* **1990**, *346*, 155.

(3) Huck, W. T. S.; Yan, L.; Stroock, A.; Haag, R.; Whitesides, G. M. *Langmuir* **1999**, *15*, 6862.

(4) Clark, S. L.; Montague, M.; Hammond, P. T. *Supramol. Sci.* **1997**, *4*, 141.

(5) Whidden, T. K.; Ferry, D. K.; Kozicki, M. N.; Kim, E.; Kumar, A.; Wilbur, J.; Whitesides, G. M. *Nanotechnology* **1996**, *7*, 447.

(6) Sailor, M. J.; Ginsburg, E. J.; Gorman, C. B.; Kumar, A.; Grubbs, R. H.; Lewis, N. S. *Science* **1990**, *249*, 1146.

(7) Bansal, A.; Lewis, N. S. *J. Phys. Chem. B* **1998**, *102*, 1067.

(8) Royea, W. J.; Juang, A.; Lewis, N. S. *Appl. Phys. Lett.* **2000**, *77*, 1988.

(9) Sze, S. M. *The Physics of Semiconductor Devices*; 2nd ed.; Wiley: New York, 1981.

(10) Royea, W. J.; Michalak, D. J.; Lewis, N. S. *Appl. Phys. Lett.* **2000**, *77*, 2566.

(11) Eades, W. D.; Swanson, R. M. *J. Appl. Phys.* **1985**, *58*, 4267.

(12) Yablonovitch, E.; Gmitter, T. J. *Solid State Elec.* **1992**, *35*, 261.

(13) Aberle, A. G.; Glunz, S.; Warta, W. *J. Appl. Phys.* **1992**, *71*, 4422.

(14) Ulman, A. *An Introduction to Ultrathin Organic Films*; Academic Press: Boston, 1991.

(15) Hadziioannou, G.; Patel, S.; Granick, S.; Tirrell, M. *J. Am. Chem. Soc.* **1986**, *108*, 2869.

(16) Belder, G. F.; tenBrinke, G.; Hadziioannou, G. *Langmuir* **1997**, *13*, 4102.

(17) Dan, N.; Tirrell, M. *Macromolecules* **1993**, *26*, 6467.

(18) Lenk, T. J.; Hallmark, V. M.; Rabolt, J. F.; Haussling, L.; Ringsdorf, H. *Macromolecules* **1993**, *26*, 1230.

(19) Jordan, R.; Graf, K.; Riegler, H.; Unger, K. K. *Chem. Commun.* **1996**, 1025.

(20) Ebata, K.; Furukawa, K.; Matsumoto, N. *J. Am. Chem. Soc.* **1998**, *120*, 7367.

(21) Kim, N. Y.; Jeon, N. L.; Choi, I. S.; Takami, S.; Harada, Y.; Finnie, K. R.; Girolami, G. S.; Nuzzo, R. G.; Whitesides, G. M.; Laibinis, P. E. *Macromolecules* **2000**, *33*, 2793.

(22) Jordan, R.; Ulman, A. *J. Am. Chem. Soc.* **1998**, *120*, 243.

(23) Jordan, R.; Ulman, A.; Kang, J. F.; Rafailovich, M. H.; Sokolov, J. *J. Am. Chem. Soc.* **1999**, *121*, 1016.

(24) Prucker, O.; Ruhe, J. *Macromolecules* **1998**, *31*, 602.

(25) Zhao, B.; Brittain, W. J. *Macromolecules* **2000**, *33*, 8813.

(26) Ingall, M. D. K.; Joray, S. J.; Duffy, D. J.; Long, D. P.; Bianconi, P. A. *J. Am. Chem. Soc.* **2000**, *122*, 7845.

(27) Husseman, M.; Malmstrom, E. E.; McNamara, M.; Mate, M.; Mecerreyes, D.; Benoit, D. G.; Hedrick, J. L.; Mansky, P.; Huang, E.; Russell, T. P.; Hawker, C. J. *Macromolecules* **1999**, *32*, 1424.

(28) Boukherroub, R.; Wayner, D. D. M. *J. Am. Chem. Soc.* **1999**, *121*, 11513.

(29) Sieval, A. B.; Vleeming, V.; Zuilhof, H.; Sudholter, E. J. R. *Langmuir* **1999**, *15*, 8288.

(30) Boukherroub, R.; Morin, S.; Bensebaa, F.; Wayner, D. D. M. *Langmuir* **1999**, *15*, 3831.

(31) Sieval, A. B.; Demirel, A. L.; Nissink, J. W. M.; Linford, M. R.; van der Maas, J. H.; de Jeu, W. H.; Zuilhof, H.; Sudholter, E. J. R. *Langmuir* **1998**, *14*, 1759.

(32) Linford, M. R.; Chidsey, C. E. D. *J. Am. Chem. Soc.* **1993**, *115*, 12631.

(33) Linford, M. R.; Fenter, P.; Eisenberger, P. M.; Chidsey, C. E. D. *J. Am. Chem. Soc.* **1995**, *117*, 3145.

(34) Zazzera, L. A.; Evans, J. F.; Deruelle, M.; Tirrell, M.; Kessel, C. R.; Mckeown, P. *J. Electrochem. Soc.* **1997**, *144*, 2184.

(35) Feng, W. J.; Miller, B. *Langmuir* **1999**, *15*, 3152.

(36) Effenberger, F.; Gotz, G.; Bidlingmaier, B.; Wezstein, M. *Angew. Chem.-Int. Edit.* **1998**, *37*, 2462.

(37) Allongue, P.; de Villeneuve, C. H.; Pinson, J.; Ozanam, F.; Chazalviel, J. N.; Wallart, X. *Electrochim. Acta* **1998**, *43*, 2791.

(38) He, J.; Patitsas, S. N.; Preston, K. F.; Wolkow, R. A.; Wayner, D. D. M. *Chem. Phys. Lett.* **1998**, *286*, 508.

(39) deVilleneuve, C. H.; Pinson, J.; Bernard, M. C.; Allongue, P. *J. Phys. Chem. B* **1997**, *101*, 2415.

(40) Wagner, P.; Nock, S.; Spudich, J. A.; Volkmuth, W. D.; Chu, S.; Cicero, R. L.; Wade, C. P.; Linford, M. R.; Chidsey, C. E. D. *J. Struct. Biol.* **1997**, *119*, 189.

(41) Hamers, R. J.; Coulter, S. K.; Ellison, M. D.; Hovis, J. S.; Padowitz, D. F.; Schwartz, M. P.; Greenlief, C. M.; Russell, J. N. *Accounts Chem. Res.* **2000**, *33*, 617.

(42) Schwartz, M. P.; Ellison, M. D.; Coulter, S. K.; Hovis, J. S.; Hamers, R. J. *J. Am. Chem. Soc.* **2000**, *122*, 8529.

(43) Bansal, A.; Li, X.; Lauermann, I.; Lewis, N. S.; Yi, S. I.; Weinberg, W. H. *J. Am. Chem. Soc.* **1996**, *118*, 7225.

(44) Weck, M.; Jackiw, J. J.; Rossi, R. R.; Weiss, P. S.; Grubbs, R. H. *J. Am. Chem. Soc.* **1999**, *121*, 4088.

(45) Scholl, M.; Ding, S.; Lee, C. W.; Grubbs, R. H. *Org. Lett.* **1999**, *1*, 953.

(46) Higashi, G. S.; Chabal, Y. J.; Trucks, G. W.; Raghavachari, K. *Appl. Phys. Lett.* **1990**, *56*, 656.

(47) Hassler, K.; Koll, W. *J. Organomet. Chem.* **1995**, *487*, 223.

(48) Wyman, D. P.; Wang, J. Y. C.; Freeman, W. R. *J. Org. Chem.* **1963**, *28*, 3173.

(49) Stinespring, C. D.; Wormhoudt, J. C. *J. Appl. Phys.* **1989**, *65*, 1733.

(50) Cheng, K. L. *Japan. J. Appl. Phys.* **1995**, *34*, 5527.

(51) Tufts, B. J.; Kumar, A.; Bansal, A.; Lewis, N. S. *J. Phys. Chem.* **1992**, *96*, 4581.

(52) Mende, G.; Finster, J.; Flamm, D.; Schulze, D. *Surf. Sci.* **1983**, *128*, 169.

(53) Schwab, P.; Grubbs, R. H.; Ziller, J. W. *J. Am. Chem. Soc.* **1996**, *118*, 100.

(54) Amir-Ebrahimi, V.; Corry, D. A.; Hamilton, J. G.; Thompson, J. M.; Rooney, J. J. *Macromolecules* **2000**, *33*, 717.

(55) Kunst, M.; Sanders, A. *Semicond. Sci. Techno.* **1992**, *7*, 51.

(56) Yablonovitch, E.; Swanson, R. M.; Eades, W. E.; Weinberger, B. R. *Appl. Phys. Lett.* **1986**, *48*, 245.

(57) Yablonovitch, E.; Allara, D. L.; Chang, C. C.; Gmitter, T.; Bright, T. B. *Phys. Rev. Lett.* **1986**, *57*, 249.

(58) Bansal, A.; Li, X.; Yi, S. I.; Weinberg, W. H.; Lewis, N. S. *J. Phys. Chem. B* **2001**, *105*, 10266.

(59) Briggs, D.; Seah, M. P. *Practical Surface Analysis: Auger and X-Ray Photoelectron Spectroscopy*; 2nd ed.; Wiley: New York, 1990; Vol. 1.

(60) Pomykal, K. E.; Fajardo, A. M.; Lewis, N. S. *J. Phys. Chem.* **1995**, *99*, 8302.

(61) Hochella, M. F., Jr.; Carim, A. H. *Surf. Sci.* **1988**, *197*, L260.

(62) Haber, J. A.; Lewis, N. S. *J. Phys. Chem. B* **2002**, *106*, 3639.

(63) Maughon, B. R.; Morita, T.; Bielawski, C. W.; Grubbs, R. H. *Macromolecules* **2000**, *33*, 1929.

(64) Scherman, O. A.; Grubbs, R. H. *Synth. Metals* **2001**, *124*, 431.

(65) Wagner, C. D.; Riggs, W. M.; Davis, L. E.; Moulder, J. F. *Handbook of X-Ray Photoelectron Spectroscopy*; Perkin-Elmer Corporation: Eden Prairie, MN, 1979.

(66) Bielawski, C. W.; Scherman, O. A.; Grubbs, R. H. *Polymer* **2001**, *42*, 4939.